UNIVERSITY OF SOUTHAMPTON

FACULTY OF PHYSICAL AND APPLIED SCIENCES

School of Physics and Astronomy

Multiple Lateral Photo-Dember Terahertz Emitters

by

Duncan S. McBryde

Thesis for the degree of Doctor of Philosophy

February 2016

UNIVERSITY OF SOUTHAMPTON

ABSTRACT

FACULTY OF PHYSICAL AND APPLIED SCIENCES
School of Physics and Astronomy

Doctor of Philosophy

MULTIPLE LATERAL PHOTO-DEMBER TERAHERTZ EMITTERS

by Duncan S. McBryde

Pulsed terahertz time-domain systems (THz-TDS) offer many applications for spectroscopy and imaging. Typically terahertz generation is achieved by using a photoconductive antenna to generate an electric field (of about $10\,\mathrm{kV\,cm^{-1}}$) across a semiconductor. By creating such an electric field electro-migration occurs within the photoconductive antenna to eventually bridge the antenna electrodes. As a result photoconductive switches used for terahertz generation have a limited lifetime dependent on the voltage applied to them.

This thesis investigates the lateral photo-Dember (LPD) effect as an alternative emitter that does not require an applied electric field. The photo-Dember effect relies on the difference in electron and hole mobility within semiconductors creating a current surge on photo-excitation. The lateral photo-Dember effect works by partially covering regions of the diffusion area to selectively suppresses the terahertz emission radiated by diffusion current. By selecting lateral currents the LPD emitters work in the same configuration as photoconductive antennas while only requiring a metallic boundary near photo-excitation.

We investigate the mechanism of the photo-Dember effect and the suppression that causes the LPD effect. Both 1D and 2D models are demonstrated to for calculating diffusion currents within semiconductors and are used within finite element modelling to demonstrate dipole suppression. Optical fluence, beam position and polarisation are characterised within GaAs LPD emitters with SI-GaAs showing a competing generation mechanism from the Schottky barrier at high fluences. We find that the emitter dependence on optical polarisation is due to plasmonic enhancement that occurs on the metal boundary. We demonstrate a simple to fabricate multiplexed LPD emitter based on metals with different reflectivities within the terahertz regime that can be scaled over a large area and propose a design using plasmonic enhancement.

Contents

List of Figures

List of Tables

Declaration of Authorship

I, Duncan S. McBryde , declare that the thesis entitled *Multiple Lateral Photo-Dember Terahertz Emitters* and the work presented in the thesis are both my own, and have been generated by me as the result of my own original research. I confirm that:

- this work was done wholly or mainly while in candidature for a research degree at this University;
- where any part of this thesis has previously been submitted for a degree or any other qualification at this University or any other institution, this has been clearly stated;
- where I have consulted the published work of others, this is always clearly attributed;
- where I have quoted from the work of others, the source is always given. With the exception of such quotations, this thesis is entirely my own work;
- I have acknowledged all main sources of help;
- where the thesis is based on work done by myself jointly with others, I have made clear exactly what was done by others and what I have contributed myself;
- parts of this work have been published as: [1], [2], [3], [4], [5], [6], [7], [8] and [9]

Signed:.....

Date:23/02/2016.....

Acknowledgements

Firstly I would like to thank my supervisor Dr. Vasilis Apostolopoulos for the huge amount of help that he as provided me in guiding me though my PhD and undergraduate years. Much thanks are owed to Dr. Mark Barnes, who has been a constant friend, a great colleague and a source of segueing conversations over almost any topic. Thanks to Paul Gow for all the hard experimental work that he has taken on and shared with me. Thanks to Geoff Daniell for every useful and insightful discussion about mathematics, physics, programming and computer history trivia. Thanks to all the members of the Terahertz group, past and present, who have all supported me; Lewis Maple, Joanna Carthy, Elena Mavrona, Armen Aghajani, Dr. Aaron Chung, Dr. Zakaria Mihoubi and Dr. Sam Berry. Thanks to Dr. Keith Wilcox, Dr. Adrian Quarterman and Professor Anne Tropper who provided great advice at the start of my research placement. Thanks go to Zondy Webber and Neil Sessions who have provided valuable clean room advice.

Personal thanks go to both my family; Chamain, David and Gordon McBryde and my friends; Dan Heath, Matt Proctor, Andrew Turnbull, Jonathan Woods, Yu-Ching Cha, Chris Randall, Mael Brossard, Andrew Acreman, Amelie Heuer-Jungemann, Simon Gregory, Joe Spencer, Theo Chen Sverre, Roman Bruck, Robin Head, and Olly Morris for all their advice, love, support, friendship, hugs and cups of tea.

Chapter 1

Introduction

1.1 Terahertz in the Electromagnetic spectrum

The terahertz spectrum lies between the microwave and infrared region of the electromagnetic spectrum, broadly defined as 0.3–20 THz [10]. This region has seen a surge of interest since the mid 1980's due to the invention of time-domain terahertz spectroscopy (THz-TDS) which allows the electric field of coherent terahertz pulses to be generated and measured coherently with an ultrafast laser. THz-TDS exhibits signal to noise ratios (SNR) exceeding 50 dB. With a photon energy of 1–100 meV the terahertz region is of interest as it is within the mechanical vibration and rotation modes of organic molecules [11, 12] and transparent to polymers and ceramics [13]. As a result THz-TDS has found use as a spectrographic tool [14], being capable of detecting substances such as pharmaceuticals, explosive compounds [15]. Interstellar dust produces observable terahertz emission above 10 K, of interest to the astronomy community [16]. The Atacama Large Millimeter Array (ALMA) is being used by the astronomy community for probing up to 1 THz to study the formations of young galaxies.

1.2 History

Before the growth of terahertz technology in the 1980's, the terahertz region represented a significant gap in accessibility of the EM spectrum. Conventional electronics ceased to function when driven to frequencies >300 GHz and there was a lack of low energy photon sources , representing limits from both the classical electronics and optical techniques [17]. The limits of low energy optical generation were limited by a lack of far-infra-red lasers with a radiative photon energy below 10 meV. From the lower end of the frequency spectrum conventional oscillator circuits fail to efficiency function above 300 GHz due to insufficient transistor performance above the cut-off frequency [18]. Gyrotron, klystron

and synchrotron sources represented the upper limit of accessing the terahertz spectrum by electronic oscillators, providing access up to 300 GHz. These devices are powerful, with gyrotron powers reaching into the range of MW [19], but lack coherent detection.

A breakthrough came for coherent terahertz generation in 1975 with the invention of the Auston switch [20]. The Auston switch is a photoconductive silicon switch used for synchronous detection that provides the basis for THz-TDS. The Auston switch allowed the transient conductivity to increase between two transmission lines when activated by an ultra-fast optical pulse from a Nd:Glass laser. Two optical pulses with different wavelengths alter the conductivity with a 530 nm pulse to activate and a 1.06 µm pulse to deactivate the switch. Synchronous detection was performed with an additional transition line on the same substrate with a delayed optical pulse, showing a switching time of 15 ps. Improvements in the switch were made by changing the material substrate to GaAs which removed the requirement for two optical pulses of different frequencies by reducing the carrier lifetime [21]. Mourour et al. demonstrated that picosecond microwave pulses could be generated with both Ge and GaAs photoconductive switches [22, 23], placing photoconductive generation within the microwave X-band. Auston et al. further reduced time response to 1.6 ps and showed the transient conductivity produced Hertzian dipoles using another photoconductive switch for detection [24]. Auston et al. demonstrated electro-optic rectification as a terahertz source [25], and demonstrated its use with as a coherent spectroscopy method [26]. DeFonzo et al. further demonstrated the use of terahertz propagating in free space, generated from photoconductive antennas [27, 28]. From this THz-TDS was established and remains in experimental apparatus similar to the original pump-probe design, though with many refinements to antenna optimisation and increased bandwidth of the terahertz spectrum [29–31].

1.3 THz-TDS

The time-domain terahertz spectrometer is a configuration of a standard optical pump-probe experiment as shown in figure 1.1 using synchronous detection to measure the electric field $\vec{E}_{\mathrm{THz}}$ of the terahertz pulse. An ultrafast optical pulse, such as a titanium sapphire (Ti:S) laser, is split into two beams with an adjustable delay on one of the beams. The adjustable delay line allows the relative time between the two optical pulses to be varied. The ultrafast laser typically has a $<$1 ps pulse width, with shorter pulse widths with higher bandwidth accessing wider regions of the terahertz spectrum. The optical pulse is passed through a beam splitter to create two pulse paths. One pulse is used for terahertz generation, and the other for terahertz detection. The emitter pulse is focused (usually with microscope objectives) onto the terahertz emitter and generates a terahertz pulse. A hyper-hemisphere silicon lens metallic parabolic mirror arrangement is used to collimate the terahertz beam. Using a similar parabolic emitter and silicon lens, the terahertz pulse is focussed onto the terahertz receiver. While this occurs the probe

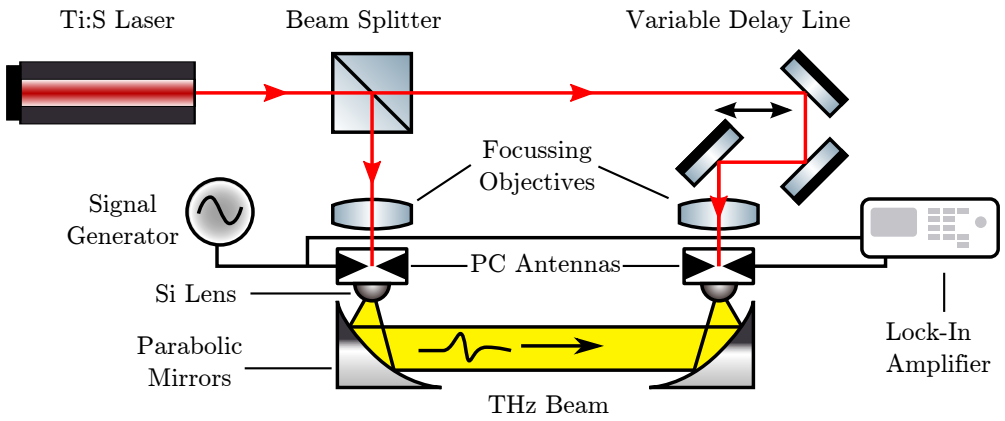

Figure 1.1: Diagram of a THz-TDS optical layout using photo-conductive antennas as both terahertz emitter and receiver. The relative time of arrival of the terahertz pulse and the optical probe pulse is controlled by the variable delay line. The delay line is varied to scan the temporal profile of the terahertz pulse with the probe pulse. Lock-in detection is used to remove background noise from the receiver by convolving the detected electric field with the reference signal.

pulse propagates though a variable optical delay, in the case of figure 1.1 shown as a retro-reflector on a stage. If the path lengths between the emitter pulse and probe pulse are the same, both the terahertz pulse and optical probe pulse arrive at the detector at the same time. If the path lengths between the probe and emitter pulse are different, the relative time of arrival $\tau = d/c$ where d and c are the change in optical delay length and speed of light. By scanning the optical delay d the probe pulse is scanned over the terahertz pulse to measure $\vec{E}_{\mathrm{THz}}$ in over the time range τ of interest. The synchronous detection using the optical pulse and the terahertz pulse is the cause for the high signal to noise ratios achieved with THz-TDS.

The experiment is modulated for lock-in detection to reduce background noise. The terahertz emitter is modulated on and off, either electrically with a signal generator or by optically chopping the beam. The emitter modulation is based from a reference signal that is fed into the lock in amplifier along with the input signal from the terahertz detector. The lock-in amplifier convolutes the reference signal with the detected signal with each step of the delay stage. This convolution further removes the background noise from the recorded signal provided that there is no external noise at the chosen reference signal.

1.4 Photo-Conductive Antennas

Photo-conductive (PC) antennas are typically used to both generate and detect terahertz radiation with a bandwidth of 0.1–5 THz. They typically consist of two electrodes deposited on top of a semiconductor with a gap of 1–100 µm [32], such as the illustration in figure 1.2. A voltage bias applied over the electrodes creates an electric field

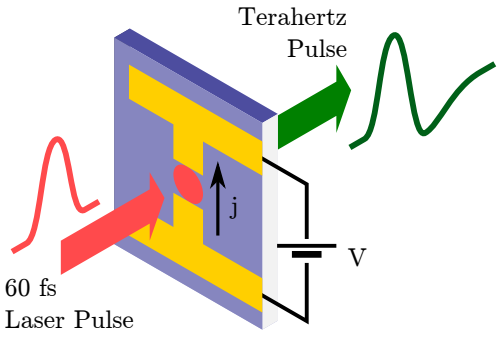

Figure 1.2: An illustration of terahertz generation within a photo-conductive antenna. Carriers are generated by the ultra-fast laser pulse, and accelerated by the electric field formed by the electrodes of the antenna to produce a fast transient current $\vec{j}$. The changing current $\vec{j}$ creates an electromagnetic wave on a picosecond time scale, creating the terahertz pulse. The electric field of the terahertz pulse is approximated as the rate of change of carrier diffusion $\frac{\partial \vec{j}}{\partial t}$.

($\sim$10 kV cm^{-1}). An ultra-fast (<1 ps) optical pulse with photon energy above the semiconductor band-gap strikes the semiconductor and creates free carriers by optical excitation. For a GaAs based semiconductor photoconductive antenna a titanium sapphire (Ti:S) laser is used as the centre wavelength of 800 nm is above the 1.42 eV band gap. The free carriers are rapidly accelerated resulting in a radiative dipole. The rapid acceleration of the carriers gives rise to a broad-band (1–5 THz) electromagnetic pulse. The changing dipole due to the charge current gives rise to terahertz radiation approximated as the second temporal derivative of the dipole moment [33], with $\vec{E}_{\mathrm{THz}} \propto \frac{\partial \vec{j}}{\partial t}$.

The pulse is detected using a device that measures the electric field generated by a terahertz pulse when activated by the optical probe pulse. A delay line controls the detection time of the terahertz pulse by adjusting the relative time of the arrival of the optical pulse. The adjustment of delay allows the detector to sample the electric field of the terahertz pulse synchronously by scanning over the delay length. Typically another photoconductive antenna is used for sampling the electric field of the terahertz pulse. The probe pulse is focussed onto the electrodes of the photoconductive antenna. Carriers are generated within the antenna gap by the optical pulse. The carriers form a net current when biased by the electric field of the terahertz pulse that is detected by the lock-in amplifier. When the electric field of the terahertz pulse is zero, no carriers are accelerated and no signal is observable. The detected current from the photoconductive antenna is proportional to the electric field of the terahertz pulse, convoluted with the response of the emitter determined by the carrier lifetime.

1.5 Applications of THz-TDS

Many materials, such as fabric, ceramics and paper are transparent in the terahertz region [34]. Organic molecules have distinct mechanical vibrational modes which produce

distinct absorption spectra, allowing determination for a variety of substances such as pharmaceutical compounds [35] and explosives [13, 15].

A THz-TDS system can be used to measure the spectrographic properties by placing a sample in the terahertz beam. First a reference scan is performed without a sample in place using the THz-TDS. The electric field of the terahertz scan is measured in time, and the Fourier transform of the scan is computed to determine the frequency components of the reference terahertz pulse. The sample is inserted into the terahertz beam and electric field of the terahertz scan is measured after the pulse passes through the sample. The pulse shape of the terahertz pulse electric field is altered by the sample, by absorption and reflection within the sample boundaries. When the Fourier transform is computed for the sample terahertz pulse, the absorption lines from the sample become visible. The division of the reference scan by the sample scan in the frequency domain returns the transfer function of the material. The transfer function of the sample is used to identify the absorption spectra of the sample, and can be used to determine the refractive index [36] and the layer structure of the material.

This has been demonstrated for scanning paper mail and determining the pigments of paintings for art conservation [37, 38]. As the terahertz emission is dependent on the acceleration of carriers within a semiconductor, THz-TDS has become a valuable tool for the study of ultra-fast carrier dynamics [39, 40]. THz-TDS has seen success in the quality control industry within pharmaceutical manufacturing process for identifying the distribution of active compounds within tablets. The complex refractive index of materials in the frequency domain can be determined [41] and materials are identified by examining the transfer function of the terahertz pulse [42].

1.6 The Photo-Dember Effect

Terahertz generation can occur without an external electrical bias as a result of the boundary conditions on the carrier transport within a semiconductor as a result of the Dember effect [43]. The mechanism of the photo-Dember effect arises from the differing diffusion mobilities of holes and electrons within a semiconductor, shown in figure 1.3. The difference of rate of diffusion is due to the difference in mobilities of electrons and holes in the semiconductor.

An ultra-fast laser pulse generates carriers at the surface of a semiconductor as shown in figure 1.3 The surface imposes a boundary condition on the diffusion current; diffusion cannot go beyond the semiconductor-air surface. The boundary condition constrains carriers to diffuse into the bulk semiconductor. Electrons, having a different diffusion rate to the holes in the semiconductor, diffuse faster than holes. The different diffusion rates create a net dipole orientated parallel to the surface normal of the material as shown in figure 1.3. The diffusion occurs within a picosecond time scale with the rate of

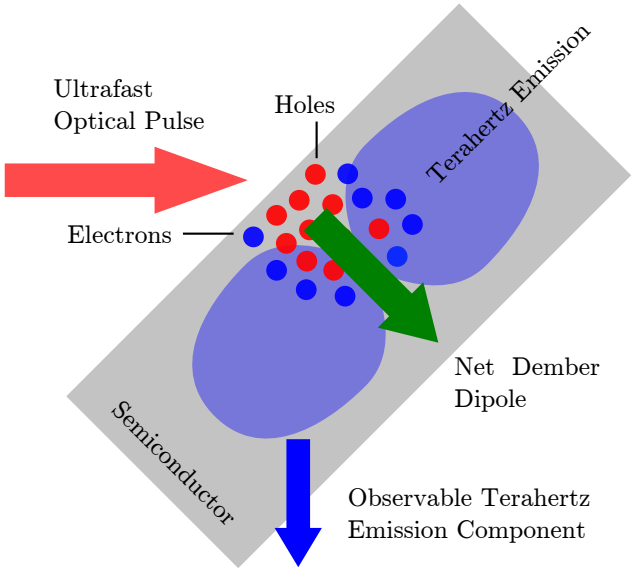

Figure 1.3: Diagram of the photo-Dember effect producing terahertz emission. The laser pulse (red) generates carriers at the semiconductor surface, which create a net dipole (green) parallel to the surface normal. The transient dipole creates terahertz emission (blue). A Hertzian dipole radiates most power 90° to the dipole direction and creates an observable component at 45° to the surface normal.

change of the diffusion current governing the terahertz emission [44]. As the radiating dipole is parallel to the surface normal terahertz emission is generated perpendicular to the surface normal, shown by the blue lobes in figure 1.3. For the short diffusion length over which the diffusion effect occurs, typically less than 10 µm which is much smaller than the wavelength of the terahertz emission, the dipole generated may be approximated as a Hertzian dipole. This dipole results in the majority of the terahertz emission propagating at 90° to the surface normal. As a result only a small component of the terahertz emission propagates out of the surface of the semiconductor, and none in the direction of the surface normal. Observable terahertz emission using the photo-Dember effect in THz-TDS is achieved by orientating the semiconductor surface at 45° to the detector so that the component of the dipole emission propagates to the detector [45]. Placing the photo-Dember terahertz emitter in the presence of a strong magnetic field of ∼1 T enhances the terahertz output [46]. The magnetic field rotates the direction of the net dipole, allowing more of the terahertz emission to be coupled into the terahertz detector [47]. The resultant terahertz pulses have higher bandwidth compared with photo-conductive antenna structures, but lower output power. The photo-Dember effect is distinct from the surface field effect caused by Fermi pinning where a net dipole is created because the Fermi level at the surface is different to the bulk Fermi level of the semiconductor [48].

An issue with the photo-Dember effect for terahertz generation is that the arrangement of the dipole direction occurs in the same direction of the surface normal. Within THz-TDS

the dipole moment created by photoconductive antennas occurs along the axis of the antenna electrodes, which is in the same plane as the surface. This arrangement allows the use of silicon lenses to efficiently couple the terahertz emission to the receiver.

1.7 Fermi Pinning

Fermi pinning is a surface field effect to occurs in semiconductors which can be used to create terahertz emission [49]. Doping a semiconductor causes the Fermi level to change within the bulk material, changing the occupancy of the conduction and valence bands. Near the surface of the semiconductor, surface states are formed as a result of the discontinuity in the crystal lattice. The surface states have a much higher density of states compared to the bulk semiconductor [50]. The increased surface states cause the Fermi level E_F to change and becomes "pinned" to the surface [51, p. 460]. This pinning causes the electrostatic potentials of the semiconductor energy bands, shown in figure 1.4, to change with depth from the surface. This band bending causes a depletion layer at the surface, which leads to a net dipole being formed when carriers are optically excited at the semiconductor surface. The net current of carriers is in the same direction as the Dember diffusion parallel to the surface normal. The direction of the dipole and current at the semiconductor surface can be changed by altering the doping concentration of the semiconductor which changes the polarity of the observed terahertz pulse [52]. The doping concentration determines the magnitude and direction of the Fermi pinning effect. Figure 1.4 (c) shows a p-doped semiconductor where the depletion field is reversed, and occurs in the opposite direction to an intrinsic semiconductor (Figure 1.4 (a)) or n-type semiconductor (Figure 1.4 (b)).

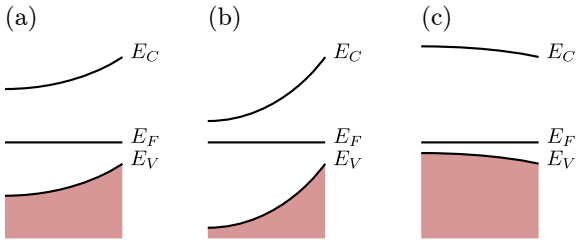

Figure 1.4: Illustration Fermi level pinning causing band bending. The figures show the electrostatic potentials for the conduction band E_C and valence band E_V for: (a) a near intrinsic semiconductor, (b) a p-type semiconductor resulting in a hole depletion layer, and (c) a n-type semiconductor with E_F pinning resulting in an electron depletion layer.

1.8 The Lateral Photo-Dember Effect

In the photo-Dember effect the radiative dipole is in the same direction as the surface normal of the semiconductor. As a result the majority of the terahertz emission from the dipole is at 90° to the dipole, perpendicular to the surface normal. In comparison to photo-conductive antennas, where the radiative dipole is perpendicular to the surface normal as in figure 1.2, this geometry is awkward to couple into an existing terahertz time-domain spectroscopy experiment which uses photoconductive antennas as an emission source. Klatt et al. claimed the ability to change the dipole vector of the photo-Dember effect to be perpendicular to the surface normal as shown in figure 1.5(b) [53, 54]. The dipole reorientation was achieved by selectively masking the surface of GaAs and InGaAs. By focussing the laser beam on to the boundary of the gold mask coherent terahertz pulses occurred without an applied bias as shown in figure 1.5(b). Changing the dipole to the plane of the surface allows the LPD emitter to be used in the same geometry as

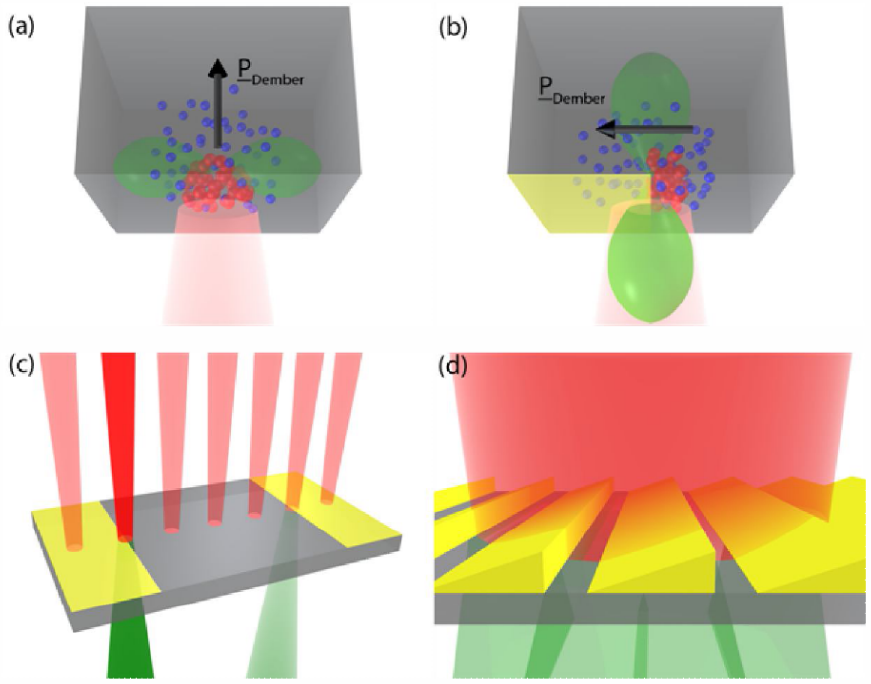

Figure 1.5: A diagram from Klatt et al. showing the proposed direction of the photo-Dember dipole $\vec{P}_{\text{Dember}}$. The green lobes representing the emitted terahertz emission. Blue points represent electrons and red points holes, and green lobes indicate the direction of terahertz emission. (a) shows the photo-Dember dipole, where the electrons diffuse to create a dipole in the same direction as the laser pulse. (b) shows the lateral photo-Dember dipole, created by the metal mask, parallel to the surface. (c) shows that repetitively masking the semiconductor with flat strips does not create a net dipole, due to the lateral photo-Dember dipoles being in equal and opposite directions. (d) shows a series of repeating ramps fabricated to increase the output power over a large area. Image used from [53].

photoconductive antennas. The mechanism behind this effect was originally attributed to the dynamics of carrier diffusion. In the normal photo-Dember effect the boundary of the surface imposed on the current creates the *net* dipole in the same direction as the surface normal as shown in figure 1.5 (a). In the lateral photo-Dember (LPD) effect a net radiative terahertz dipole is observed perpendicular to the surface normal close to a metal mask as shown in figure 1.5 (b).

Partially masking the optical pulse produces an asymmetric carrier concentration within the semiconductor, as shown in figure 1.6. Klatt et al. attributed the emission observed to the microscopic diffusion current. In figure 1.6, the microscopic current is assumed to be proportional to the carrier gradient, $\vec{j} \propto \frac{\partial n}{\partial x}$. Klatt et al. propose a greater microscopic diffusion current is created by the higher contrast regions of carrier density, $\frac{\partial n}{\partial x}$, than that from the lower contrast regions. Electrons, with higher mobility than holes, diffuse further thus creating a changing dipole. By orienting the dipole perpendicular to the surface normal, the terahertz emission occurs in the direction of the semiconductor surface normal. Aligning the terahertz emission with the surface normal eliminates the requirement to rotate the sample as in the photo-Dember effect. This allows the emission from lateral photo-Dember emitters to be used in the same geometry as a photo-conductive THz-TDS antenna. Scalability with area was also demonstrated by creating a series of gold wedges. The wedge shaped emitters in figure 1.5(d) create an asymmetric carrier distribution by using the skin depth to change the optical intensity of the beam, as shown in figure 1.7. The microscopic current, $\vec{j}$, at the thick end of the wedge is greater than that at the thin end of the wedge. The large microscopic diffusion current creates a radiating terahertz dipole that dominates over the smaller dipoles created at the thin end of the wedges.

I originally proposed a simpler fabrication method for creating a structure that would result in regions of high and low carrier density gradients in the same fashion as LPD emitters demonstrated by Klatt et al. Figure 1.7 has two regions of high and low regions of gradient in carrier density, which according to the presented hypothesis, create a net diffusion current per unit cell. Instead of creating complex three-dimensional wedges one could create a two dimensional mask to create the same carrier distribution as shown in figure 1.7. The function of the mask would be to define the initial carrier distribution formed by the optical beam. The design that I proposed had an asymmetrical distribution of fine structure along one axis. An initial carrier distribution, such as the figure shown in figure 1.8, has fine detail represented as a triangular one side and sharp high contrast region on the other. As carriers diffuse with time the fine comb structures blur together and become irresolvable. This creates two regions, where the region with fine detail creates a region of low contrast in the carrier density and the region without the fine detail has a higher contrast. The post-diffusion carrier distribution is the same to that described by Klatt et al. in figure 1.7 and thus should result in a net diffusion current if the given hypothesis for the LPD effect was valid. In the triangular emitter design

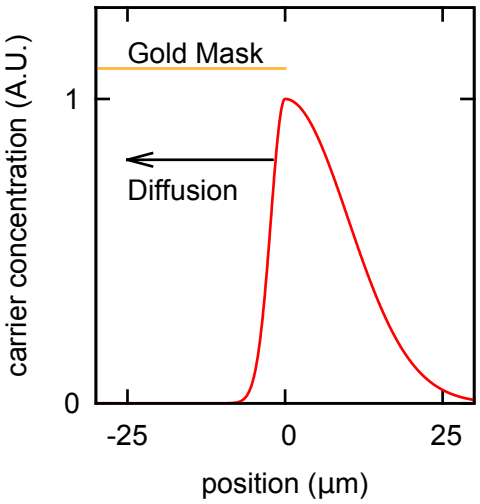

Figure 1.6: A diagram showing the initial carrier distribution near gold boundary created by a single edge LPD emitter. The gold mask changes the shape of a Gaussian optical beam to an asymmetric distribution, plotted here as a piecewise Gaussian function. According to Klatt et al. the increased gradient in the carrier distribution within $x < 0$ results in a net diffusion current $\vec{J}$, drawn as an arrow towards the metal mask.

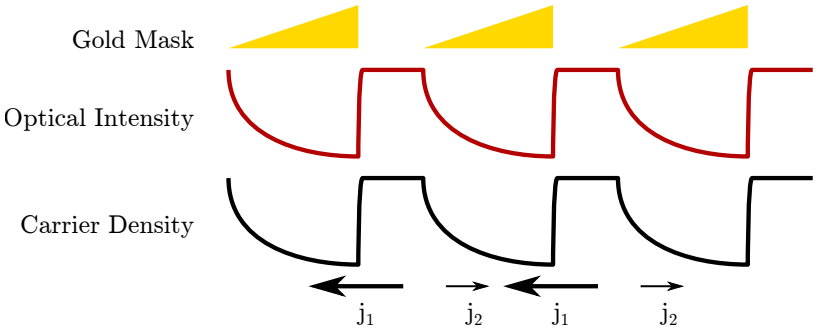

Figure 1.7: Illustrations of the multiplexed photo-Dember mechanism from Klatt et al.'s hypothesis. The gold wedge geometry allows the optical beam to partially transmitted to create an asymmetrical optical intensity, creating an asymmetrical carrier density. The carriers diffuse to create current densities j_1 and j_2. Klatt et al. proposed that $j_1 > j_2$, creating a net current. However the net current is zero and creates no net dipole to radiate terahertz emission.

the relative length scale and velocity is important. Electrons should have a similar diffusion length to the fine structure before they recombine If the electron velocity is $\sim 1 \times 10^5\,\mathrm{m\,s^{-1}}$ and the lifetime 1 ps we expect the diffusion length of the order of 100 nm.

I created a two dimensional drift-diffusion model to determine if this argument was correct, which is discussed in detail in chapter 2. The model simulates the microscopic carrier current density j for a repeating unit cell. We found from the simulation results a net carrier current creates a radiating dipole, but only when taking into account the electric field created by the dipole. The net diffusion caused by the electric field was

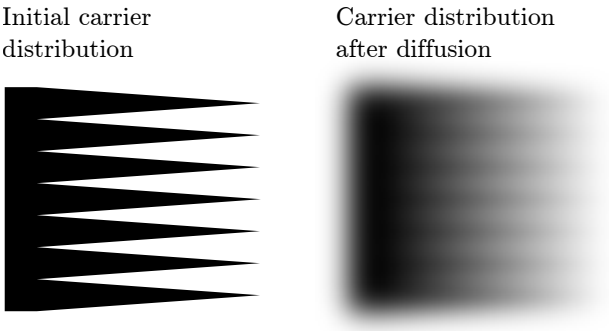

Figure 1.8: An illustration showing the original proposed mechanism for a 2D repeatable LPD emitter. A photo-lithography mask produces an asymmetric two-dimensional carrier density, shown in this case as a dark triangular pattern. The original carrier density diffuses with time and blurs the fine detail of the structure. The blurred fine detail creates a region of low carrier density gradient on the right, compared to structure on the left. This is the same profile of carrier gradient as in figure 1.6, with different spatial gradients along the x axis.

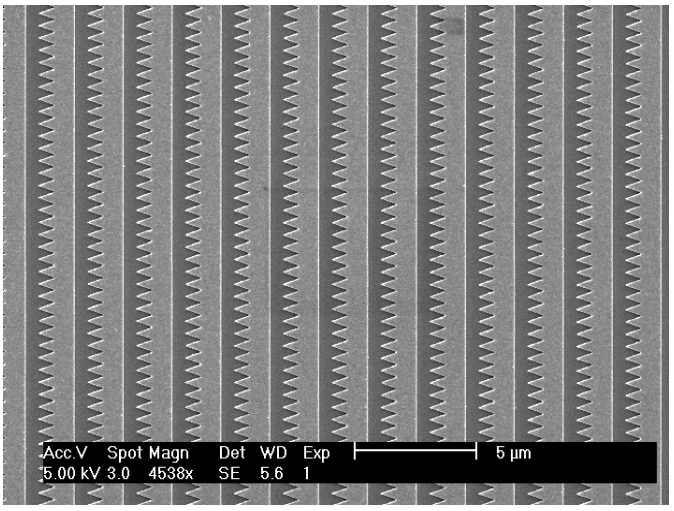

Figure 1.9: Two dimensional multiplexed emitters fabricated by Anthony Brewer by electron beam lithography. The repeatable emitters failed to produce observable terahertz emission, producing observable terahertz emission only when partially illustrated on the pattern boundary.

found to be negligible in comparison to the magnitude of net diffusion within the unit cell of the emitter. However using this result we originally believed that we found the mechanism for the LPD effect and proceeded with fabrication of the triangular LPD emitters.

We collaborated with Anthony Brewer at the Cambridge Cavendish laboratory facility to create a set of triangular emitters on low temperature grown GaAs using electron beam lithography, as shown in figure 1.9. The results from the diffusion simulation were used to pick the optimal geometry of the triangular comb structure. The fabricated triangular emitter failed to produce observable terahertz emission as predicted from the hypothesis proposed by Klatt et al. when illuminated fully in the same geometry as the original LPD

emitter. However under testing the emitters did produce observable terahertz emission when partially illuminating the boundary of the emitters. The partially masked terahertz emitters produced observable terahertz emission with less output power compared with a continuous gold boundary on LT-GaAs.

As a result of failing to detect any terahertz emission from the repeating triangular emitters Mark Barnes developed a new model for the LPD mechanism [3]. We proposed an argument demonstrating that the hypothesis for the lateral photo-Dember effect mechanism was flawed, and demonstrated this theory comparing the current direction to a photoconductive antenna [2]. The hypothesis as explained by Klatt states that the radiative dipole is created due to the contrast in the carrier distribution in figure figure 1.6, $\frac{\partial N}{\partial x}$, proportional to the microscopic current $\vec{j}$. However the *net* dipole creates the terahertz emission and is created by the *net* current $\vec{J}$. For any finite distribution of carriers N, the net current due to diffusion must always be equal to zero.

$$J = \int_{-\infty}^{\infty} j\mathrm{d}x \propto \int_{-\infty}^{\infty} \frac{\mathrm{d}N}{\mathrm{d}x}\mathrm{d}x = [N]_{-\infty}^{\infty} = 0. \tag{1.1}$$

If the net current J is zero, no net lateral net dipole can be formed, leaving the mechanism for terahertz generation due to the lateral photo-Dember effect unknown. Mark Barnes demonstrated this further by demonstrating experimentally that an asymmetric distribution of carriers caused by masked illumination does not result in detectable terahertz radiation in the LPD geometry [3].

We proposed a new hypothesis for the lateral photo-Dember emission [3]. While there is no net current there exist two equal and opposite sets of diffusion currents along the surface of the semiconductor, each creating an opposing radiative dipole as shown in figure 1.10. The dipoles radiate on the surface of a bulk semiconductor, no net terahertz emission is observed in the direction perpendicular to the surface normal. The terahertz emission from each set of dipoles is π out of phase with each other, and any emission from the dipole interferes destructively. This dual dipole emission emits terahertz emission in a quadrupole pattern, allowing some emission due to lateral diffusion to be observed off-axis.

If the carriers are generated near the gold boundary, as shown in figure 1.11, a portion of the lateral diffusion occurs under the gold mask. As a result one of the dipoles that arises from the carrier diffusion is located under the gold mask, whereas an opposing dipole of equal magnitude is located under the semiconductor surface. As is the case for the unmasked lateral dipoles in figure 1.10, the dipoles radiate terahertz emission. The dipole component under the gold mask emits a terahertz pulse that is reflected by the gold boundary. The reflected terahertz pulse is phase shifted by π due to the change in refractive index between the semiconductor and gold. If the distance from the radiating dipole to the gold edge is significantly smaller than the terahertz wavelength,

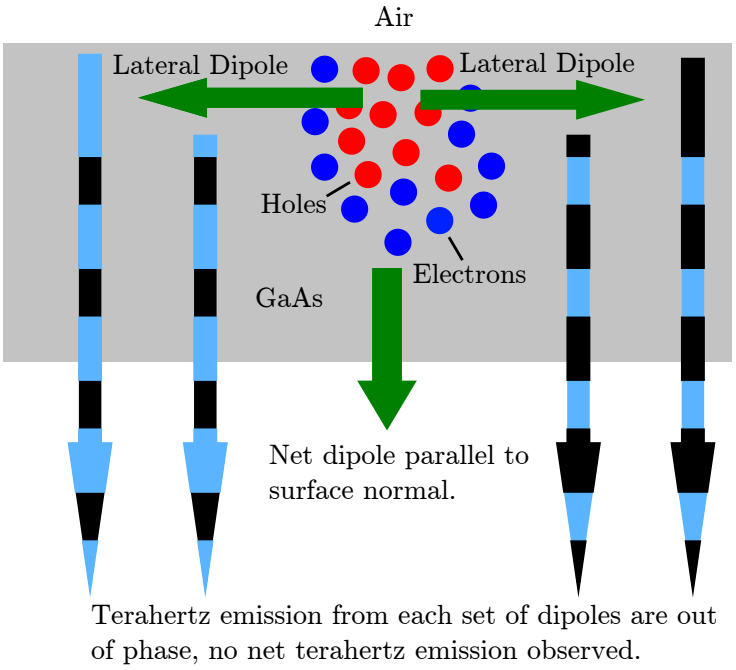

Figure 1.10: An illustration showing the considered dipoles formed in the photo-Dember effect for an unmasked semiconductor surface. Carriers are generated at the surface boundary and diffuse away from the point of excitation constrained by the surface boundary, creating a net dipole pointing into the substrate. A set of lateral dipoles are also created that occur in opposite directions to each other. The set of lateral dipoles create terahertz emission, shown in blue arrows with black markers representing the relative phase. Each set of dipoles is π out of phase with each other and no terahertz emission is measured in the direction of the surface normal.

the terahertz emission from the dipole under the edge is quenched due to interference from the reflection [55]. The reflection from the unmasked dipole is reflected without a change in phase, due to the refractive index of air being less than the semiconductor. The reflected component enhances the dipole emission. The unmasked dipole is free to radiate in the same direction of the surface normal. The net observable dipole that forms terahertz emission now has a non-zero lateral component along the plane of the surface. This lateral component allows the LPD emitter to function in the same geometry as a photoconductive antenna in a THz-TDS experiment.

With the model defined for the LPD mechanism we can understand how this related to the multiplexed emitters created by Klatt. While the varying depth of the wedges does create varying optical transmission into the substrate, the changing thickness also creates a change in the dipole quenching strength in the terahertz region due to the reduction in reflectivity. Klatt et al. published a report using the LPD emitter with erbium fiber laser that shows a SEM image of the fabricated emitter, shown in figure 1.12 [54]. To fabricate the gold wedges as illustrated in figure 1.5 (d) and figure 1.12, two metals were used; gold (Au) and aluminium (Al). Initially thin parallel walls of aluminium 250 nm wide

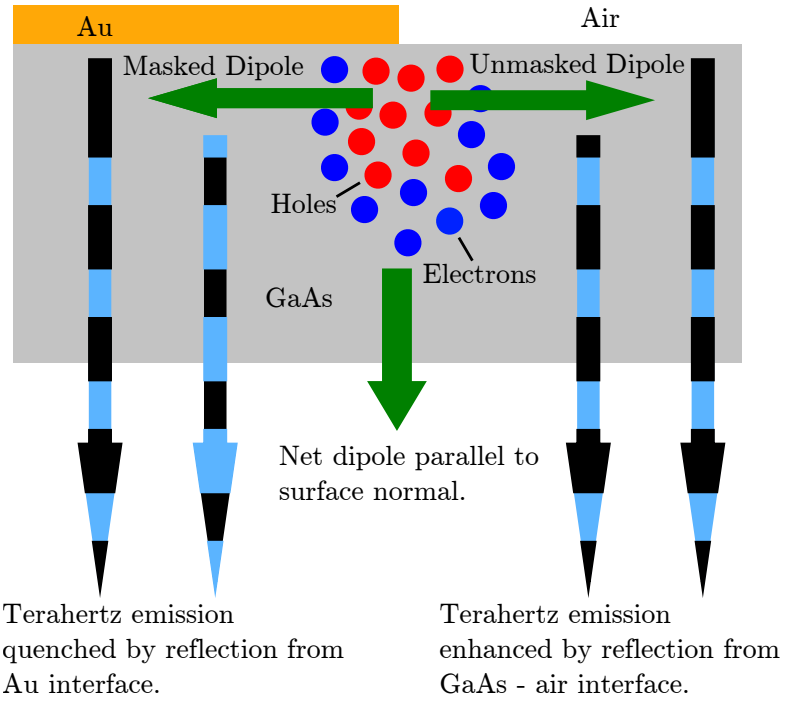

Figure 1.11: An illustration showing how terahertz emission is generated from the lateral photo-Dember effect. As in figure 1.10, dipole components are created as a result of carrier diffusion. The carriers are generated near a gold mask, so one set of dipoles is created under the metal mask. Terahertz emission is created by both masked and unmasked dipoles, and is reflected from the semiconductor surface. The terahertz emission, shown in blue arrows with black markers representing relative phase, is reflected from the metal surface. The reflection from the masked dipole acquires a π phase shift due to the increased refractive index of the metal relative to the semiconductor. The reflected terahertz emission suppresses, or quenches, the un-reflected terahertz emission due to deconstructive interference.

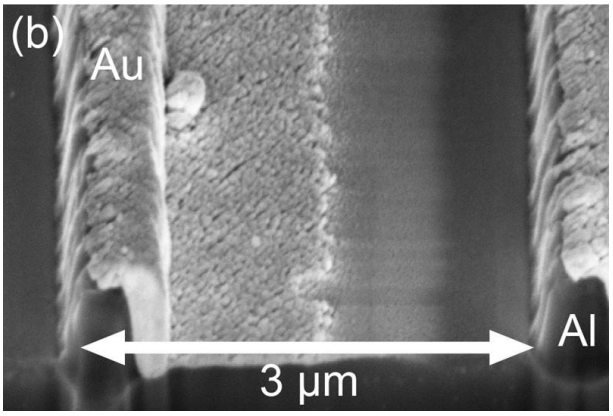

Figure 1.12: A SEM image showing the multiplexed LPD emitters as fabricated by Klatt et al. Thin walls of aluminium (Al) are deposited on the GaAs surface, and gold (Au) is evaporated at an angle to create a set of thin wedges. The wedges formed by the gold layer do not vary linearly in thickness, and show signs of percolation. Image used from [54].

with a periodicity of 3 µm are evaporated on an InGaAs substrate. The substrate is then rotated and gold is deposited at an angle. The thin walls partially block the deposited gold, partially shadowing the semiconductor surface from the evaporated gold. The gold partially accumulates against the aluminium walls' side. However this technique does not result in an ideal flat wedge shape, instead producing a step-like distribution of height between the two metals. On the region of the semiconductor where the gold is deposited, a rough non-continuous distribution of gold is formed, known as percolation [56]. We hypothesised that instead of the emitter functioning as described in figure 1.7, where regions of high current density dominate terahertz emission, the emitter functions due to the difference in quenching strength between the two metals [2, 3]. Both aluminium and gold have different reflectivities within the terahertz regime [57]. As the efficiency of dipole quenching is dependent on the reflectivity from the metal surface, a difference in reflectivity would cause a difference in dipole quenching strength each side of the repeatable LPD emitter. The difference in quenching would cause a net lateral dipole to be observable. This hypothesis is used to create two dimensional emitters, discussed in more detail in chapter 4, using two different metals with different reflectivities. Klatt et al's model predicts that the net diffusion created by a carrier contrast gradient will diffuse toward from the metal edge, as shown in figure 1.6. Using a photoconductive antenna with a known bias for reference we demonstrated that the polarity of the terahertz pulse from the LPD emitter is in the opposite direction of Klatt et al's hypothesis [2]. The current shown in figure 1.6 would instead have the emitted terahertz pulse quenched by the metal mask above. Current resulting from diffusion from the unmasked region would be free to radiate. The polarity of the terahertz pulse from a single edge demonstrates the same polarity as current diffusing away from the metal edge [2].

1.9 Applications of LPD Emitters

The main advantage that LPD emitters have as a terahertz source within THz-TDS is that they function as a passive component. A photo-conductive antenna requires an external bias to operate. Though producing very high signal to noise ratios, typically above 50 dB, small-gap photo-conductive antennas suffer from a limited lifetime due to electromigration from the metal structure. The high electric field required to rapidly accelerate the carriers in the semiconductor limits the lifetime of the emitters due to electromigration between the electrodes of the antenna in a THz-TDS environment [58]. The electromigration causes the photo-conductive switch to short-circuit, shown in figure 1.13, by bridging the electrodes causing device to short and not create an electric field over the antenna gap. As LPD emitters have no applied bias electromigration does not occur and this failure point is eliminated. The LPD effect has been noticed and used before on photoconductive emitters failed due to electromigration without an applied bias. Within our THz-TDS photoconductive antennas that have been damaged may

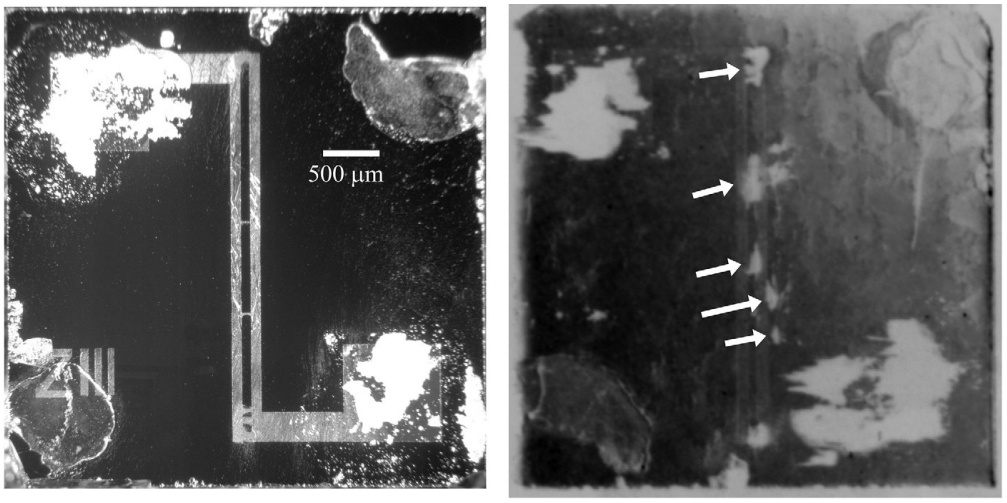

Figure 1.13: Optical (left) and X-ray (right) images of a photo-conductive terahertz emitter suffering from electro-migration. The large electric field causes the metal from the electrodes to bridge the gap of the antenna, highlighted by white arrows. Image used from Qadri et al. [58]

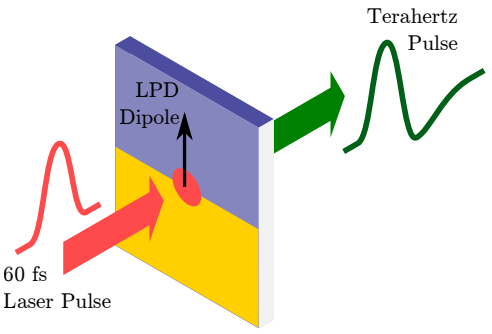

Figure 1.14: Diagram showing the orientation of the LPD dipole in the same direction as the photoconductive antenna in figure 1.2.

still be used as LPD emitters by focussing the optical spot on a metal-semiconductor boundary. If the metal-semiconductor boundary is parallel to the dipole direction, as shown in figure 1.14, the LPD dipole is in the same direction as the photoconductive current in figure 1.2. If the optical fluence is increased to ∼100 mW with a spot size of ∼50 µm with a repetition rate of 80 MHz the LPD effect creates detectable emission. This orientation allows the photoconductive structure to function as a terahertz emitter past its expected lifetime without replacement or significant re-alignment. The trade-off made for the increased reliability of the emitters is increased optical fluence from laser source.

Repeatable LPD emitters presented in this thesis are simple to fabricate and easily scalable over a large area. The emitters presented by Klatt et al. were fabricated over an area of $1 \times 1\,\mathrm{mm}^2$, whereas the multiple metal LPD emitters demonstrated in chapter 4 had dimensions of $5 \times 5\,\mathrm{mm}^2$. As the LPD emitters are fabricated by standard photo-lithography the dimension limit is the size of the photo-lithography mask and

the substrate dimensions. The advantage for using large terahertz emitter arrays over a point terahertz source is avoiding optical saturation and the possibility of selecting the polarisation properties of the terahertz pulse [59]. Creating an emitter that is capable of radial polarisation would lead to efficient wave-guiding through thin metal wires [60]. Such an LPD emitter could be made using a series of LPD emitters arranged radially, rather than in a linear pattern as described previously. The ease of scaling the LPD emitters over a large area allows for collimated terahertz output. By illuminating a set of LPD emitters with the same phase, the directionality of the terahertz output is increased if the size of the emitter array is larger then the terahertz wavelength. This collimated output reduces the complexity of alignment in the THz-TDS system, where a point source is usually collimated with a silicon lens. Such collimated output is available with multiplexed photoconductive antennas for both detection and generation of terahertz pulses, though the reduced fabrication complexity for LPD emitters makes this possibility more achievable over larger areas.

LPD emitters may be suitable for building a robust terahertz system where lifetime and reliability are crucial. If the active region of the device fails, possibly due to thermal ablation from the laser, the laser focus can simply be realigned onto a non-damaged region of the emitter without issue. Most photoconductive emitter's electrodes are connected with wire bonds which fragile when exposed and easily broken under load. The ease of fabrication onto existing substrates also opens to opportunities for integration with exiting terahertz structures such as quantum cascade lasers and wave-guides. Lateral photo-Dember emitters fabricated on a quantum cascade laser structures allow for use of the structure for pulse amplification, without coupling via and air gap.

Within a research environment a high power Ti:S laser is used which typically has an output power of $>1.5\,\mathrm{W}$. Within a photoconductive THz-TDS the optical power is reduced to 5–10 mW to prevent damage occurring to the photoconductive antennas. As a result for a research system achieving the high optical powers of 100 mW with a Ti:S laser is achievable, though with a commercial THz-TDS the laser power may have to be increased to allow operation.

Chapter 2

Lateral Photo-Dember Modelling

At the start of the investigation into the LPD effect I created a numerical simulation to find the current simulated by an array of LPD emitters [9]. The hypothesis put forward by Klatt et al. stated that the LPD effect was due to the creation of different regions of carrier contrast to create a net current [53]. To achieve this change in contrast they used metal with varying thickness, as described in chapter 1 in figure 2.1. To test Klatt et al's hypothesis [53], and to attempt to fabricate repeatable LPD emitters, we created a model of the LPD effect based on the diffusion of carriers within semiconductors.

The first model I created to simulate the lateral photo-Dember effect was a 2D drift-diffusion model, created with Python [9]. This model was created to explore the hypothesis proposed by Klatt et al. that the *net* current $\vec{J}$ produced in a unit cell was due to the initial carrier concentration gradient $\vec{\nabla} n$. The original simulation was designed to explore the suitability of the triangular comb structures proposed in chapter 1, such as those shown in figure 2.4. The simulation for testing these triangular emitters follows the description described in section 2.2 with some basic assumptions. Geoff Daniel created a drift-diffusion based one-dimensional model, with whose help I expanded into a two-dimensional model to simulate the triangular LPD emitters. The model assumed that only electrons diffused and that the hole concentration was static, and that the generation of carriers $G(t)$ was instantaneous, and that the decrease in carrier density n_e was only due to recombination with the hole density n_h. The 2D model was further developed with the aid of Geoff Daniel into a dimensionless model, treating the spatial dimensions in terms of Debye lengths. From the original simulation I showed that a net current was generated per unit cell. This net current per unit cell observed was attributed to the carrier concentration gradient hypothesis as described by Klatt et al. With the simulation results demonstrating a net diffusion current I determined that the triangular emitters would function as LPD emitters.

On device fabrication, via focussed ion beam milling and electron beam lithography made by Anthony Brewer at Cambridge, the devices failed to function under full optical

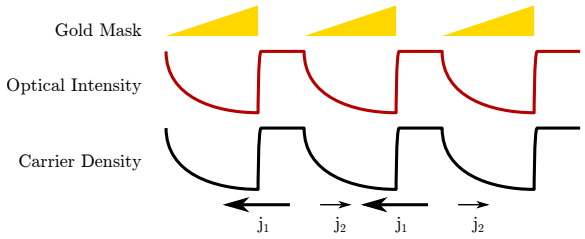

Figure 2.1: Illustrations of the multiplexed photo-Dember mechanism from Klatt et al.'s hypothesis. The gold wedge geometry allows the optical beam to partially transmitted to create an asymmetrical shadow. This asymmetrical optical field creates an asymmetrical carrier distribution within the semiconductor. Klatt et al. proposed that the large gradient in the carrier density distribution that occurs on the larger end of the wedge creates a higher diffusion current compared with the current on the sloped section of the wedge. The microscopic current is at a maximum at the thick end of the wedge, however the total current is zero and creates no net dipole to radiate terahertz emission.

illumination. The fabricated structure is shown in chapter 1 in figure 2.2. Failure of the device to produce detectable terahertz emission prompted a closer study of the simulation. While net current per unit cell is present the contribution of the net current is small relative to the absolute net current per unit cell. The net current per unit cell is due to the electric field of the displaced carriers rather than the diffusion of carriers.

The original 2D simulation was then further refined into a one-dimensional study by Mark Barnes to simulate the current distribution formed by a masked half-Gaussian, plotted in figure 2.3, to study the argument presented by Klatt et al. From the reduced one-dimensional simulation we output the current density distribution $\vec{j}$ with time and integrated this output into a time-dependent RF simulation in COMSOL, demonstrating that dipole quenching was responsible for the LPD effect [2, 3]. The one-dimensional simulation was further updated to take into account carrier generation with time by adding the term $G(t)$ to observe the effect of optical pulse width in time in the COMSOL simulations. Mark Barnes further developed the model to include a bimolecular recombination rate to accurately represent the recombination of carriers; the previous versions of the simulation assumed the recombination lifetime term τ was equal to the observed carrier lifetime [61]. When Mark Barnes investigated the 2D diffusion model with the bimolecular recombination rates, no significant change was found in the rate of change of current density. The results in this section present the simulation as the development of differential equations, incorporating the changes and revisions made including the generation term G, the dimensionless units but not the rates for bimolecular recombination.

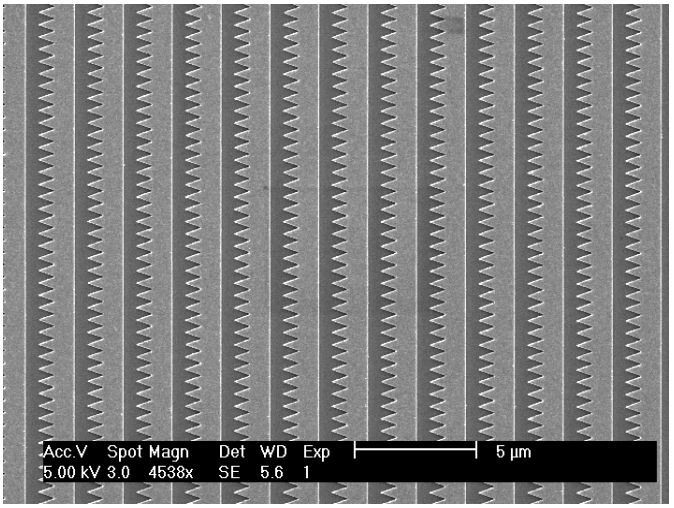

Figure 2.2: Two dimensional multiplexed emitters fabricated by Anthony Brewer by electron beam lithography. The repeatable emitters failed to produce observable terahertz emission, producing observable terahertz emission only when partially illustrated on the pattern boundary.

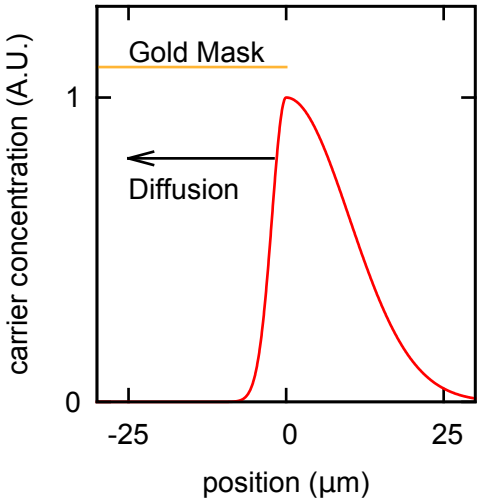

Figure 2.3: A diagram showing the initial carrier distribution near gold boundary created by a single edge LPD emitter. The gold mask changes the shape of a Gaussian optical beam to an asymmetric distribution, plotted here as a piecewise Gaussian function. According to Klatt et al. the increased gradient in the carrier distribution within $x < 0$ results in a net diffusion current $\vec{J}$, drawn as an arrow towards the metal mask.

2.1 Proposed 2D Structure

As described in the introduction Klatt et al. used a wedge shaped metal structure, as shown in figure 2.1, to change the initial carrier concentration in the semiconductor. Fabricating wedges of variable thickness near the optical skin depth causes the optical absorption of light into the semiconductor is varied along the axis of the unit cell. The optical absorption of light generates a carrier density distribution n on the surface of the semiconductor. As a result the non-symmetrical carrier gradient two regions of carrier contrast, $\frac{\partial n}{\partial x}$, are formed on each side of the repeatable emitter. The difference in $\frac{\partial n}{\partial x}$ causes a net current $\vec{J}$ to be produced according to Klatt et al's hypothesis. An alternative to creating a similar distribution of n and thus the same distribution of $\frac{\partial n}{\partial x}$, on each side of the emitter could be achieved by using 2D structures. If a 2D initial carrier concentration is defined with one region with structure smaller than the carrier diffusion length blurring occurs to create smooth regions of low carrier contrast. For example figure 2.4 (a) shows an initial electron density in the semiconductor that consists of thin repeating triangles. As time advances the electrons diffuse causing the features of the fine structure of the triangles to become blurred. After some time, the electrons diffuse to a point that resembles figure 2.4 (b). At this point the thin triangular structures are irresolvable, and create a low contrast of carrier density on the right hand edge of the structure shown in figure 2.4. The vertical edge of the emitter is still resolvable and has a higher contrast in carrier density. This is the same situation as the repeating emitters described in chapter 1 without the requirement of a varying metal mask height.

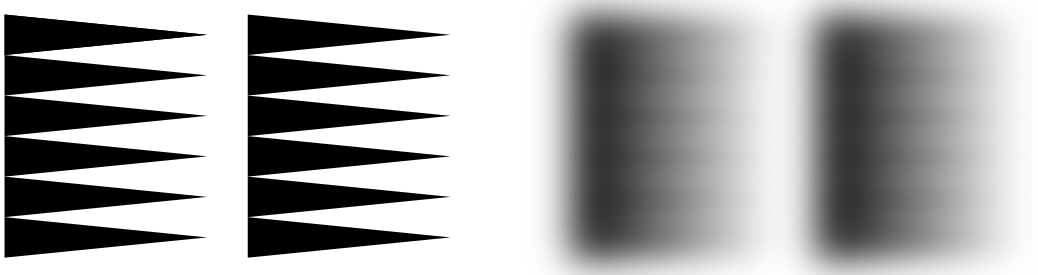

(a) Initial electron distribution (b) Electron distribution after diffusion

Figure 2.4: Figure demonstrating the proposed alternative design for lateral photo-Dember emitters. (a) shows the initial concentration of electrons in a repetitively tiled pattern consisting of thin triangles. (b) shows same concentration blurred by carrier diffusion. The blurring of the structures leads to different regions of carrier contrast on either side of the repeating emitter. According to Klatt et al's hypothesis, this would lead to a net LPD dipole due to the difference in contrast either side of the emitter.

2.2 Model description

The model used to simulate the carrier transport within a semiconductor is based on a drift-diffusion model to simulate the current within a semiconductor, similar to those used by Liu et al. [62] and Dekorsy et al. [63]. Initially we define the carrier concentration as equal amounts of electrons, n_e and holes n_h. Starting from Fick's first law [64] the flux $\vec{J}$ arising from an electron population n_e can be expressed as:

$$\vec{J} = -De\vec{\nabla}n_e \tag{2.1}$$

where D is the diffusion constant and e the elemetry charge constant. The current density $\vec{j}$ in a semiconductor is not only caused by diffusion, but also by the electric field. If we assume that the holes are static in comparison to electrons we define the current density $\vec{j}$ as

$$\vec{j} = \mu e n_e \vec{E} + eD\vec{\nabla}n_e. \tag{2.2}$$

where $\vec{E}$ is the electric field, e the electronic charge, n_e the electron density, μ the electron mobility, and D the diffusion coefficient. It is assumed that the carriers are "cold", and have the same thermal energy as the ambient temperature, k_bT. This case corresponds to using light with energy just above the band gap of the semiconductor, as with higher energy photons the carriers will gain additional kinetic energy. Within the model the carriers have a probability of recombining with each other proportional to n_e and n_h. If the average time to recombine is defined as τ_r, then the rate of change for the hole ($\frac{\partial n_h}{\partial t}$) and electron densities ($\frac{\partial n_e}{\partial t}$) defined by the conservation of charge are

$$\frac{\partial n_h}{\partial t} = -\frac{n_e n_h}{\tau_r} + G(x,t) \tag{2.3}$$

and

$$\frac{\partial n_e}{\partial t} = \frac{1}{e}\vec{\nabla}\cdot\vec{j} - \frac{n_e n_h}{\tau_r} - \frac{n_e}{\tau_t} + G(x,t), \tag{2.4}$$

where τ_r is the carrier recombination time, τ_t is the carrier trap time, and $G(x,t)$ is the carrier generation term, which in our simulation is separable into

$$G(x,t) = G(x)G(t) = G(x)\exp\frac{(t-t_0)^2}{2\sigma_t^2}. \tag{2.5}$$

Where $G(t)$ represents the temporal Gaussian pulse profile in time, centred at t_0 with pule width of σ_t. By substituting $\vec{j}$ from equation (2.2) in equation (2.4) we obtain:

$$\frac{\partial n_e}{\partial t} = \mu\vec{\nabla}\cdot(\vec{E}n_e) + D\nabla^2 n_e - \frac{n_e n_h}{\tau_r} - \frac{n_h}{\tau_t} + G(x,t), \tag{2.6}$$

which describes the evolution of n_e. The electric field is defined by Gauss's law as:

$$\vec{\nabla} \cdot \vec{E} = \frac{e}{\epsilon_0}(n_h - n_e). \tag{2.7}$$

By repeatedly solving equations (2.3), (2.6) and (2.7) for n_e, n_h and $\vec{E}$ the evolution of n_e can be obtained, which we perform with a simple Euler method for a finite time step of dt.

It is possible to choose a set of scaling factors before attempting to solve the diffusion equations. By choosing to solve equation 2.6 in dimensionless units the answer obtained can be scaled by the set scaling factors without having to run the simulation repeatedly to observe the impact of variables contained within the scaling factors. If the length x and time t are scaled so that $x = LX$ and $t = T_{scale}\tau$, equation 2.6 becomes

$$\frac{1}{T_{scale}}\frac{\partial n_e}{\partial \tau} = \frac{\mu}{L}\vec{\nabla} \cdot (\vec{E}n_e) + \frac{D}{L^2}\nabla^2 n_e - \frac{n_e n_h}{\tau_r}. \tag{2.8}$$

Equation (2.7) then becomes

$$\vec{\nabla} \cdot \vec{E} = \frac{eL}{\epsilon_0}(n_h - n_e). \tag{2.9}$$

If the variable n_0 is introduced to represent the initial density of carriers at the start of the simulation, n_e and n_h can be represented as $n_e = n_0 N_e$ and $n_h = n_0 N_h$. The normalisation is chosen so that $0 < N_h < 1$ and $0 < N_e < 1$. This therefore gives

$$\frac{\partial N_e}{\partial \tau} = T_{scale}\frac{\mu}{L}\vec{\nabla} \cdot (\vec{E}N_e) + T_{scale}\frac{D}{L^2}\nabla^2 N_e - \frac{N_e N_h}{\tau_r}. \tag{2.10}$$

If a scaling factor for $\vec{E}$ is chosen so that $\vec{E} = \frac{en_0 L}{\epsilon_0}\vec{\xi}$, where $\vec{\xi}$ is the scaled electric field, Gauss's law becomes

$$\vec{\nabla} \cdot \vec{\xi} = N_h - N_e. \tag{2.11}$$

The scaled electric field ξ is substituted into equation 2.10, leading to:

$$\frac{\partial N_e}{\partial \tau} = \frac{T_{scale}\mu}{L}\frac{en_0 L}{\epsilon_0}\vec{\nabla} \cdot (\vec{\xi}N_e) + \frac{T_{scale}D}{L^2}\nabla^2 N_e - \frac{N_e N_h}{\tau_r}. \tag{2.12}$$

The values for L and T_{scale} can be chosen to simplify equation 2.12. By choosing to base the scaling value on the Debye length L to scale the simulation with diffusivity D,

mobility μ and n_0, eliminating the need to re-run the simulation to observe the impact of these parameters. Choosing $T_{scale} = L^2/D$ and $L^2 = \epsilon_0 D/e\mu n_0$, equation 2.12 becomes

$$\frac{\partial N_e}{\partial \tau} = \vec{\nabla} \cdot (\vec{\xi} N_e) + \nabla^2 N_e - \frac{n_0 T_{scale}}{\tau_r} N_e N_h. \tag{2.13}$$

Using the Einstein relation $\mu k_B T = eD$, valid for carriers in thermal equilibrium, the scaling values for L and T_{scale} become

$$L^2 = \frac{\epsilon_0 k_B T}{e^2 n_0} \tag{2.14}$$

and

$$T_{scale} = \frac{\epsilon_0}{e\mu n_0}, \tag{2.15}$$

where L is the Debye length of the plasma created by the carriers. The recombination time t_r is scaled to give the dimensionless recombination time, $T_r = \tau_r / T_{scale}$, leaving the dimensionless equations to be solved as

$$\frac{\partial N_e}{\partial \tau} = \vec{\nabla} \cdot (\vec{\xi} N_e) + \nabla^2 N_e - \frac{N_e N_h}{T_r}, \tag{2.16}$$

$$\frac{\partial N_h}{\partial \tau} = -\frac{N_e N_h}{T_r} \tag{2.17}$$

and

$$\vec{\nabla} \cdot \vec{\xi} = N_h - N_e. \tag{2.18}$$

2.3 Two Dimensional Model

From the one dimensional model we expanded to create a two dimensional model to test the proposed triangular emitters. As we wanted to test a repeating array of emitters we assume cyclic boundary conditions so that only the unit cell is investigated. For each operation on a matrix element that relied on using the neighbouring elements, the element would cycle to the other side of the unit cell if extended beyond the length of

Temperature	T	$300\,\mathrm{K}$
Initial charge density	n_0	$1 \times 10^{20}\,\mathrm{m}^{-2}$
Carrier recombination time	τ_r	$1 \times 10^{-12}\,\mathrm{s}$
Electron mobility	μ	$0.85\,\mathrm{m}^2\mathrm{V}^{-1}\mathrm{s}^{-1}$
Generation pulse FWHM	σ_{FWHM}	$1 \times 10^{-11}\,\mathrm{s}$
Generation pulse t_0	σ_{t0}	$2 \times 10^{-11}\,\mathrm{s}$

Table 2.1: Simulation parameters for the 2D drift-diffusion model for LT-GaAs

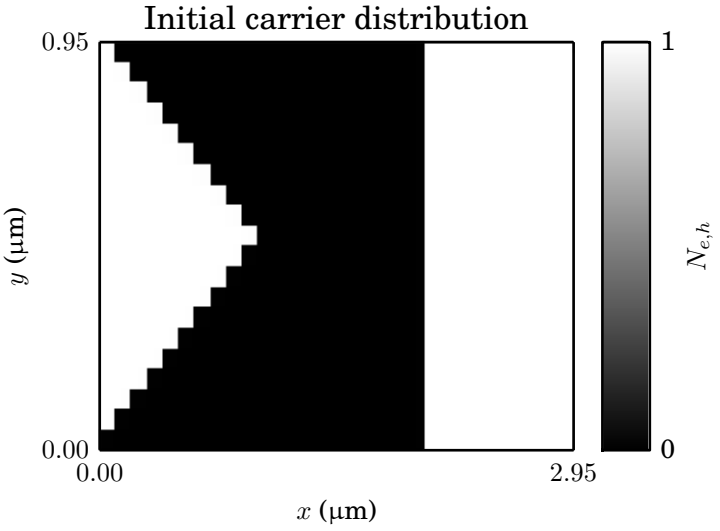

Figure 2.5: The initial density distribution of N_e and N_h

the matrix. For example, if the calculation of $n_{i,j}$ relied on the calculation of $n_{i-1,j}$ and the element to be calculated was $n_{0,0}$, then the element $n_{i-1,j}$ would be $n_{N,0}$ where N is the size of the matrix.

At the beginning of the program, the size of the simulation grid is defined as N_x and N_y in the x and y directions respectively. Matrices are created with these lengths and widths, all initially filled with zeroes. Two are created for the scaled electron and hole densities, N_e and N_h, one for the scaled charge distribution ρ (simply defined as $N_h - N_e$), one for the potential distribution V and two for the electric field, E_x and E_y.

Once the matrices are defined, an arbitrary pattern can be used to define the initial concentrations of N_e and N_h, as the matrix can take any value from 0 to 1 to represent the initial carrier densities. In the tested emitters, the distribution of $G(x)$ is defined as a step function between 1 and 0 over a triangular area, as shown in figure 2.5 and $G(t)$ is defined as before as a Gaussian pulse in time. The placement of the unit cell is chosen to minimise diffusion over the cyclic boundary, reducing probable cause of errors in testing.

We define the scaling factors for the simulation so that the simulation takes place in dimensionless units. At the start of the simulation, the physical constants e, k_b ϵ_0 are defined, as well as the temperature T, the mobility of the semiconductor μ, the initial carrier concentration n_0 and the recombination time t_r, with $T = 300\,\mathrm{K}$, $\mu = 0.85\,\mathrm{m^2V^{-1}s^{-1}}$ and $t_r = 1\,\mathrm{ps}$. The value $n_0 = 1 \times 10^{20}\,\mathrm{m^{-2}}$ was chosen to correspond with the lower bound of excitation density based on previous simulations of carriers in GaAs [63]. The scaling factor for length, L, is defined within the simulation and

calculated according to equation 2.14:

$$L = \sqrt{\frac{e_0 k_b T}{e^2 n_0}}. \tag{2.19}$$

The scaling factor for time, defined as T_{scale} is calculated as

$$T_{scale} = \frac{\epsilon_0}{e n_0 \mu}. \tag{2.20}$$

The dimensionless recombination time T_r is obtained by $T_r = t_r / T_{scale}$, and the size of the unit cell and the value of $\mathrm{d}x$ are divided by L also. The value for $\mathrm{d}t$ is proportional to $\mathrm{d}x^2$, so as to scale with the size of the simulation. If $\mathrm{d}t$ becomes too large the simulation becomes unstable and exits without returning a value for j, scaling with $\mathrm{d}x^2$ prevents this from happening. When calculating the electric field from V by using $\vec{\nabla}V$, the value for $\vec{E}$ is multiplied by L to keep the result dimensionless as a result of the differential. The value for E is thus:

$$\vec{E} = L\vec{\nabla}V. \tag{2.21}$$

To find the values of $\mathrm{d}N_e$ and $\mathrm{d}N_h$ are found at each time step by first creating a matrix with all elements equal to zero for both $\mathrm{d}N_e$ and $\mathrm{d}N_h$. Then the calculation of

$$\mathrm{d}N_e = \vec{\nabla} \cdot \vec{E} N_e + \nabla^2 N_e - \frac{N_e N_h}{T_r} \tag{2.22}$$

and

$$\mathrm{d}N_h = -\frac{N_e N_h}{T_r} \tag{2.23}$$

is performed by iterating through the matrix co-ordinates i and j sequentially (respecting boundary conditions), obtaining values from E_y, E_x, N_e and N_h. The gradient operator $\vec{\nabla}$ is implemented by using differences to calculate the gradient with respect for the boundary conditions. The calculation for the difference of carriers $\mathrm{d}N_{ei,j}$ and holes $\mathrm{d}N_{hi,j}$ becomes:

$$\begin{aligned} \mathrm{d}N_{ei,j} = \quad & (N_{ei+1,j}E_{xi+1,j} - N_{ei-1,j}E_{xi-1,j} + N_{ei,j+1}E_{y_{i,j+1}} - N_{ei,j-1}E_{y_{i,j+1}})/2\mathrm{d}x \\ + \quad & (N_{ei+1,j} + N_{ei-1,j} + N_{ei,j+1} + N_{ei,j-1} - 4N_{ei,j})/\mathrm{d}x^2 \\ - \quad & (N_{ei,j}N_{hi,j})/T_r \end{aligned} \tag{2.24}$$

and

$$\mathrm{d}N_{hi,j} = -\frac{N_{ei,j}N_{hi,j}}{T_r}. \tag{2.25}$$

The values of $\mathrm{d}N_e$ and $\mathrm{d}N_h$ are then added to N_e and N_h, and the simulation steps forward by one time step $\mathrm{d}t$.

The current density j is found from the diffusion of N_e by using equation 2.2. First the gradient of $\vec{E}N_e$ is calculated in the x and y directions, summed over the whole matrix and then multiplied by $n_0 \mu k_b T \mathrm{d}x^2$ giving the total current in units of Cs^{-1}.

2.3.1 Jacobian Calculation of Electric Field

In the two dimensional implementation of the diffusion model, determining the electric field from the charge distribution was not a straightforward case of integrating Gauss's law as in the one dimensional case. Instead the potential V of the charge distribution was obtained, with E being calculated as $\vec{\nabla}V$. Using this implementation Gauss's law becomes Poisson's equation,

$$\nabla^2 V = \frac{e(n_e - n_h)}{\epsilon_0}. \tag{2.26}$$

The first implementation of solving the Poisson equation used a Jacobi method using Successive Over-Relaxation (SOR). This was done by copying the matrix containing ρ into the potential matrix V. For each element in V, the element was updated using the average of four neighbouring elements, so that:

$$V_{i,j} = \frac{V_{i+1,j} + V_{i-1,j} + V_{i,j+1} + V_{i,j-1}}{4}, \tag{2.27}$$

Which is a solution to the Poisson equation, as for the second partial differential term can be approximated as

$$\frac{\partial^2 V(x,y)}{\partial x^2} = \frac{V(x-h) - 2V(x) + V(x+h)}{h^2}, \tag{2.28}$$

where h is a small displacement. As the Laplace operator ∇^2 is expressed as:

$$\nabla^2 V(x,y) = \frac{\partial^2 V}{\partial x^2} + \frac{\partial^2 V}{\partial y^2} \tag{2.29}$$

which can then be approximated to:

$$\nabla^2 V(x,y) = \frac{V(x-h,y) + V(x+h,y) + V(x,y-h) + V(x,y+h) - 4V(x,y)}{h^2} \tag{2.30}$$

and rearranged to give

$$V(x,y) = \frac{V(x-h,y) + V(x+h,y) + V(x,y-h) + V(x,y+h) - h^2\nabla^2 V(x,y)}{4}. \tag{2.31}$$

The term $h^2\nabla^2 V(x,y)$ is then ignored due to h^2 being vanishingly small. Each element was updated sequentially, along each row and then each column while respecting the cyclic boundary conditions, using the previously calculated values of $V_{i,j}$. The process was continued until the matrix V showed suitable convergence, and then the gradient of V was obtained by calculating the slope of V in the x and y directions. The difficulty arising with this method of obtaining the potential distribution was that solving each step grew as $\mathcal{O}(n^2)$ and had to be done until convergence to a solution occurred. This was unsatisfactory due to most computing time required to recalculate the potential distribution. Attempts were made to increase convergence in equation 2.27 by adding an arbitrary constant α, so

$$V_{i,j} = \frac{V_{i+1,j} + V_{i-1,j} + V_{i,j+1} + V_{i,j-1}}{4} + \alpha. \tag{2.32}$$

Convergence was still too slow for simulation purposes. A more useful implementation based on Fourier transforms was used to compute the solution to the Poisson equation.

2.3.2 Fourier Calculation of Electric Field

If a one dimensional potential distribution $V(x)$ can be written in terms of wave vector components $\hat{V}(k)$ with the forward and inverse Fourier transforms, $\mathcal{F}$ and $\mathcal{F}^{-1}$.

$$V(x) = \mathcal{F}^{-1}(\mathcal{F}(V(x))) = \int_{-\infty}^{\infty} \hat{V}(k) e^{-i2\pi(xk)} \mathrm{d}k, \tag{2.33}$$

Introducing the Laplace operator ∇^2 gives

$$\nabla^2 V(x) = \frac{\rho}{\epsilon_0} = \iint_{-\infty}^{\infty} \nabla^2 \hat{V}(k) e^{-i2\pi(xk_1 + yk_2)} \mathrm{d}k_1 \mathrm{d}k_2, \tag{2.34}$$

which leads to:

$$\frac{\rho}{\epsilon_0} = \iint_{-\infty}^{\infty} -4\pi^2(k_1^2 + k_2^2) \hat{V}(k) e^{-i2\pi(xk_1 yk_2)} \mathrm{d}k_1 \mathrm{d}k_2. \tag{2.35}$$

Continuing rearrangement leads to an expression for $V(x)$ in terms of ρ:

$$\frac{\rho(x)}{\epsilon_0} = \mathcal{F}^{-1}(-4\pi^2(k_1^2 + k_2^2)\mathcal{F}(V(x))), \tag{2.36}$$

leading to

$$V(x) = -\frac{1}{4\pi^2\epsilon_0}\mathcal{F}^{-1}\left(\frac{\mathcal{F}(\rho(x))}{k_1^2 + k_2^2}\right). \tag{2.37}$$

The 2D Fourier transform also assumes periodic boundary conditions which is ideal in this case. Without need for iteration, the Fourier method provides the potential V, and thus the electric field in a much smaller amount of time compared with the Jacobi method. The Fourier method scales with the problem as $\mathcal{O}(n\log(n))$, making this an efficient way of finding the potential from an arbitrary charge distribution. In a two dimensional grid of size L_x and L_y with spacing h between points, equation 2.37 becomes:

$$V(x,y) = -\frac{L_x L_y}{h4\pi^2\epsilon_0}\mathcal{F}^{-1}\left(\frac{\mathcal{F}(\rho(x,y))}{k_1^2 + k_2^2}\right). \tag{2.38}$$

This method could also be used to simulate the diffusion of the carriers, which is the classical solution to the heat equation where the carrier density as a result of diffusion is the convolution of the initial function with a Gaussian kernel. However for the simulation we chose to carry over the iterative solution for the one dimensional model, determining the gradient numerically with each step.

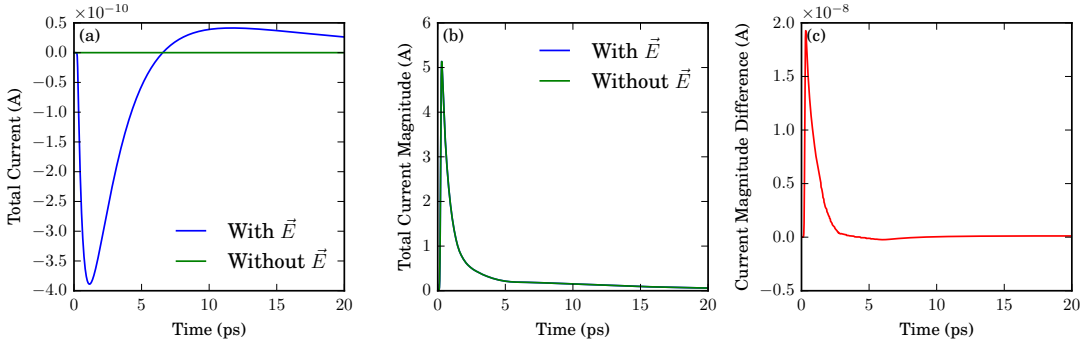

Figure 2.6: Comparison of total current simulated in the 2D unit cell with time, showing the effect of the electric field $\vec{E}$. The total current density is integrated over dx and dy to show (a) the total current and (b) the magnitude of the current. The difference between the simulated current with and without the electric field $\vec{E}$ is a factor of 10^{-8} and considered negligible. (c) shows this difference in current magnitude.

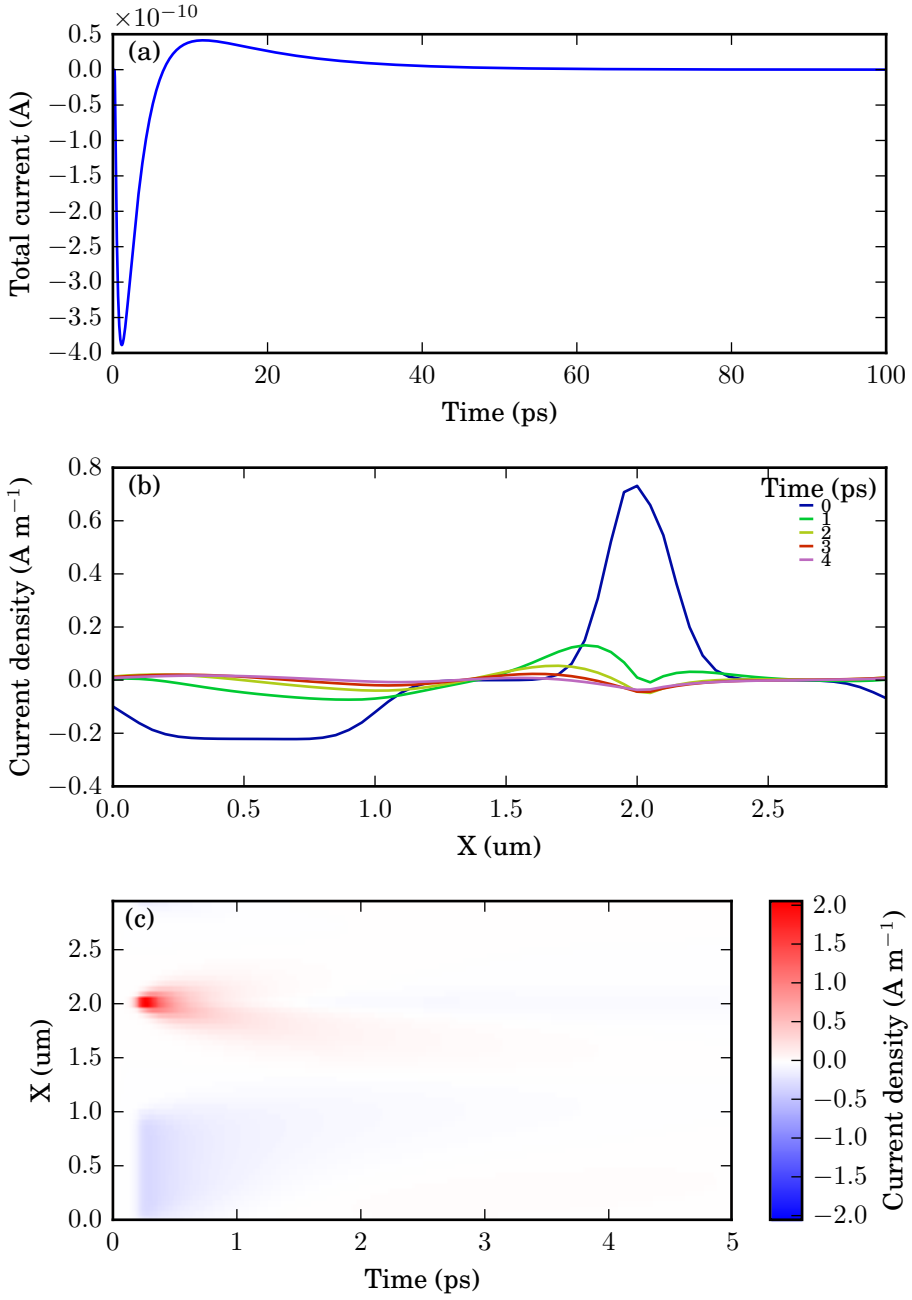

Figure 2.7: Current density from simulating the 2D array of triangular emitters. (a) shows the total current integrated over the unit cell with time. (b) shows the sum of the current density j over the y axis plotted against x for various times. (c) shows the same data as an image map, showing the sum of j over y plotted against time.

2.4 Results of the Two-Dimensional Model

From our 2D model we found that from creating an array of triangular emitters we were able to create a net current, shown in figure 2.6 using the simulation parameters specified in table 2.1 on page 25. This current is only observable when taking into account the effect of the electric field on the carriers; removing the term $\vec{E}$ in equation (2.2) and equation (2.4) results in no net current. Figure 2.7 (a) shows the total current generated in the unit cell with time and figure 2.7 (b) and (c) shows the current density j summed over the y axis to show the current density along the axis of the emitter with time. From the simulation we can see that large surge current created by the optical pulse envelope, causing carrier to diffuse at 0.2 ps. Figure 2.6 shows a higher current density in one dimension at the high-contrast boundary at $X = 2\,\mu\text{m}$, compared to the low contrast triangular regions between $X = 0$–$1\,\mu\text{m}$. A more detailed inspection of each variable in the simulation is included in figure 2.8. Initially from this we concluded that a net current was feasible for a set of triangular emitters and started fabricated triangular based masks using photo-lithography. However when tested in the THz-TDS experiment no detectable current was observed from the patterned triangular emitters. The cause for this is likely due to the relative difference in strengths of the current arising from the electric field compared with the current from diffusion. As shown in figure 2.6, the total current per unit cell is 10^8 less than the magnitude of the total current. This generated current is insignificant to the total current density, which is dominated by the diffusion term. As a result we concluded that the process that governed the LPD effect was not due to the creation of a net current, but a process that involved the interaction of the emitted radiation with the metal. From this we investigated the interaction of the emitted terahertz emission from the simulated current with a gold mask.

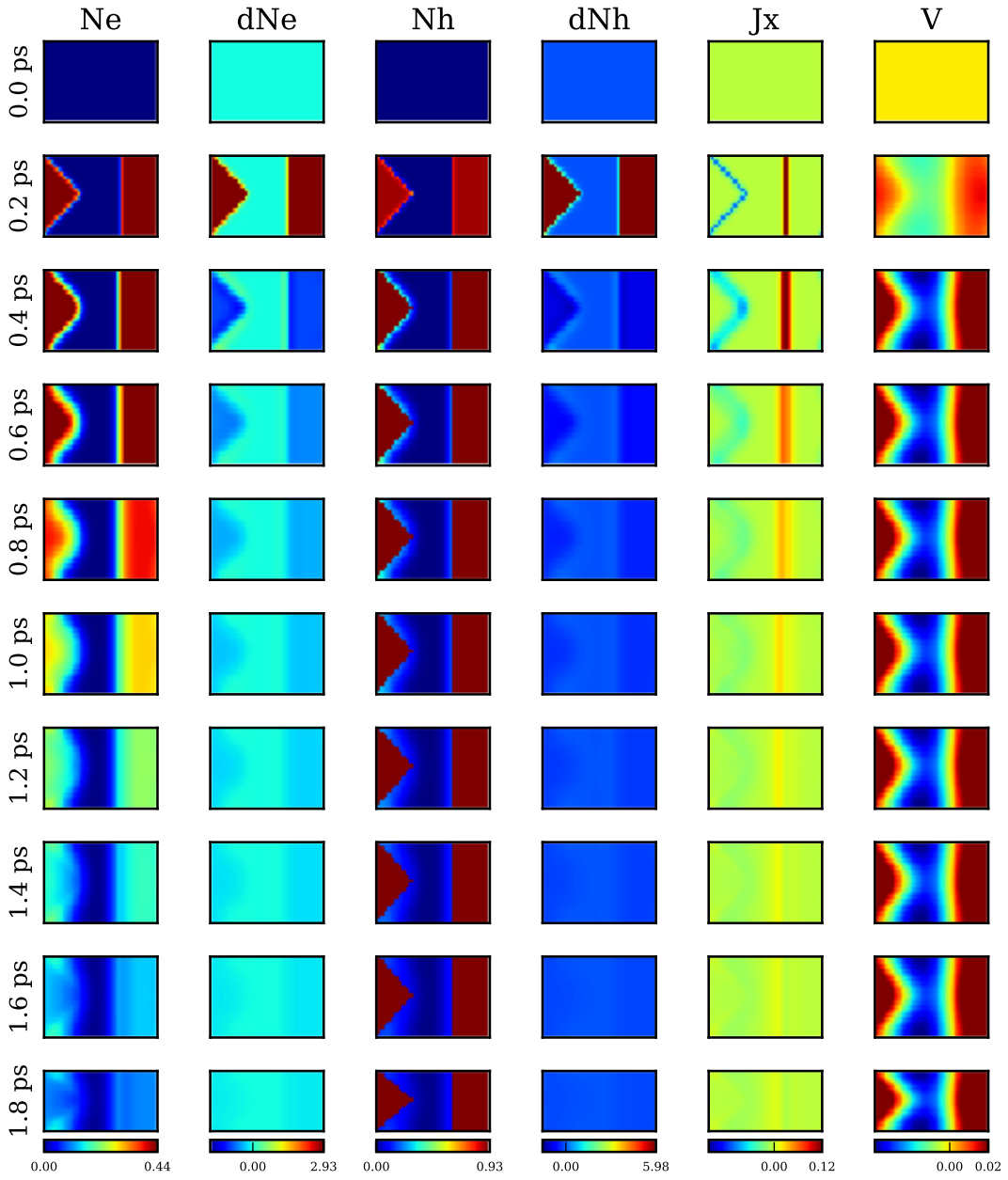

Figure 2.8: A figure showing the full evolution of the variables in time specified in the 2D simulation described in chapter 2. The variables N_e, dN_e, N_h, dN_h, j_x and V are shown as two-dimensional images over a period of 2 ps, with the optical pulse arrival at 0.2 ps. The x and y axis of each image are 3 µm and 0.8 µm respectively. In the simulation we can see the generation of carriers occurring between 0–0.2 ps due to the optical pulse. During this time, carriers are diffusing away from the initial distribution, most visible in j_x at 0.4 ps. Past 0.2 ps the carrier generation decreases and the electron concentration decreases. At 1.6 ps there are more carriers outside the hole region as a result of diffusion and recombination. The current density in j_x reverses direction as a result, with electrons flowing back into the hole distribution and recombining.

2.5 One Dimensional Model

We started creating the model simulating the current density $\vec{j}$ in one dimension. The equations 2.6, 2.3 and 2.7 are rearranged so that the change in N_e N_h and $\vec{E}$ are

$$\mathrm{d}N_e = \frac{\mathrm{d}N_e\vec{E}}{\mathrm{d}x} - \frac{\mathrm{d}^2N_e}{\mathrm{d}x^2} - \frac{N_eN_h}{\tau_r} - \frac{N_e}{\tau_t} + G(t,x), \tag{2.39}$$

$$\mathrm{d}N_h = -\frac{N_eN_h}{\tau_r} \tag{2.40}$$

and

$$\vec{E} = \int_b^a N_h - N_e\mathrm{d}x \tag{2.41}$$

The result for N_e and N_h is updated as

$$N_e = N_e + \mathrm{d}N_e\mathrm{d}t \tag{2.42}$$

and

$$N_h = N_h + \mathrm{d}N_h\mathrm{d}t. \tag{2.43}$$

At the start of the simulation, the matrices N_e and N_h are created, and define the initial hole and electron densities. Two matrices representing displacement x are also created; one for displacement in the $+x$ direction and one for $-x$. The matrix representing $-x$ is a range from 1 to M, and the matrix for $+x$ is from the range $M+1$ to $2M$. This is to avoid any discontinuity with the electric field when approximating the integral as a sum, which is

$$\vec{E}_j^- = \sum_{i=-M}^{j} (N_{ei} - N_{hi}) \tag{2.44}$$

in $-x$ and

$$\vec{E}_j^+ = \sum_{i=j}^{M} (N_{ei} - N_{hi}) \tag{2.45}$$

in $+x$.

The evolution of N_e, N_h and $\vec{E}$ are repeatedly updated through each time step $\mathrm{d}t$, which is chosen as $\mathrm{d}t \propto \mathrm{d}x^2$. The diffusion length is found by plotting the matrix N_e with displacement x, and measuring the distance over which diffusion occurs. If we define $G(x)$

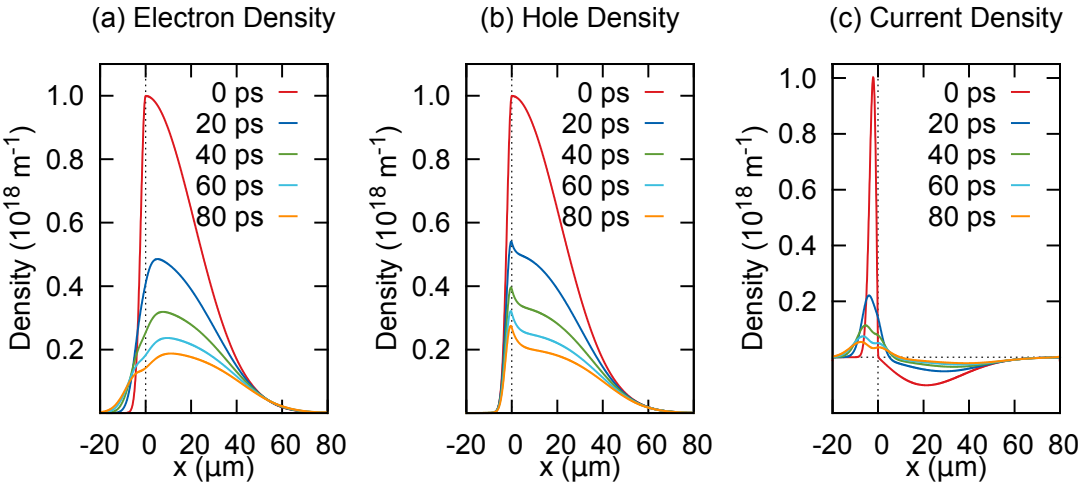

Figure 2.9: Results from the one dimensional model as presented in [3] showing the time evolution of the electron (a), hole densities (b), and current density (c). The dotted line at $x = 0$ represents the mask boundary, with $x < 0$ representing the unmasked semiconductor. A high current density is apparent near the gold mask. Carriers have kinetic energy corresponding to 3000 K to exaggerate the diffusion effect.

as a half-Gaussian function, we can simulate the carrier diffusion as described by Klatt et al for a pulse focussed on the edge of a metal emitter as shown in figure 2.9 which shows the change in N_e, N_h and j with time. Figure 2.9 shows the diffusion of carriers using the parameters specified in table 2.1 (page 25) extending over the barriers, with the very large change in initial current density shown in figure 2.9. A noticeable effect is the increased hole density at $x = 0$ caused by the high degree of diffusion near the metal mask. Due to the large current density $\vec{j}$ near the boundary electrons diffuse away from the hole concentration resulting in less electrons compared to holes. This limits the recombination rate, causing the slight increase of N_h near the boundary. The total current of the one dimensional model integrates to zero only considering the current due to carrier diffusion. The net current observable per unit cell is due to the drift caused by the electric field component, which is much weaker compared to the magnitude of the diffusion current [3].

2.6 Integration of 1D Model with COMSOL

We investigated the current that the original drift-diffusion current produced thought to be responsible for the lateral photo-Dember emission due to the Klatt et al. hypothesis. The simulated current due to the electric field created by the separated charge was insignificant compared to the carrier diffusion. We used the output of the one-dimensional simulation to create a time-domain COMSOL simulation of the lateral photo-Dember effect [3]. The microscopic current simulated is created by a partially masked Gaussian carrier

distribution as shown in figure 2.9. The COMSOL simulation, as shown in figure 2.10, calculates the electromagnetic wave produced by the electron and hole diffusion in time.

The COMSOL model describes a semiconductor, modelled as a dielectric, partially masked by a gold mask, with the time-dependent current located below the surface of the gold mask as shown in figure 2.10. The gold layer was modelled as a perfect electric conductor so that the dipole quenching effect would be exaggerated. We took the output of the simulated current from the one dimensional current and used this as a time-dependent COMSOL variable of current density within a one-dimensional wire 1 µm below the surface of the semiconductor. This would simulate the current produced within the semiconductor by an optical laser pulse and take into account the recombination of carriers. The time-variant current produces a propagating electromagnetic pulse through the semiconductor proportional to the time derivative of the current $\frac{\partial \vec{j}}{\partial t}$. We tested the case for both masked (figure 2.10(a)) and unmasked (figure 2.10(b)) cases to view the effect of the interaction of the terahertz emission with the metal surface. The unmasked semiconductor as shown in figure 2.10(b) does not experience any dipole quenching from a mask, and radiates a terahertz pulse in a quadrupole pattern. This quadrupole pattern produces no observable terahertz emission in the direction normal to the semiconductor surface, but produces emission that propagates at 45° to the surface normal. The masked semiconductor in figure 2.10(a) demonstrates the effect of dipole quenching. The current that diffuses under the mask produces a terahertz pulse that is reflected by the mask and self interferes, and is quenched. This allows the dipole in the unmasked region to radiate, producing observable emission parallel to the surface normal.

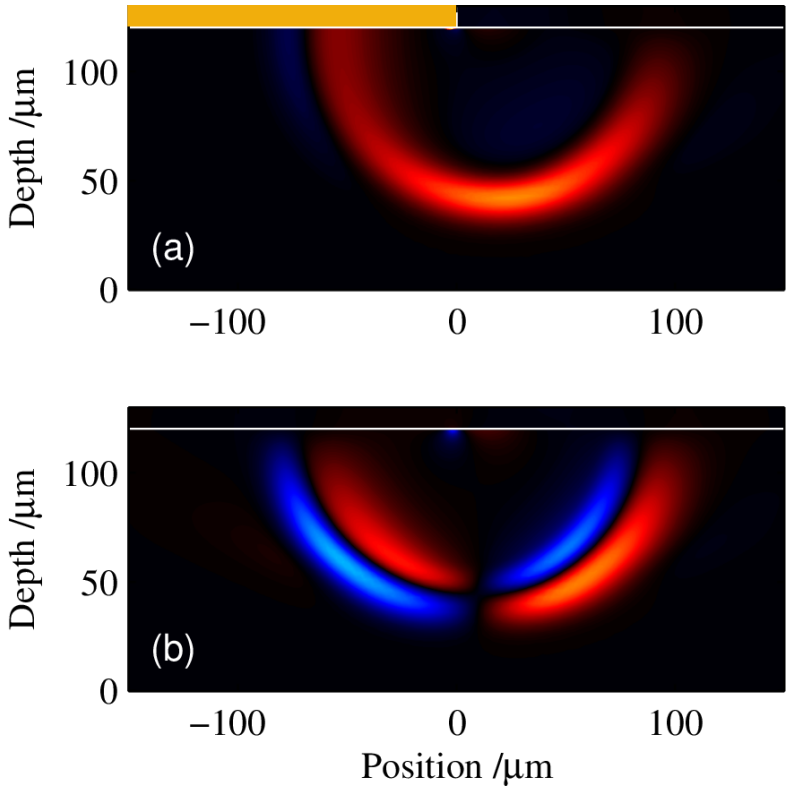

Figure 2.10: A COMSOL model of the dynamic electric field along the z axis produced by the drift-diffusion model after an asymmetric carrier distribution is created with the one dimensional model. Red is the positive field, blue negative values. Figure (a) shows a partially masked semiconductor with gold, shown as a yellow rectangle and (b) an unmasked semiconductor. Figure (b) shows the terahertz emission radiating in a quadrupole patterns, producing no electric field parallel to the surface normal.

2.7 Bimolecular Recombination Time

The drift-diffusion model so far assumes that the recombination time of the carriers, represented as $\frac{N_e N_h}{\tau_r}$, is the same as the total carrier lifetime given in semiconductor literature. While this is true for the trap time of the electrons, represented as $\frac{N_e}{\tau_t}$, the recombination units are not physical if given in unites of seconds. Mark Barnes undertook work to correct the simulation using the bimolecular recombination time given within semiconductor literature [61]. The bimolecular recombination time b replaces the term $\frac{N_e N_h}{\tau_r}$, altering to the rate of change in n_e to

$$\frac{\partial n_e}{\partial t} = \mu \frac{\partial n_e \vec{E}}{\partial x} + D \frac{\partial^2 n_e}{\partial x^2} - b(n_e n_h) - \frac{n_e}{\tau_t} + G(x,t) \tag{2.46}$$

where $b = 20 \times 10^6\,\mathrm{cm\,s^{-1}}$. In the case of intrinsic semiconductors without recombination due to trap states the capture rate τ_t can be omitted. After taking into account the correct change the results of the newly-scaled simulation do not change significantly.

The time used for the carrier recombination in table 2.1 (page 25) for τ_r equates to $1 \times 10^{10}\,\mathrm{cm\,s^{-1}}$, meaning that the simulation run over-estimates the effect of carrier recombination. However as the carrier recombination only serves to influence the effect on the electric field, the results from the simulation are still valid as the contribution from the intrinsic electric field was originally negligible; the decreased recombination makes this increasingly negligible.

2.8 Conclusion

In this section we have demonstrated the creation of a drift-diffusion simulation used to create the current density distribution within a semiconductor from an arbitrary patterns of carrier distributions. We take into account the diffusivity, the recombination of carriers and the resulting electric field that this creates. The electric field does to the intrinsic recombination of carriers, while small, does create a net current in the unit cell. This net current however is dominated by the diffusion term, and we have shown that a one dimensional current distribution can produce terahertz emission by the LPD effect.

Chapter 3

Single Lateral Photo-Dember Emitters

Within this chapter we investigate the choice of semiconductor substrate for LPD emitters. In a typical THz-TDS photoconductive antennas are used as coherent pulsed terahertz sources. Frequently photoconductive antennas are fabricated from low-temperature grown (LT) GaAs or InGaAs with the band-gap of the semiconductor chosen to match the photon energy of the source laser. Semiconductors with high mobilities and short carrier lifetimes are chosen for ideal performance as terahertz emitters to increase the rate of change of the microscopic current with time, $\frac{\partial \vec{j}}{\partial t}$. The long carrier lifetime of SI-GaAs restricts the available bandwidth within terahertz generation and detection, but can be reduced by lowering the growth temperature, creating LT GaAs [69, 70]. LT-GaAs is a commonly used material within photoconductive switches due to its 1.423 eV direct band gap [67] providing compatibility with 800 nm Ti:Sapphire laser systems and its sub-picosecond carrier lifetime [65, 68, 71]. Such a material matches well with the requirements of the LPD emitter, where the terahertz generation also depends on high mobility and short carrier lifetime, compared with the materials shown in Table 3.1. As the conversion efficiency of optical power to terahertz radiation is less than that of photoconductive antennas, optical saturation within a small illuminated area is a

Material	Carrier Lifetime (ps)	Mobility ($\mathrm{cm\,V^{-1}\,s}$)
Cr:doped GaAs	50–100	1000 [65]
Ion-implanted InP	2–4	200 [65]
Ion-damaged SOS	0.6	30 [65]
Amorphous Si	0.8–20	1 [65]
MOCVD CdTe	0.45	180 [65]
$In_{0.52}Al_{0.48}As$ (MBE 150 °C)	0.4	5 [65]
Semi-Insulating GaAs	10–100 [66]	8000 [67]
Annealed LT GaAs (MBE 200 °C	0.3	120–150 [68]

Table 3.1: Carrier mobility and lifetime for various semiconductors

limiting factor compared with photoconductive antennas. In this chapter we characterise the performance of LPD emitters on SI and LT-GaAs substrates, both annealed and unannealed and observe saturation effects with optical fluence. The short carrier lifetime is of more critical value for a photoconductive receiver rather than a photoconductive generator. In a photoconductive receiver the reduction of carrier lifetime increases the bandwidth of the detector, whereas for a photoconductive generator the majority of the bandwidth comes from the surge of current created during optical generation, relying on the short bandwidth of the optical pulse.

3.1 Use of LT-GaAs in Terahertz Emitters

The desire of using LT-GaAs substrates in terahertz detectors and emitters stems from the requirement for low carrier lifetime. Reducing the carrier lifetime increases the transient response for terahertz detectors allowing for higher detected bandwidth [73]. Most of the bandwidth during terahertz emission originates from the carrier generation surge at the start of photo-excitation within the semiconductor, rather than carrier capture [72]. LT-GaAs is still used in photoconductive antenna generators where the shorter carrier lifetime avoids saturation with optical fluence and higher breakdown fields. Lower lifetime of the carriers creates a faster rate of change of current $\frac{\partial \vec{j}}{\partial t}$ resulting in increased spectral bandwidth from the terahertz emitter and increased amplitude [68, 73]. GaAs is well suited to ultra fast applications where sub-picosecond carrier lifetimes can be controlled at manufacture by adjusting the growth temperature.

LT-GaAs is usually grown with Molecular Beam Epitaxy (MBE). High purity gallium and arsenic (or other high purity elements) are heated within effusion cells under high vacuum. These effusion cells create molecular beams that are directed at a rotating heated SI-GaAs wafer. The flux from each effusion cell can be adjusted to achieve the desired flux of each element to be deposited on the substrate. Growth of GaAs at 600 °C and above creates a defect-free crystalline structure, whereas lower growth temperatures of ∼200 °C create defects. The lower growth temperature results in defect sites being created by incorporating excess arsenic as anti-sites, forming small continuous regions of arsenic embedded within the metal [74, 75], acting as buried Schottky barriers [76]. The defect sites reduce the carrier lifetime by adding energy levels within the band gap providing alternative recombination pathways for carriers as shown in figure 3.1. Carriers can either be trapped by the defect sites and scatter back into the valence band, or recombine, or be excited from trap states. As a result different recombination pathways for carrier generation and annihilation exist. The trap lifetime is much shorter than the carrier recombination lifetime [70]. Due the different carrier lifetimes trap states can become saturated with carriers if the rate of depletion from the trap state (τ_1 in figure 3.1) is less than the increase of carriers combining into the trap state (τ_2)

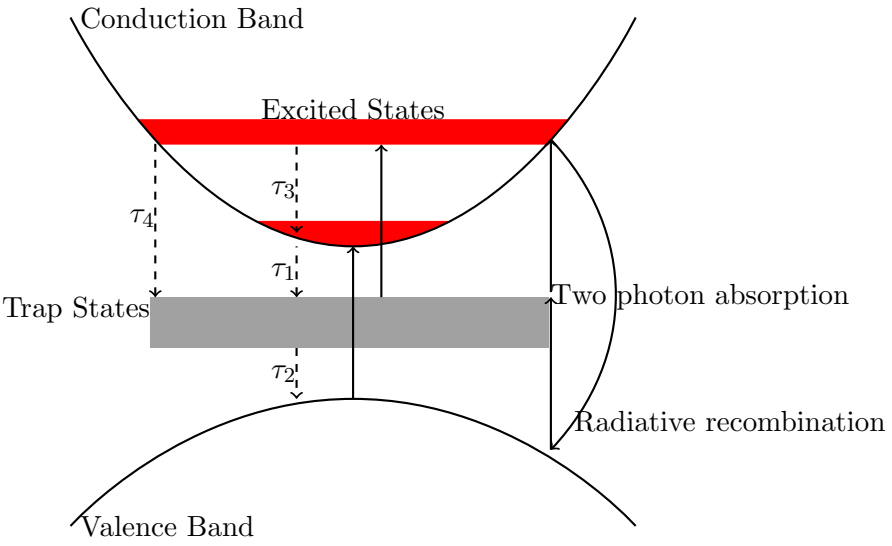

Figure 3.1: Illustration showing the excitation and relaxation pathways in GaAs. Carriers can be both excited from the valence band and mid gap trap states, and decay through the mid-gap states. Excitation from the mid-gap states can produce a larger carrier concentration compared with just band-to-band absorption [76]. The mid-gap states are created by low temperature growth to decrease the capture times τ_1 and τ_2.

Photoconductive antennas frequently use annealed LT-GaAs to increase the difference in dark and light resistance which minimizes dark currents within a photoconductive receiver and allows large external biases. Annealing is done by quickly heating and cooling the LT-GaAs. Unannealed LT-GaAs suffers from low dark resistivity ($\sim$10 Ω cm) due to conduction from excess arsenic that forms the trap states [77]. Annealing the samples at high temperatures creates precipitates from the excess arsenic [78], causing the As to cluster increasing the distance between traps. The increased distance reduces carrier "hopping" or tunnelling between the traps, increasing the resistivity. Annealing at 600 °C increases the resistivity by five orders of magnitude but carrier lifetime changes from 90 fs to 1.6 ps [79]. This is vital for photoconductive switches where low resistivity results in decreased emitter lifetime. However in diffusion based emitters, such LPD emitters, the dark resistivity does not matter as there is no applied bias.

The LPD emitter's conversion efficiency is less compared with conventional photoconductive antennas due to relying on intrinsic carrier diffusion rather than an applied voltage. As a result to achieve comparable terahertz output with photoconductive antennas the optical fluence has to be increased. Typically in a THz-TDS system optical power on a photoconductive emitter is typically limited to roughly 10 mW with a laser spot size 10 µm on each antenna [72, 80]. The limited fluence places a minimum constraint on spot size, as the optical beam needs to be centred within the electrodes of the photoconductive emitter. Increasing the optical fluence leads to device degradation [58] and surface ablation. However in a THz-TDS using a titanium sapphire laser the output power is of the order of 1 W, resulting in most of the output power not being used for terahertz

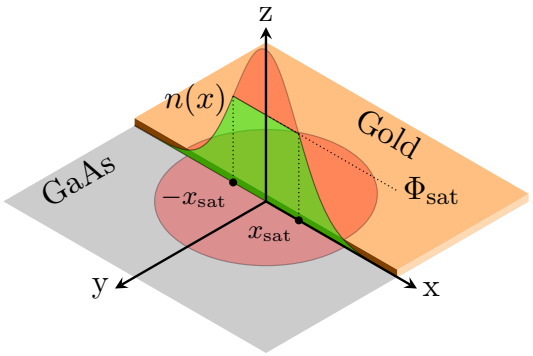

Figure 3.2: A schematic showing the distribution of photo-generated carriers within the semiconductor. Only carriers generated near the metal boundary contribute to the terahertz emission.

generation. Using a large scale emitter removes the spot size limitation allowing more of the input optical power to be used.

Terahertz emitters based on the lateral photo-Dember effect do not require a difference in light and dark resistance due to the lack of external bias. The parameters that affect the terahertz emission is expected to be the difference in mobilities of the carriers and the carrier lifetime, which is dominated by the trapping time of the material.

3.2 Fitting Model

To determine the fluence at which saturation occurs a simple one dimensional model based on the geometry of the single edge LPD emitter was created. In the lateral photo-Dember effect the total current that will contribute to the terahertz emission is proportional to the difference of carrier concentration on the metal edge, where it is highest, to the edge of the optical spot, where it is zero. Thus the generated terahertz is proportional to the carrier concentration along the metal boundary. The model assumes that only the optical fluence along the metal boundary contributes to the terahertz emission. Carrier generation that occurs beyond the boundary creates a dipole parallel to the surface normal that produces no lateral current and so does not contribute to the terahertz emission. It is assumed that the terahertz emission is proportional to the rate of change in the carrier density within this one dimensional region, and that the carrier density is a function of the pulse fluence. In our model we assume that the number of carriers generated is proportional to the fluence of the beam up to a maximum value of Φ_{sat}, which is a single point of optical saturation. The fluence Φ of the pump beam with average power p and radius r can be spatially described as a Gaussian, and so the fluence along the border for a centred beam spot is

$$\Phi(x) = \frac{p}{2\pi r^2} \exp\left(-\frac{x^2}{2r^2}\right).$$

As stated previously it is assumed that the carrier density n is proportional to the fluence which saturates at Φ_{sat}. This creates a Gaussian distribution of carrier density that is clipped at Φ_{sat} within the range of x_{sat} and $-x_{\text{sat}}$, which is,

$$n(p, r, x_{\text{sat}}, x) \propto \begin{cases} \frac{p}{2\pi r^2} \exp\left(-\frac{x_{\text{sat}}^2}{2r^2}\right), & \text{for } |x| < x_{\text{sat}}; \\ \frac{p}{2\pi r^2} \exp\left(-\frac{x^2}{2r^2}\right), & \text{for } |x| > x_{\text{sat}}. \end{cases} \tag{3.1}$$

The integration of this function represents the sum of carriers along the boundary, N. We assume the terahertz emission is proportional to the rate of change of carriers, $\frac{\partial N}{\partial t}$, we can state that the terahertz emission E_{THz} is proportional to N. By integrating Equation 3.1 it can be shown that the total number of carriers as a function of power p and spot radius r is

$$\begin{aligned} E_{\text{THz}}(p, r, \Phi_{\text{sat}}) \propto & 2\sqrt{2} r \Phi_{\text{sat}} A + \frac{1}{\sqrt{2\pi}} \frac{p}{r} \operatorname{erfc}(A), \\ A = & \mathbb{R}\left(\sqrt{\ln\left(\frac{p}{2\pi\Phi_{\text{sat}} r^2}\right)}\right). \end{aligned} \tag{3.2}$$

$\mathbb{R}(f(x))$ is the real part of the function $f(x)$.

This is the term fitted to our results for determine Φ_{sat}, where E_{THz} is the spectral intensity. When the optical fluence is varied with constant spot radius r and increasing power p, E_{THz} saturates. Note that the model does not determine the mechanism of the saturation effect, only to attempt to determine the fluence at which it occurs. The model defines saturation as being an immediate cap on optical fluence, whereas a more realistic model could be created by using a gradual saturation in fluence up to Φ_{sat}. The saturation model assumes that there is a limit to the carrier density n that can occur within the region along the LPD boundary.

3.3 Fluence Dependency

To observe the effect of varying pump fluence on output terahertz emission a typical THz-TDS apparatus was used with a range of lateral photo-Dember emitters patterned on unannealed LT-GaAs, annealed LT-GaAs and SI-GaAs. A 80 MHz repetition rate Ti:Sapphire laser at 800 nm wavelength was used as the beam source with a commercial LT-GaAs (Menlo Tera T8) antenna used as a receiver. All LPD emitters were grown on a

(100) SI-GaAs substrate using undoped LT-GaAs. The LT-GaAs emitters consisted of a 1 µm layer of LT-GaAs grown at 230 °C on a 100 nm AlAs layer on a SI-GaAs substrate, with one emitter was annealed in-situ at 600 °C. Each sample was partially masked by gold to form a boundary between the gold and semiconductor as shown in figure 3.2. Varying the pump beam power and beam radius (defined as $1/e^2$ of the peak intensity) allows the optical fluence to be changed for each measurement of the terahertz pulse. The spectral intensity of the terahertz pulse was measured with fluence, calculated from the measured electric field in the time domain. The spectral intensity is defined as the sum of the real part of the Fourier transform in the time domain signal. Using the fitting model we attempted to determine the a value for optical saturation for each material tested.

Unannealed LT-GaAs demonstrates saturation with a fitted value of $\Phi_{\text{sat}} = 1.1 \pm 0.1\,\text{mJ}\,\text{cm}^{-2}$. Figure 3.3 (a) shows the time-domain traces from the terahertz scans grouped together by spot size and figure 3.3 (b) measured as terahertz pulse intensity with optical fluence. Out of the materials tested, the LT-GaAs functions as the most powerful emitter in terms of peak detected electric field, yielding the largest spectral intensity per terahertz pulse. A comparison of the maximum spectral intensity emitted by each LPD emitter is shown in table 3.2, categorised by material. The comparatively large terahertz pulse electric field is likely due to the trap states providing increased carrier generation in the LT-GaAs. The number of trap states in unannealed LT-GaAs are of the order of $1 \times 10^{19}\,\text{cm}^{-2}$, which are greater than the number of carriers generated [66]. As a result we expect the optical saturation to be very high as most carriers are captured from the trap states. This is supported by the lack of observable saturation of terahertz power with optical fluence in figure 3.3 (b), but the change in pulse shape in figure 3.3 (a) indicates a change in carrier dynamics before power saturation. A change in terahertz pulse shape takes place past the initial terahertz pulse shown in figure 3.3 (a) at $r = 11$ µm at 2 ps at optical fluences above $100\,\mu\text{J}\,\text{cm}^{-2}$. The two points shown as empty circles in figure 3.3 (b) are excluded from the saturation fit. At these points thermal damage on the sample surface was noted due to thermal ablation. The back reflection from the surface showed that the

Material	Maximum Spectral intensity (A.U.)	Optical Power p (mW)	Spot Radius r (µm)	Fluence ($\mu\text{J}\,\text{cm}^{-2}$)	Dynamic range (dB)
Unannealed LT-GaAs	2.22	300	15	520	21.5
Annealed LT-GaAs	1.42	300	30	131	23.7
SI-GaAs	0.818	240	23	34.2	24.5

Table 3.2: Table of the maximum spectral intensity recorded for each LPD emitter with optical fluence. Results are used from the data plotted in figure 3.4(a) for annealed LT-GaAs, figure 3.3(a) for unannealed LT-GaAs, figure 3.5 for SI-GaAs and figure 3.8 for dynamic range.

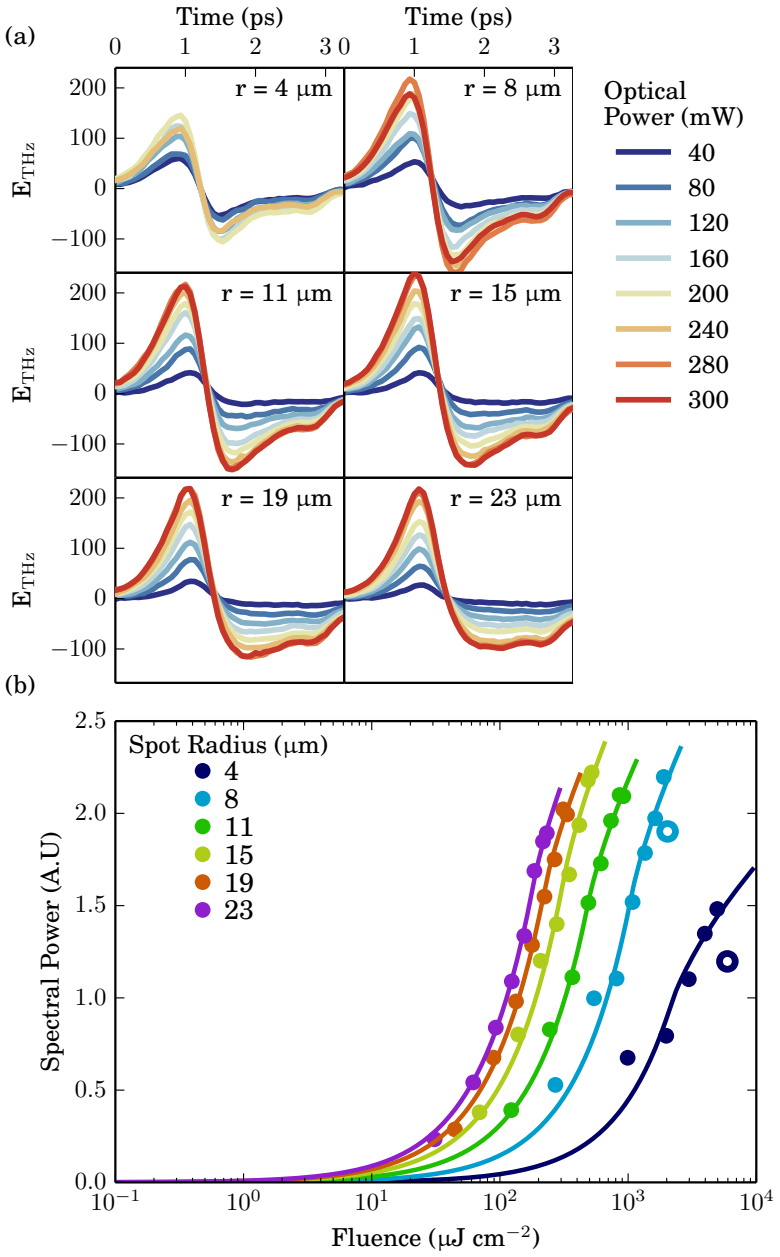

Figure 3.3: Unannealed LT-GaAs THz-TDS variation with optical fluence. Figure (a) shows the time-domain scans grouped by optical spot radius with increasing power as plots of the detected electric field with time. Figure (b) shows the spectral intensity from each time domain scan plotted with optical fluence with Equation 4.2 fitted. Circled points are excluded from the fit.

gold boundary was deformed and the GaAs surface was darker and less reflective. As a result we treat the saturation observed in figure 3.3 (b) due to thermal damage from the input laser pulse. While unannealed LT-GaAs demonstrates the highest spectral intensity, the dynamic highest range recorded is 2 dB lower compared with annealed LT-GaAs and SI-GaAs, as shown in figure 3.8. This reduction in dynamic range is likely due to feedback into the laser system from the LPD emitter surface, which has been noted as causing periodic drops in the recorded terahertz signal.

Annealed LT-GaAs (figure 3.4) demonstrates two distinct saturation domains of terahertz output power with fluence. Due to there being two regions of saturation, the fitting model in equation (4.2) does not produce any meaningful fitting. One saturation shoulder occurs at approximately $7\,\mu J\,cm^{-2}$ creating the shoulder observable in figure 3.4 (b). This shoulder is more pronounced when plotting the data as the first order derivative with fluence, as shown in figure 3.7 (e). At this saturation point the output terahertz power is greater than unannealed LT-GaAs and SI-GaAs, past this saturation point the terahertz output power increases again with optical fluence, demonstrating signs of saturation at $100\,\mu J\,cm^{-2}$ for spot radius above 20 µm. While the spectral intensity of annealed GaAs is less than unannealed GaAs, the optical efficiency is much higher. Figure 3.7 (b) shows the variation in the optical efficiency of annealed GaAs in comparison to unannealed LT-GaAs in figure 3.7 (a) and SI-GaAs in figure 3.7 (c). This high efficiency demonstrated at low optical fluence in figure 3.7 (c) allows the annealed LT-GaAs emitter sample to function as a lateral photo-Dember emitter with optical powers of less than 1 mW of optical power. Between the two saturation domains the time-domain terahertz signal changes, shown in figure 3.4(a). At $1\,\mu J\,cm^{-2}$ the electric field of the time domain terahertz pulse increases linearly from 3–6 ps whereas above $10\,\mu J\,cm^{-2}$ the electric field decreases and rises in this range. Annealing the sample reduces the total number of trap states to $1 \times 10^{18}\,cm^{-2}$, comparable to the number of excited free carriers. The change in carrier dynamics within annealed LT-GaAs with fluence has been observed with THz-TDS due to trap saturation [81]. This variation of carrier lifetime with fluence is compatible with the change of the time domain signal seen in figure 3.4(b). At low optical fluences, where the number of trap states is greater than the number of excited carriers, carrier lifetime is determined by the capture rate from the conduction band to trap states. As optical fluence increases, the trap states become fully occupied with carriers and the trap rate is decreased and becomes dependent on the recombination time from the trap state to the valence band. Increasing the optical fluence increases the recombination time of the carriers which affects the time domain past 3 ps, as shown in figure 3.4(a). In the rate equations described in Sosnowski et al. when saturation is reached more optical light is used to generate free carriers [81]. Since we expect the terahertz signal to be proportional to the number of free carriers, this also explains the abrupt change in pulse power shown in figure 3.4(b) at $10\,\mu J\,cm^{-2}$.

The SI-GaAs lateral photo-Dember emitter produces less intense terahertz emission than

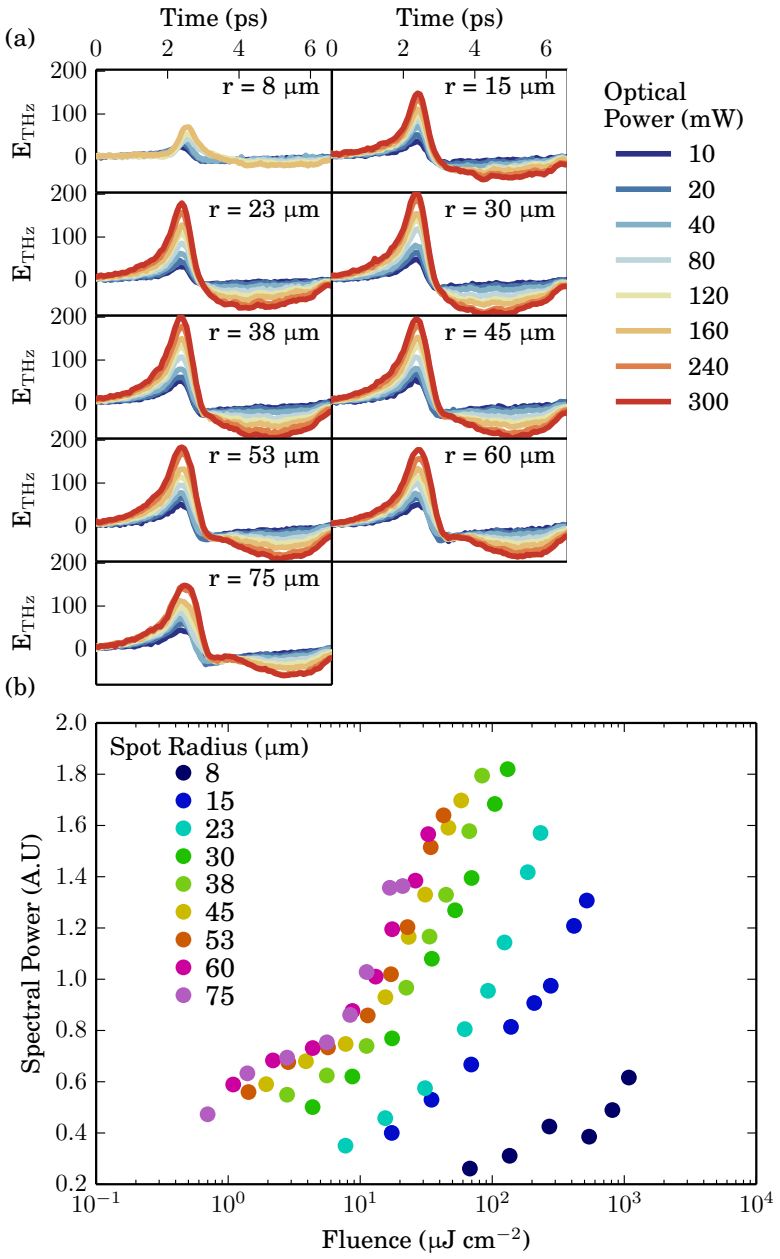

Figure 3.4: Annealed LT-GaAs THz-TDS variation with optical fluence. Figure (a) shows the time-domain scans grouped by optical spot radius with increasing power as plots of the detected electric field with time. Figure (b) shows the spectral intensity from each time domain scan plotted with optical fluence. The terahertz pulse's spectral intensity shows a saturation shoulder at a comparatively low fluence of $7\,\mu J\,cm^{-2}$, and continues to increase again at higher fluences. Note the change in the time domain pulse shape with fluence.

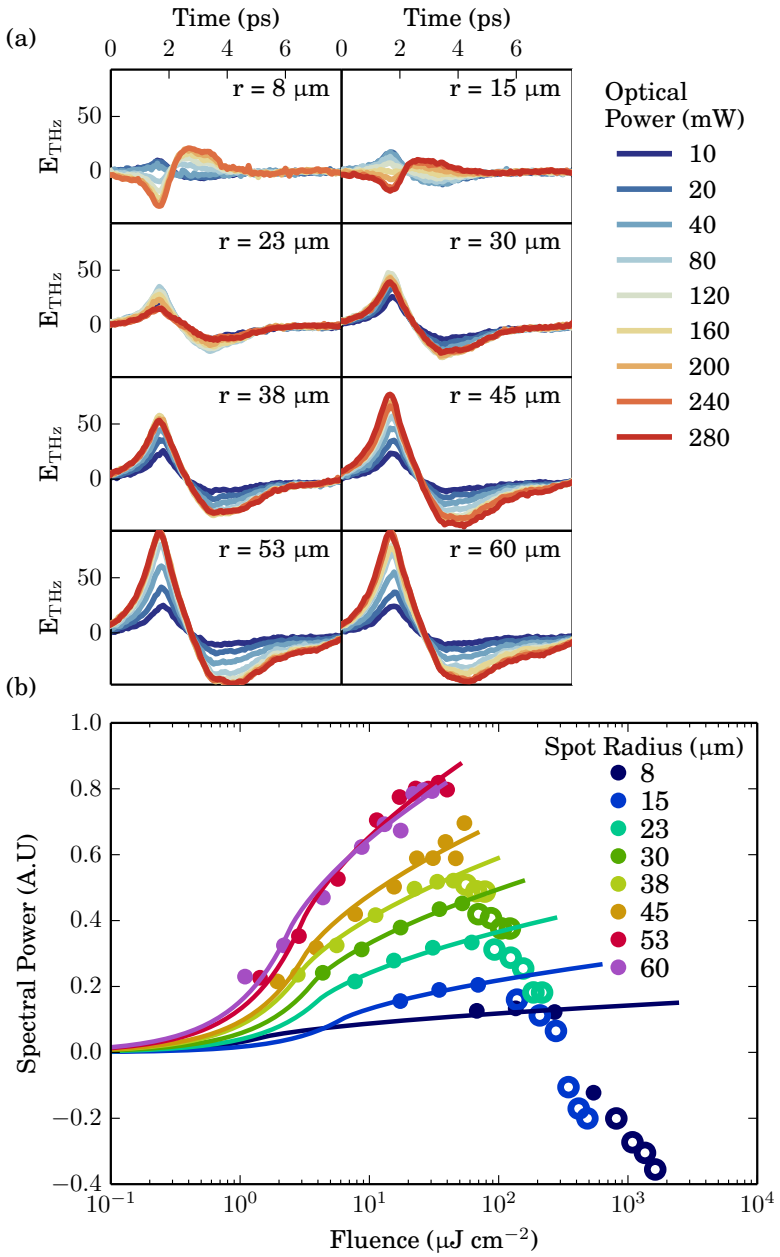

Figure 3.5: Semi-insulating GaAs THz-TDS variation with optical fluence. Figure (a) shows the time-domain scans grouped by optical spot radius with increasing power as plots of the detected electric field with time. Figure (b) shows the spectral intensity from each time domain scan plotted with optical fluence with Equation 4.2 plotted. Output power is less than half that of unannealed LT-GaAs as shown in figure 3.3. The fitting value for $\Phi_{sat} = 15.5 \pm 3.0\,\mu J\,cm^{-2}$. Above this fluence the terahertz output decreases and the polarity of the terahertz pulse inverts at $200\,mJ\,cm^{-2}$.

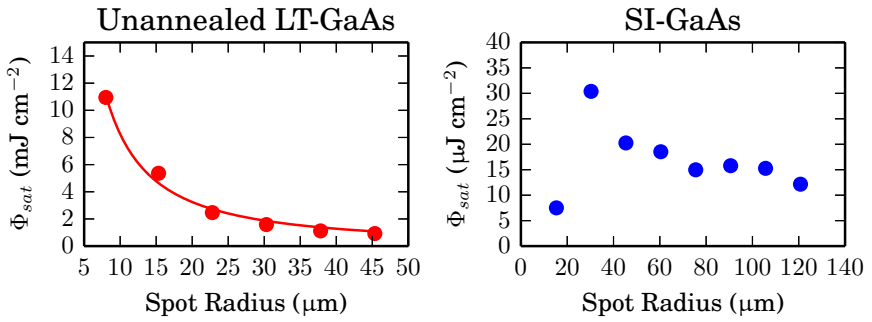

Figure 3.6: Values of Φ_{sat} used to fit fluence curves to (a) unannealed GaAs and (b) SI-GaAs from the data shown in figures 3.3 and 3.5. Lines fitted showing power relationship with spot radius of the form $f(x) \propto x^a$, where a is -1.346 for unannealed GaAs and -0.619 for SI-GaAs.

either annealed or unannealed LT-GaAs. The maximum spectral intensity is less than half that of unannealed LT-GaAs as shown in figure 3.3 as noted in table 3.2. SI-GaAs exhibits a well defined saturation curve with a point of inflection at $15.5 \pm 3.0\,\mu\text{J}\,\text{cm}^{-2}$. Beyond this fluence the output power of the emitter decreases and at fluences above $200\,\mu\text{J}\,\text{cm}^{-2}$ the polarity of the pulse inverts, as shown in figure 3.10(a). The decrease and inversion of the polarity is attributed to a competing terahertz emission mechanism that dominates the lateral photo-Dember effect in SI-GaAs samples at fluences greater than $3\,\text{mJ}\,\text{cm}^{-2}$. This competing effect causes fluence dependence above Φ_{sat}, as shown in figure 3.5, to decrease rapidly. Thus the value determined for Φ_{sat} is determined by the relative strength of the competing generation mechanism rather than intrinsic carrier saturation. The cause for this inversion is discussed in the next section.

All of the samples show variation in the value of Φ_{sat} with optical spot size used in fitting equation (4.2) as shown in figure 3.6. Figure 3.6 (a) and (b) shows the variation of the fitted values of Φ_{sat} with each value of r held constant. This is unexpected, as the model attempts to take into account the geometry of the LPD emitter as the optical spot size grows. The model assumes that the region of active terahertz generation occurs along a

Material	Optical Power p (mW)	Spot Radius r (µm)	Fluence ($\mu\text{J}\,\text{cm}^{-2}$)	Spectral intensity (A.U.)	Dynamic range (dB)
Unannealed LT-GaAs	240	23	186	1.69	20.1
Annealed LT-GaAs	240	23	186	1.42	22.6
SI-GaAs	240	23	186	0.182	18.8

Table 3.3: Table of results comparing the spectral intensities and dynamic range of LPD emitters with a constant fluence of $186\,\mu\text{J}\,\text{cm}^{-2}$. Results are used from the data plotted in figure 3.4 for annealed GaAs, figure 3.3 for unannealed GaAs and figures 3.5 and 3.8 for dynamic range.

one dimensional slice of the optical spot and that additional terahertz generation does not occur above a fluence of Φ_{sat}. If this is true, we expect the fitted value of Φ_{sat} to remain constant with spot size. The variation with spot size r implies that the saturation does not depend on the on-dimensional cross section, and instead on the total deposited area over the GaAs surface. If the data in figure 3.6 is fitted with a power function of the form $f(r) \propto r^a$, we find a is -1.35 for unannealed GaAs, while SI-GaAs shows little variation with r. In the geometry of the fitting a 1D section along the boundary is defined as the active component. The inverse relationship of Φ_{sat} for unannealed LT-GaAs may imply that instead of a saturation of fluence along the one dimension, the saturation occurs over two dimensions. If this is the case the saturation mechanism may be limited by the thermal load of the material in LT-GaAs. This works well with the observation that saturation occurs near the damage threshold. The power relationship with SI-GaAs shows a more stable fit, but still has a power dependence with r.

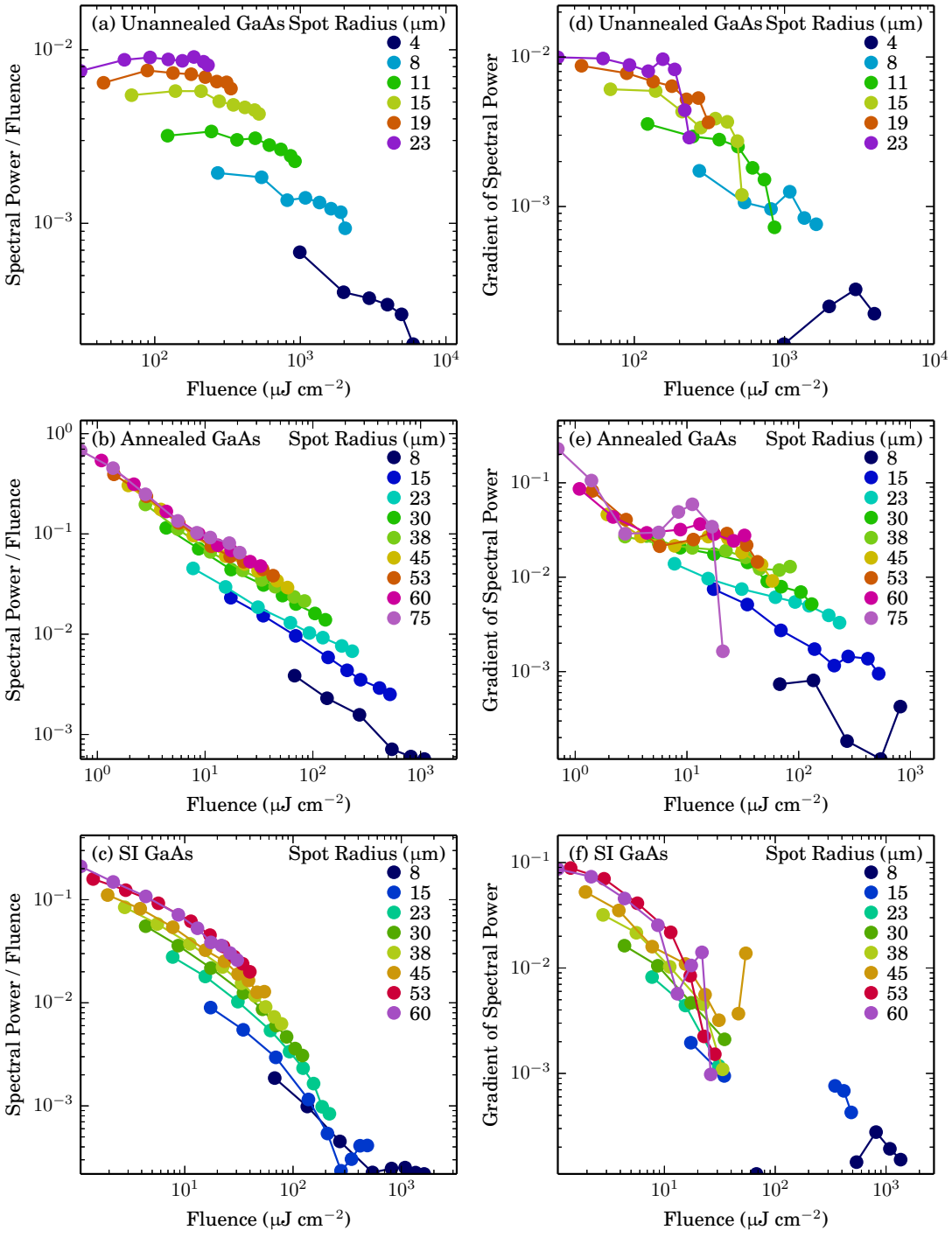

Figure 3.7: Figures showing the optical efficiency and the slope of fluence data used in figures 3.3 to 3.5. All figures are plotted with a logarithmic x and y axis. Figures (a), (b) and (c) show the relative efficiency of the LPD emitters, measured as the terahertz spectral intensity dived by the optical fluence. Figures (d), (e) and (f) show the first order derivative of the spectral intensity measurements. Figure (b) showing the high optical efficiency of annealed LT-GaAs at very low optical fluences of $\sim 1\,\mu J\,cm^{-2}$. Figure (e) shows the initial shoulder clearly at $7\,\mu J\,cm^{-2}$ of annealed LT-GaAs.

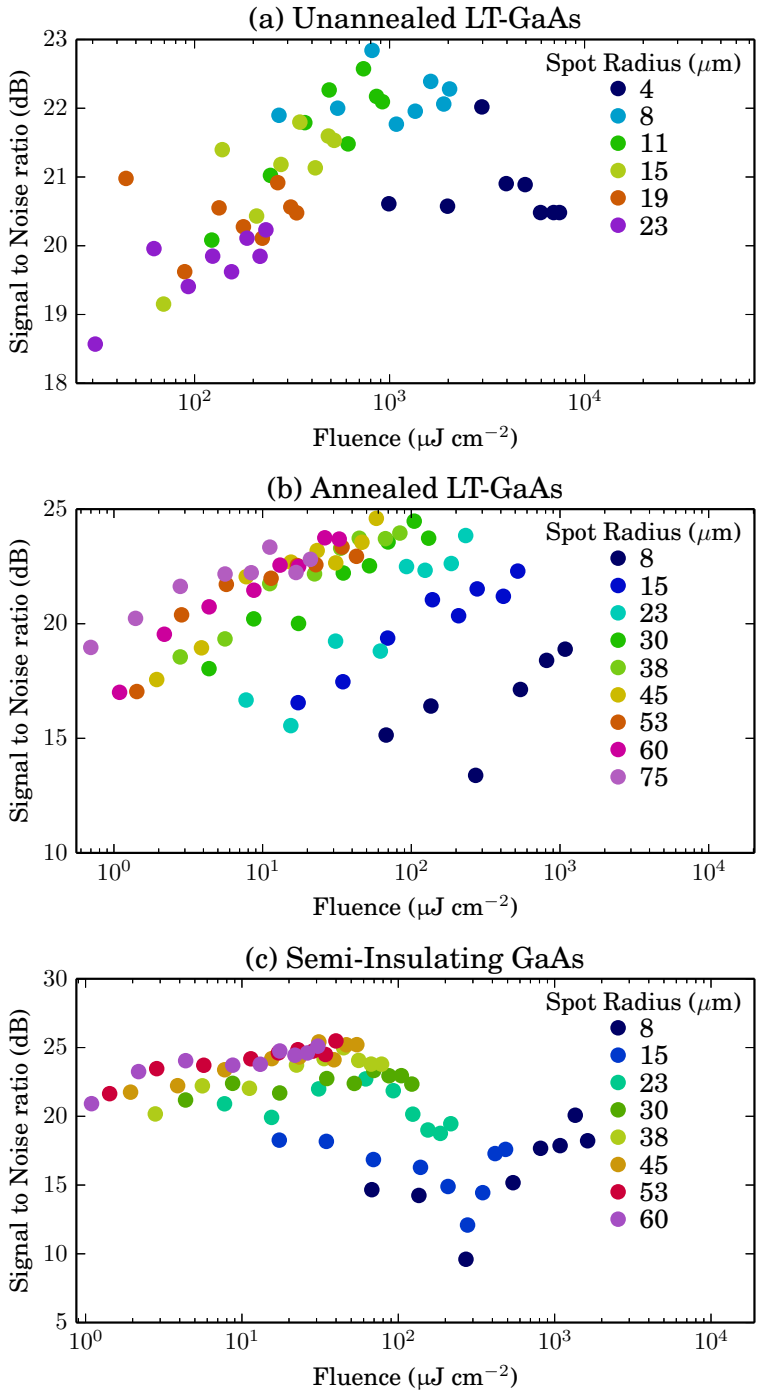

Figure 3.8: Figures showing the signal to noise ratio (SNR) of the data used for (a) unannealed LT-GaAs, (b) annealed LT-GaAs and (c) semi-insulating GaAs.

3.4 Polarity Dependence

The polarity inversion shown in figure 3.9 of the terahertz pulse with increasing fluence in SI-GaAs is unexpected. Figure 3.9 shows this inversion in the time domain of the terahertz pulse for two different spot sizes with increasing optical power. Figure 3.9 (a) shows the time-domain terahertz pulse with increasing power for a 75 µm radius optical spot size and figure 3.9 (b) shows the same for a 15 µm radius optical spot size. Figure 3.9 (a) shows the terahertz pulse increasing with optical power, and figure 3.9 (b) shows the pulse decrease and invert polarity at optical fluences greater than $1\,\mathrm{mJ\,cm^{-2}}$. Each of these time domain plots is taken as a subset of the fluence measurement presented in figure 3.5. The inversion occurs with increasing fluence, and the polarity inversion occurs at the same fluence independent of spot size. This effect is only observable on the boundary of the gold mask. Figure 3.10 shows time domains scans with the optical beam positioned on the gold boundary at 0 µm, and ± 20 µm from the boundary. Inversion is only seen on the boundary at 0 µm. The region that this effect occurs in is much more dependent of position than the lateral photo-Dember effect. We believe that the inversion is due to a competing terahertz generation mechanism that dominates over the lateral photo-Dember effect at high fluences in SI-GaAs.

We attempted to characterise this inversion with optical polarisation. The optical beam power was 140 mW with a beam diameter of 30 µm yielding a fluence of $240\,\mathrm{\mu J\,cm^{-2}}$. The observed terahertz pulse power is dependent on optical polarisation, as shown in figure 3.11. Research based on the polarisation dependency of photoconductive

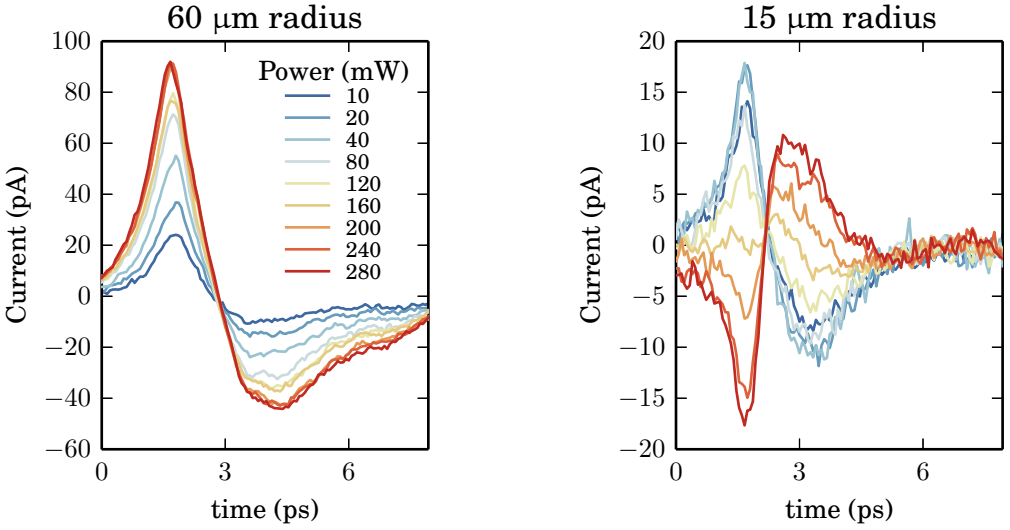

Figure 3.9: Time domain terahertz scan from the SI-GaAs LPD emitter. Figures (a) and (b) show the time domain data from figure 3.5 for 60 µm and 15 µm spot radii. The inversion in pulse in figure (b) occurs in fluences greater than $1\,\mathrm{mJ\,cm^{-2}}$.

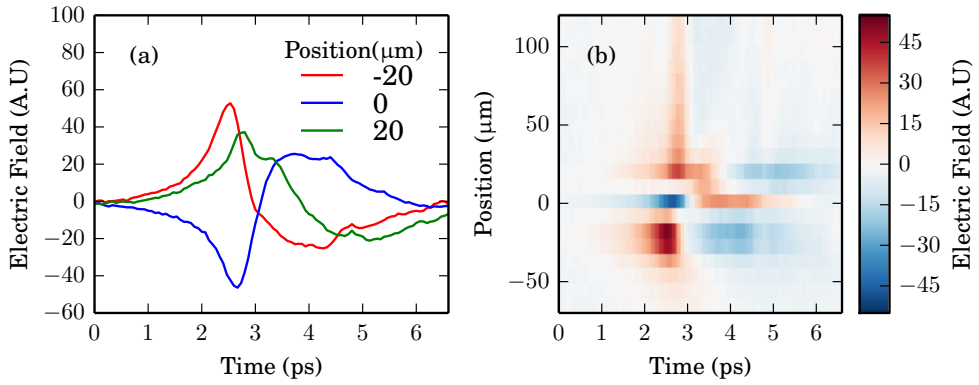

Figure 3.10: Time domain scans with lateral position on sample. Figure (a) shows time domains scans with the optical beam positioned on the gold boundary at 0 µm, and ± 20 µm from the boundary. Figure (b) combines a set of time domain scans with lateral position demonstrating the change in polarity on the gold boundary, positioned at 0 µm and 270 µm.

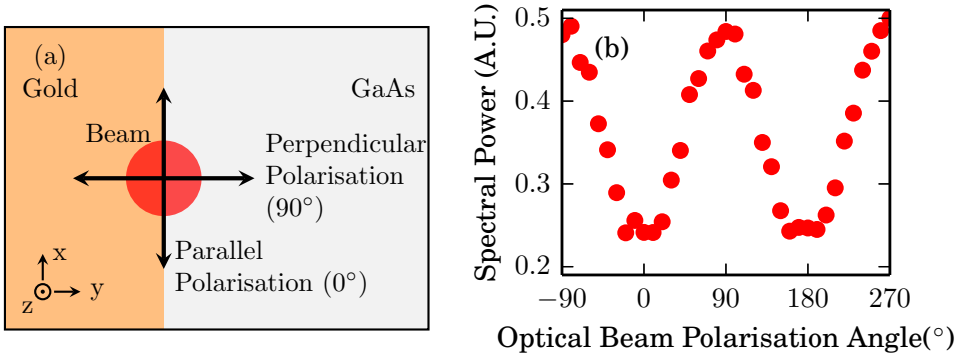

Figure 3.11: Terahertz output power from optical polarisation Figure (a) illustrates the polarisation orientation relative to the LPD emitter with arrows representing the polarisation of the optical beam. Figure (b) shows the variation in terahertz pulse power for a SI-GaAs LPD emitter at $237\,\mu J\,cm^{-2}$ optical fluence. Peak terahertz emission occurs with perpendicularly polarised light (0°). The increased emission at perpendicular polarisation is due to the increased carrier density in the depletion region near the metal mask.

antennas frequently refers to the polarisation of light as being "TE" or "TM" polarised relative to the photoconductive current. With the lateral photo-Dember emitters that distinction is lost, so we define the polarisation as either perpendicular or parallel to the emitter boundary as shown in figure 3.11 (a). The peak output power corresponds to perpendicular polarised light relative to the gold border on the semiconductor, as shown in figure 3.11 (b), regardless of the emitter rotation. Changing the polarisation alters the point at which the polarity of the signal inverts with fluence, the threshold was reduced to a minimum at perpendicular polarisation. We also rotated the lateral photo-Dember emitter by 90° to determine if the inversion depends on emitter orientation, though the same angular dependence was kept with the optical beam polarisation relative to the metal boundary.

Photoconductive antennas also demonstrate similar polarisation dependence to the observed inversion in the LPD emitters [82]. Perpendicular (90°) polarised light increases terahertz output power for photoconductive emitters compared with parallel (0°) polarised light. The variation in terahertz output power with optical polarisation is due to the optical near field diffraction pattern of the metal structure. Changes in the spatial optical intensity impact the performance of both LPD and photo-conductive antennas. If both the LPD emitters and photoconductive antennas are treated as semi-infinite metal planes, the near field diffraction pattern can be calculated. Close to a semi-infinite metal plane, diffraction creates an optical enhancement close to the plane boundary [83]. Figure 3.11 shows the impact of polarisation of diffraction on a large, thin metal sheet modelled in COMSOL. Parallel polarisation shows a smooth variation in optical intensity with a period comparable to the wavelength of the optical beam, while perpendicular polarisation shows a sharp sub-wavelength intense enhancement in the local optical intensity. The enhancement demonstrated in the COMSOL model matches the analytical calculation for near field diffraction of a semi-infinite sheet [83]. The large increase in local optical intensity aids the efficiency of both photo-conductive antennas where there is an enhanced electric field near the anode of the emitter [84]. The region of this anode enhancement occurs $\sim 200\,\text{nm}$ away from the metal boundary [85]. By creating an enhanced optical field near the anode more carriers are formed near the anode. Carriers that are created near the anode experience an enhanced electric field, create a higher rate of change of microscopic current $\partial\vec{j}/\partial t$, creating enhanced terahertz emission [84].

LPD emitters do not use an applied bias, and thus do not have an anode to enhance the electric field. However the dipole suppression that occurs within LPD emitters is improved by positioning carriers closer to the metal boundary. If more carriers are generated near the gold mask more carriers diffuse under the mask and contribute to the lateral photo-Dember emission, opposed to contributing to quadrupole emission away from the mask. The enhanced local optical field was simulated with COMSOL with the results showed in figure 3.12 for a plane optical 800 nm wave, partially masked by a gold sheet. In figure 3.12, an enhancement in the optical field is observable within the range of 200 nm for perpendicular polarisation, confirming Heitman et al.'s prediction. The model shown in figure 3.12 uses rounded features on the gold mask to demonstrate the local field enhancement as sharp geometry demonstrates a singularity-like enhancement of electrical field near the mask. Perpendicular polarisation also demonstrates a higher optical field under the gold mask that extends past the $\sim 200\,\text{nm}$ enhancement region, creating a larger quenched dipole for perpendicular polarisation compared to parallel polarisation.

While this effect accounts for an enhancement in the lateral photo-Dember effect it alone does not explain how the polarity of the time-domain signal inverts. For the inversion to take place a different effect competes with the dipole quenching mechanism, generating a terahertz pulse with the opposite phase. By patterning an insulating PI layer between

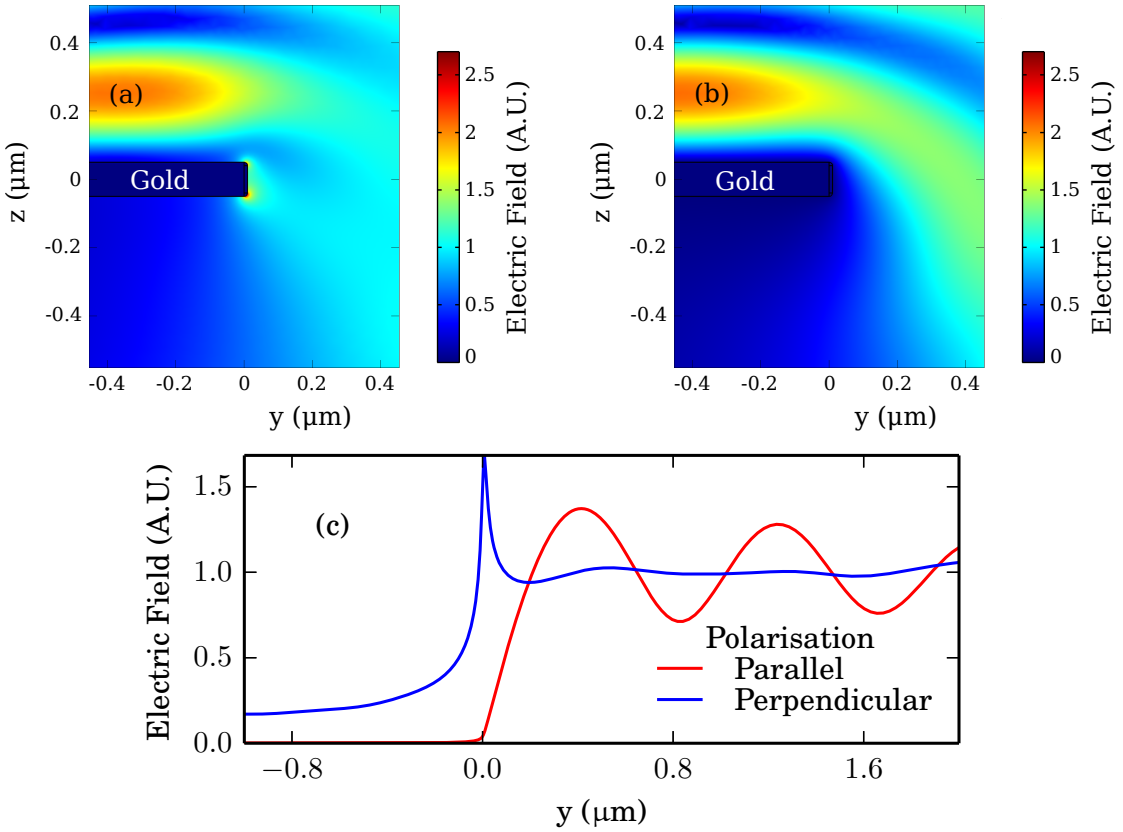

Figure 3.12: (a) and (b) show the impact of polarisation on the diffracted light intensity under a 100 nm thick gold sheet in air, modelled with COMSOL. The gold masks the region $y < 0$, leaving the region $y > 0$ unmasked. The perpendicularly polarised light creates a local enhancement near the sheet edge, shown in (a). (b) shows no local enhancement for parallel polarised light. (c) shows the comparison local enhancement underneath the gold mask along the y axis.

the Au layer and SI-GaAs the polarity change observed at high fluence does not occur, indicating that the inversion is due metal-semiconductor contact.

3.5 Emission due to Schottky Barrier

From the change in signal polarity observed in SI-GaAs at high fluences we can assume that there is another terahertz generation mechanism that competes with the diffusion current. The same effect has been observed in SI-GaAs in both surface-based emitters using Au as a metal interface [86–88]. Jin et al. observed a similar polarity change in terahertz pulses with optical fluence using SI-GaAs and gold as a photo-Dember emitter [86]. The SI-GaAs was covered by a thin <10 nm gold layer and placed at an oblique angle to the optical beam in the classic photo-Dember emitter geometry. At low optical power terahertz emission was observed with the same pulse polarity the LT-GaAs based

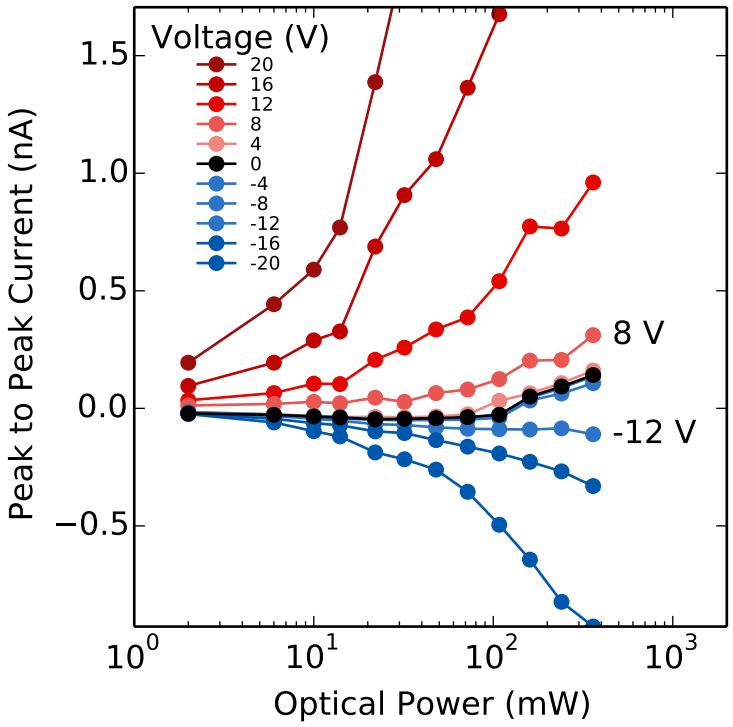

(a) Voltage and power measurements for SI-GaAs with perpendicular polarisation.

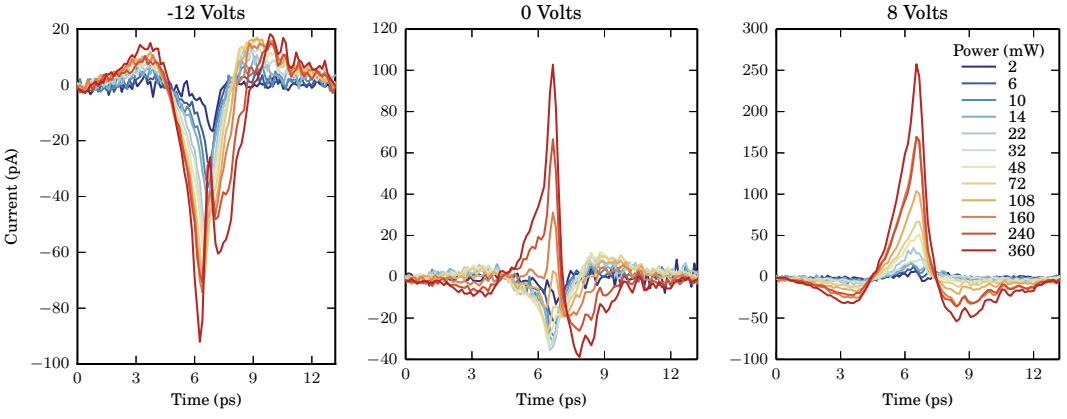

(b) (c) (d)

Figure 3.13: A set of plots showing terahertz emission from the lateral photo-Dember effect in the time domain with varying voltage and fluence. Figure (a) plots the peak to peak current in the time domain on a semi-log scale to show the change in polarity that occurs with fluence. The linear region is indicated by the grey area. The fluence at which the polarity of the pulse changes does not change with optical power or electric field. Note the peak formed in the time domain in figure (b) at $-12\,\mathrm{V}$ with increasing power. This peak indicates that the fluence dependent effect competes with the photoconductive effect.

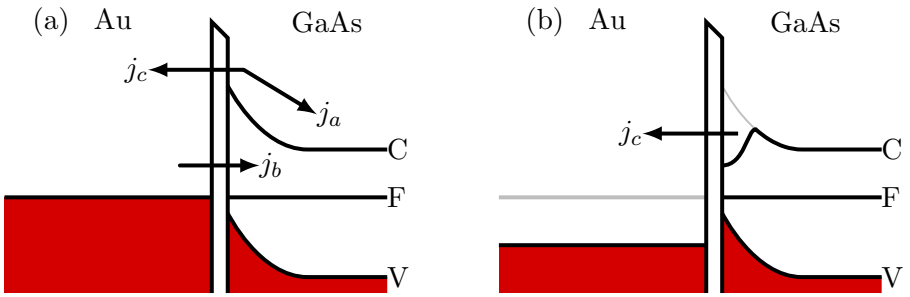

Figure 3.14: Illustration showing the change band structure at (a) low optical fluence and (b) high optical fluence for SI-GaAs covered with an Au layer. The gap between Au and GaAs represents the existence of a thin oxide layer present in metal-semiconductor contacts. The conduction (C), Fermi (F) and valence (V) band structures are altered by the presence of the oxide layer. Currents j_a, j_b and j_c are considered near the boundary. Figure (a) shows the band structure at low optical fluence, and (b) at high optical fluence. In figure (a), j_c is small and j_a and j_b dominate. In figure (b) at high optical fluence an accumulation layer of electrons is created from j_b creating a second region of band bending. j_c becomes larger and dominates over j_a and j_b, causing the observed inversion in terahertz polarity.

lateral photo-Dember emitters, whereas at high optical fluences greater than $10\,\mu\mathrm{J\,cm^{-2}}$ the polarity of the pulse inverts.

Further research on this observation was published by Li et al. who attributed the polarity change of the terahertz pulse to the Schottky field and Fresnel reflection within the semiconductor [87]. Li et al. hypothesised that the polarity of the detected terahertz signal from classic photo-Dember emitters depends on the direction of the electron diffusion. In a classic photo-Dember emitter the carrier current occurs parallel to the surface normal. Li et al. showed that if the current direction is changed by 90° the polarity of the detected terahertz signal inverts in the classic photo-Dember geometry. This rotation of current could either be caused by an applied bias, or an intrinsic bias such as a Schottky field from the metal interface within the photo-Dember emitters. While this explanation applies for classic photo-Dember emitters, it does not apply to lateral photo-Dember emitters. The polarity change described only affects the "pseudo-reflected" terahertz emission from the sample, rather than the terahertz emission transmitted through the substrate. With the LDP emitter geometry the detected terahertz emission passes through the substrate, so this explanation does not apply to the observed flip in polarity.

Shi et al. also analysed the polarity flip observed in SI-GaAs with increasing fluence in photo-Dember emitters, attributing the change in polarity to the Schottky field [88]. When a metal interface is applied to a semiconductor surface the band structure of the semiconductor changes at the surface [89]. The region over which the band bending takes place is referred to as the depletion region of the semiconductor. This band bending creates an intrinsic electric field at the surface, and is responsible for the terahertz

emission produced by Fermi level pinning. The polarity change in the terahertz signal is due to the reversal of the net current that is caused by the Schottky field. A net current reversal is caused by the accumulation of carriers in the depletion region, causing the change in signal polarity. Figure 3.14 shows a simplified band diagram in the depletion region of SI-GaAs with an Au layer, with C, V and F representing the conduction, valence and Fermi bands. The gap in the band diagram is shown to indicate the existence of surface states on the metal-semiconductor contact. When carriers are excited in the depletion region, they diffuse creating a microscopic current. We specify the current from three sources as j_a, j_b and j_c. j_a results from the Fermi level pinning of the GaAs surface, diffusing away from the metal surface. This is the same current that occurs in Fermi-pinning terahertz emitters. j_b results from free-carrier absorption of photo-excited carriers from the Au layer that flow into the GaAs substrate. Carriers from j_b accumulate in the depletion region and can flow back into the metal. j_c represents the current from electron tunnelling of carriers from the GaAs to Au from the accumulated carriers. At low fluences, shown in figure 3.14(a), j_b is small, leaving j_a and j_c providing a net current flowing from the Au layer to the GaAs substrate. As the fluence increases, shown in figure 3.14(b), carriers accumulate near the Au layer from current j_b. The accumulation layer creates an electric field near the Au layer, creating a second region of band bending. The accumulation region reduces the barrier height of the conduction and valence band, and the Fermi level within the Au layer is decreased due to the current to the GaAs. These effects enhance the electron tunnelling current j_c, allowing the current from the GaAs to gold to dominate the current from the surface field. The current j_c flows in the opposite direction to j_a and j_b, causing the change in signal polarity at high optical fluences. While this effect has been observed for classic photo-Dember emitters it is likely that the same effect is observed in the Si-GaAs LPD emitters, given the similarity on polarity shift with fluence. If true, this effect shows that a lateral component of the Schottky field plays a role on the metal boundary with the semiconductor. While this effect is observable for SI-GaAs LPD emitters, it was not observed for either annealed or unannealed LT-GaAs. The effect is likely not present in LT-GaAs due to the fast carrier recombination; the current reversal is not possible if carriers recombine rather than accumulate.

We fabricated single edge LPD emitters with an insulating polyimide (PI) layer on SI-GaAs and LT-GaAs LPD emitters to reduce the effect of the Schottky contact. Adding the PI layer removed the polarity inversion with increasing optical fluence. The PI layer was spin-coated on the semiconductor surface to a thickness of 1 µm, with gold evaporated over the PI layer. This formed an insulating layer between the semiconductor surface and the metal, removing the lateral Schottky field. Both SI-GaAs and LT-GaAs emitters continued to function as terahertz sources. Figure 3.15 shows the influence of the PI layer on unannealed LT-GaAs. With the Schottky barrier removed, the LPD emitters show reduced terahertz amplitude, indicating that the carrier diffusion from the lateral Schottky field aids the dipole diffusing away from the metal. With the PI layer inserted

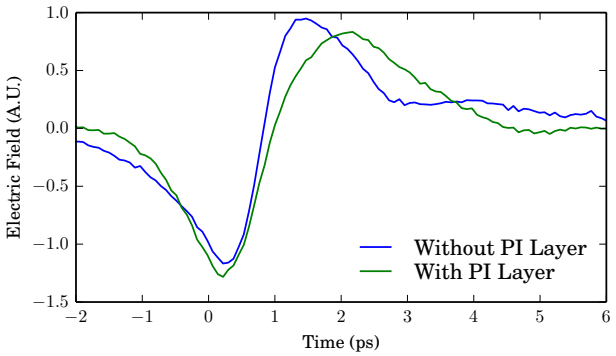

Figure 3.15: Terahertz time domain scan of a LT-GaAs LPD emitter with and without a insulating polyimide layer. Including the insulating layer results in a small decrease in the terahertz amplitude due to the reduced Schottky field. Th polarity of the field is determined by the effect of the electron tunnelling current, $\vec{j}_c$ as shown in figure 3.14

into the SI-GaAs single photo-Dember emitter, no observable change in polarity was detected regardless of optical fluence. This shows that the competing terahertz emission causing the inversion from SI-GaAs comes from the interaction between the metal and SI-GaAs surface.

We also tested this hypothesis by biasing the lateral photo-Dember emitter with an electric field. Instead the shape of the pulse does change, as shown in figure 3.13. Figure 3.13 shows terahertz emission from the lateral photo-Dember effect with varying voltage and fluence. Figure 3.13 (a) plots the peak to peak current in the time domain on a semi-log scale to show the change in polarity that occurs with fluence and figure 3.13 (b), (c) and (d) shows the time domain terahertz pulse. The fluence at which the polarity of the pulse changes does not change with optical power or electric field. Note the peak formed in the time domain in figure 3.13 (d) at $-12\,\mathrm{V}$ with increasing power. This peak is at the same direction to the unbiased photo-Dember emission at high fluence and does not appear to be affected by the applied bias. This peak indicates that the fluence-dependent effect competes with the photoconductive effect.

3.6 Conclusion

We have characterised terahertz performance from LPD emitters for unannealed and annealed LT-GaAs and SI-GaAs. Unannealed LT-GaAs demonstrated the highest saturation fluence and we conclude that for the best performance in LPD emitters annealing the substrate is not required and reduces performance, resulting in a simpler fabrication process for future emitters. However in unannealed LT-GaAs there is a change in carrier dynamics at high intensities, similar to that seen in annealed GaAs, that does not affect the terahertz pulse power. This process may be related to the same saturation mechanism in annealed LT-GaAs. Annealed LT-GaAs has shown complex

carrier dynamics owing to saturation of trap states, with the highest performance at low optical fluences. SI-GaAs exhibits a flip in signal polarity with increasing fluence that is attributed to a depletion later of carriers in the Schottky contact. All the tested LPD emitters show, as for photoconductive antennas, efficiency is increased for perpendicularly polarised light due to the increased carrier density near the gold edge due to a sub-wavelength local enhancement due to the metal barrier. The Schottky terahertz emission from the metal-semiconductor boundary competes with the LPD effect at high fluence due to current reversal. By fabricating an emitter with an insulating layer between the metal and semiconductor we can remove the change in signal polarity.

Chapter 4

Multiple Metal Lateral Photo-Dember Emitters

As we have seen in the previous chapters, the structure for a single LPD emitter is much simpler compared to a terahertz photoconductive antenna. This simplicity of construction opens up opportunities for efficient scaling over a large area by multiplexing (repeating) the number of emitters. Multiplexed photoconductive antennas have been demonstrated before [90, 91] and are available commercially [92]. The construction of these arrays of photo-conductive antennas require delicate fabrication processes, such as wire bonding for flip-chip fabrication, for attaching the electrodes. For the array of photoconductive antennas to work, the symmetry of the antenna must be changed. This is normally done by changing what parts of the antenna are illuminated, either by focussing on selected elements or by masking with an opaque layer [59]. We can use the lateral photo-Dember effect to achieve the same effect by repeating the lateral photo-Dember geometry.

As the single lateral photo-Dember emitter is a single gold edge scaling the emitter by creating a series of parallel gold strips (such as the example shown in figure 4.1) does not result in a net dipole. The dipoles on opposite sides of the emitters are equal in magnitude, as is the case of the classic photo-Dember effect, and no net lateral dipole is observed. To prevent this from happening we need to break the spatial symmetry of the repeated element, either structurally or modulating illumination intensity [1, 53]. In doing so a net lateral dipole component can be formed creating observable terahertz emission.

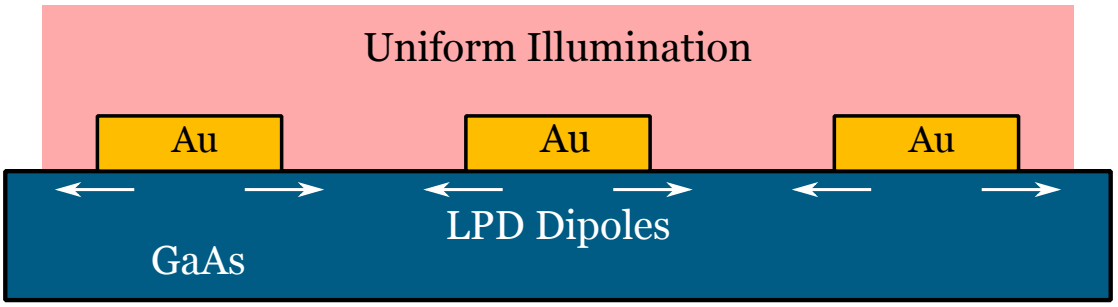

Figure 4.1: Diagram showing the set of net LPD dipoles from each edges for a set of strips. As each dipole on the strip is equal and opposite, not net terahertz emission occurs.

4.1 Variable Height Terahertz Emitters

Klatt et al. was first to demonstrate multiplexing LPD emitters, consisting of a series of wedges as shown in figure 4.2, into a powerful large scale emitter [53, 54]. While the multiplexed emitters did demonstrate comparable output power and bandwidth compared with photo-conductive antennas, the proposition for the mechanism that Klatt proposed for the mechanism was incorrect [3]. The varying thickness of the emitters created by Klatt et al. were created because it was thought that the metallic wedges would generate anisotropic carrier distributions [53]. The proposed explanation, illustrated in figure 4.3 was that thin regions of the metal lower than the skin depth would transmit light into the semiconductor. The optical intensity decreases exponentially with the metal thickness due to the skin depth effect and carrier density formed is proportional to the optical intensity. Klatt et al. proposed that regions that have a sharp contrast in carrier density, $\frac{\partial n}{\partial x}$, would create a larger current j. By dividing the emitter element into two regions they identified two regions of current density j on each side of the repeatable emitter shown in figure 4.3 as j. The wedged end of the emitter creates a smaller net current compared with the high density side, the thicker end of the emitter due to the higher contrast in carrier density $\frac{\partial n}{\partial x}$. Klatt et al. state that due to the non-symmetrical current distribution, a net current is formed due to diffusion with the net current responsible for terahertz emission.

However diffusion is an isotropic process; without a boundary condition such as a barrier the current due to intrinsic diffusion sums to zero. As a result both the lateral current on each side of the repeatable emitter is equal in magnitude. Although diffusion is an isotropic process that creates a zero net current, the anisotropy comes because only a part of the dipole population is quenched. The reflectivity of the metal in the terahertz region decreases with depth, and dipole quenching no longer occurs at the wedge of the repeatable emitter. As the thickness of the metal falls below the terahertz skin depth (90 nm at room temperature [93]), quenching is no longer present. With the lack of dipole quenching on one side of the repeatable emitter the dipole formed by the thicker end of the metal wedge is free to radiate in the same direction. Using this knowledge of the

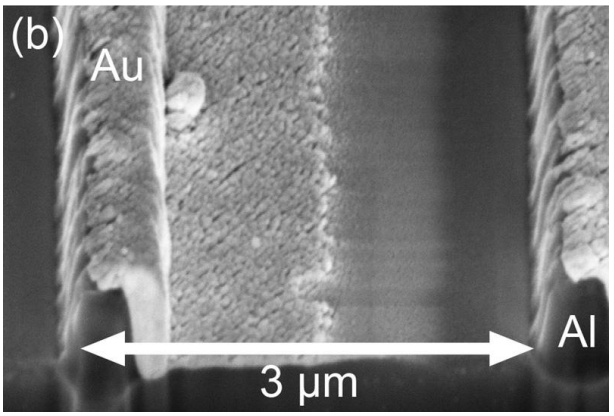

Figure 4.2: A SEM image showing the multiplexed LPD emitters as fabricated by Klatt et al. Thin walls of aluminium (Al) are deposited on the GaAs surface, and gold (Au) is evaporated at an angle to create a set of thin wedges. The wedges formed by the gold layer do not vary linearly in thickness, and show signs of percolation. Image used from [54].

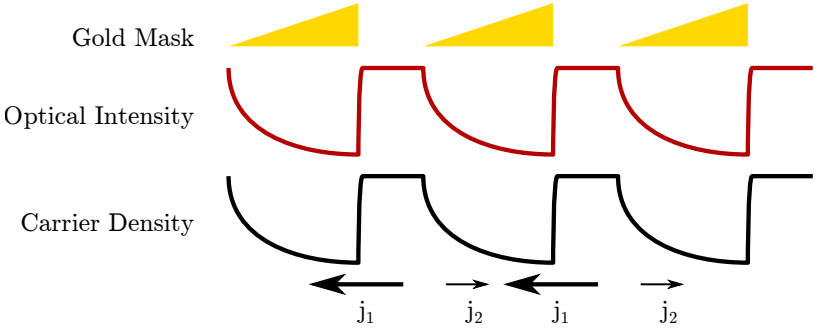

Figure 4.3: Illustrations of the multiplexed photo-Dember mechanism from Klatt et al.'s hypothesis. The gold wedge geometry allows the optical beam to partially transmitted to create an asymmetrical optical intensity, creating an asymmetrical carrier density. The carriers diffuse to create current densities j_1 and j_2. Klatt et al. proposed that $j_1 > j_2$, creating a net current. However the net current is zero and creates no net dipole to radiate terahertz emission.

difference of reflectivity we are able to fabricate emitters based on the same principle with a much simpler photo-lithography fabrication method, eliminating the need for the high-aspect ratio walls and angled evaporation.

4.2 Cylindrical Lens LPD Emitters

To create repeatable LDP emitters the lateral symmetry of the dipoles in the emitter needs to be broken either with by optical intensity or quenching strength. Paul Gow from our group first demonstrated this by changing the optical intensity using an array of cylindrical lenses shown in figure 4.4. If each lens focusses light onto a single edge, and array of LPD emitters is created as there is no opposing dipole such as the case illustrated in figure figure 4.1. The array of LPD emitters is created by patterning a

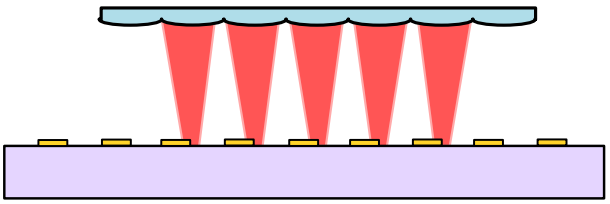

Figure 4.4: Diagram of a cylindrical micro-lens focussing on alternating edges of gold strips to create an array of LPD emitters.

series of gold strips on the semiconductor surface. An array of cylindrical lenses is chosen with the same pitch spacing as the metal strip pitch. The cylindrical lenses create a spatially symmetrical distribution of intensity over every other metal boundary element, as shown in figure 4.4. This has the effect of creating an array of single LPD emitters, with the strength of the terahertz emitters proportional to the emitters illuminated and the contrast ratio on each side of the emitter.

COMSOL was used to simulate the electric field of the terahertz emission from a repeated array of LPD emitters using the 1D diffusion model described previously in chapter 2 using the material properties of LT-GaAs [66, 94, 95]. Such a model geometry is the same case for multiple LPD emitters created by an array of cylindrical lenses. To represent the current generated from multiple LPD emitters the initial spatial carrier density was defined as a repeating array of half-Gaussian functions. Each half-Gaussian distribution represents the carrier distribution from the focus of the cylindrical lens, with a repetition period of 200 µm. The generation term $G(t)$ was defined as the pulse width of the 100 fs Ti:Sapphire laser. The simulation outputs the time-dependent current density which was incorporated into a COMSOL model. The COMSOL model contained periodic metal strips with the same positioning as the initial carrier density. The COMSOL model used the calculated current from the model to simulate the resulting terahertz pulse's interaction with the LPD metal mask, with the results shown in figure 4.5. Every repeated dipole emits a terahertz pulse parallel to the surface normal, as in the single LPD effect. Superposition occurs with neighbouring wave-fronts with each individual wave-front as they progress through the semiconductor. After emerging from the semiconductor the wave-fronts construct one single plane wave that retains coherence.

We created multiple LPD emitters using cylindrical arrays to characterize their performance with optical fluence in comparison to single edge LPD emitters. Two multiple emitter arrays were fabricated by evaporating 100 nm thick strips of gold with a 5 nm adhesion layer of chrome onto the surface of GaAs. One array was comprised of 200 µm period gold strips on SI-GaAs and the other of 15 µm period on LT-GaAs, each paired with a cylindrical lens array of corresponding pitch. A single LPD emitter was also

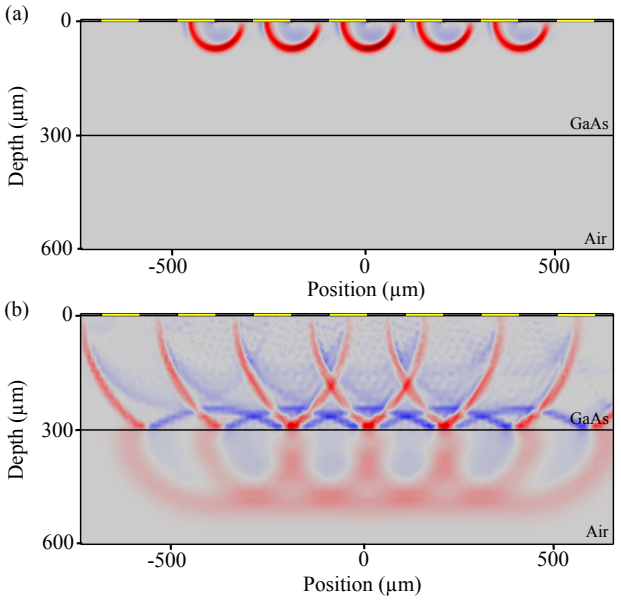

Figure 4.5: COMSOL model of the time-dependent electric field produced by the multiple LPD emitters shown in figure 4.4. Red and blue colours represent positive and negative values in the z component of the electric field at (a) 1.4 ps and (b) 4.85 ps after initial dipole emission.

fabricated as gold on LT-GaAs for comparison with the emitter arrays. A silicon hyper-hemisphere lens was used to focus the terahertz emission from the single LPD emitter. A focussing terahertz lens was not required for the emitter array due to the increased directionality from the large scale array. Each emitter was tested in the THz-TDS set up with a Menlo systems PC LT-GaAs detector, as described in section 1.3. A 100 fs, 80 MHz Ti:Sapphire laser centred at 800 nm, and with a $1/e^2$ beam size of 0.61 mm, was focussed onto the emitter surface with a cylindrical micro-lens array and modulated for lock-in detection. The optical power on the emitters was varied from 10–150 mW with the terahertz output recorded as the peak-to-peak amplitude of the time-resolved terahertz pulse. The multiple foci produced by the lens array were aligned against corresponding gold edges on the emitter by imaging the back-reflection from the surface. We illuminated 7 and 82 strips for the 200 µm and 15 µm period arrays respectively. The number of gold strips illuminated on each array were estimated by calculating the number of focusses produced by each micro-lens array that fell within the $1/e^2$ spot radius. Optical fluence was found by estimating the area of illumination for each focus and the percentage of total power focussed into each area.

By varying the power and spot size of the optical beam we attempted to determine the optical saturation fluence of the LPD emitter array. The saturation fluence was determined by fitting a simple saturation function of the form

$$E_{\mathrm{THz}}(F) = AcF/(F + F_{\mathrm{sat}}), \tag{4.1}$$

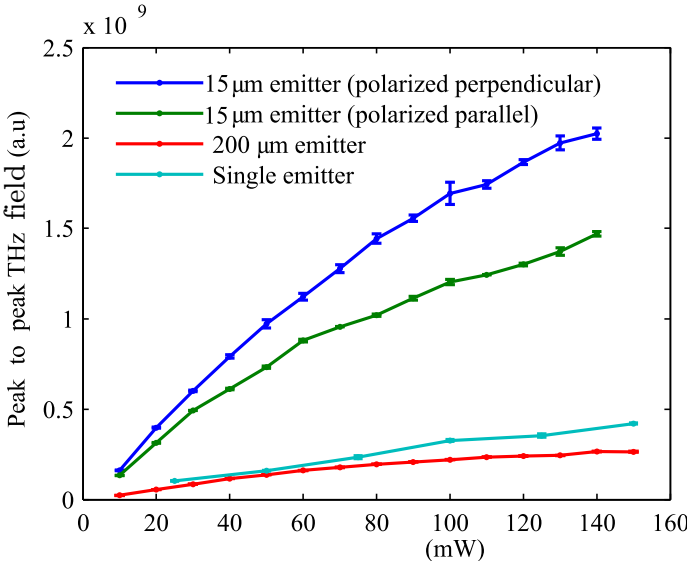

Figure 4.6: Graph of peak-to-peak terahertz electric field as a function of optical power for a single LPD LT-GaAs emitter, SI-GaAs and LT-GaAs array emitters. The 15 µm period multiple emitter was illuminated with light polarised both perpendicular and parallel to the gold edges.

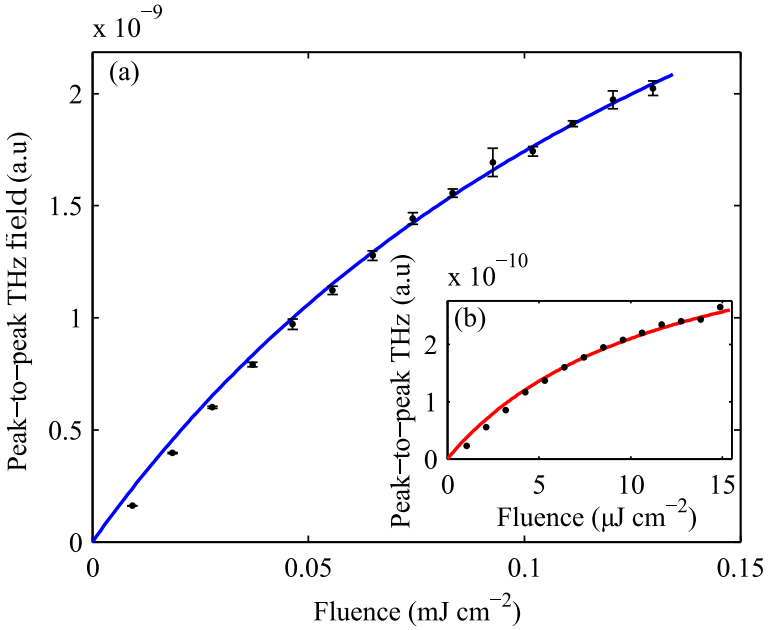

Figure 4.7: (a) Peak to peak amplitude of the detected terahertz field for the 15 µm period LT-GaAs multiple emitters plotted as a function of fluence. (b) shows the same but for the 200 µm period SI-GaAs emitters. The solid lines represent saturation curve fits.

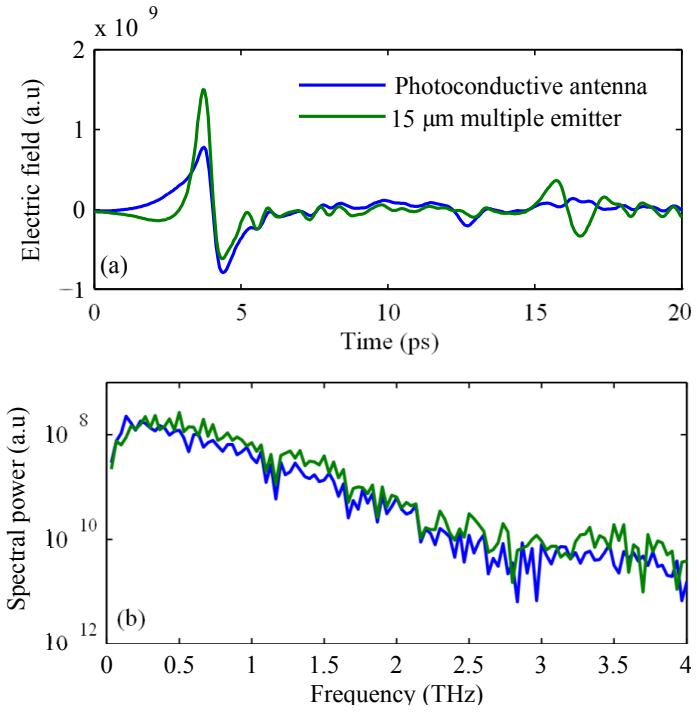

Figure 4.8: Comparison of (a), power, and (b), bandwidth, between the 15 µm period multiple emitter and a Menlo systems PC antenna. The Menlo systems antenna was biased at 5 V with both detector and emitter optical power at 5 mW. The 15 µm period multiple emitter was illuminated with optical power of 100 mW.

where A is a coefficient of conversion and alignment efficiency, c is the $1/e^2$ spot radius and F_{sat} is the saturation fluence. A simpler function is used in comparison to the fitting in chapter 3 as the geometry of the LPD emitter is not taken into account.

Results of the terahertz output with optical power are shown in figure 4.6. The 15 µm period LT-GaAs emitter exhibits an increase in peak-to-peak power of emitted terahertz radiation in comparison with a single LPD emitter and the SI-GaAs 200 µm array. By fitting equation 4.1 the average saturation fluence for LT-GaAs was found to be $F_{\text{sat}} = 0.18\,\text{mJ}\,\text{cm}^{-2}$, and for SI-GaAs $F_{\text{sat}} = 12\,\mu\text{J}\,\text{cm}^{-2}$. These values are consistent with the work carried out previously by Barnes et al. for single LPD emitters [2]. We compared the terahertz output of the 15 µm emitter with a commercial photo-conductive antenna, with scans shown in figure 4.8. Time domain scans were taken with the photo-conductive emitter biased at 5 V and both detector and emitter optical powers at 5 mW. The multiple emitter shows comparable bandwidth to the photo-conductive antenna, spanning 3 THz. However, a direct power comparison between the two emitters cannot be made due to the freedom in choice of the applied bias in the PC antennas. If the maximum voltage is chosen then the PC antenna would be more powerful, but this would considerably decrease its lifetime. Of the set of the emitters tested the 15 µm period LT-GaAs emitter provides the greatest terahertz output. The single LT-GaAs LPD emitter shows greater terahertz emission compared with the 200 µm period emitter. The

relative decreased terahertz emission compared with a single edge LPD emitter is likely a result the 200 µm period array being fabricated on SI-GaAs. SI GaAs shows lower output power in comparison to LT-GaAs due to significantly lower saturation fluence, as explained in chapter 3 [1]. This decreased saturation fluence is due to the competing current due to the current reversing due to the Schottky barrier. The presence of the silicon lens for focussing the terahertz emission produced by the single LPD emitter also makes direct comparisons between the two emitters difficult. Incident light polarised perpendicular to the gold edges shows a significant increase in emitted terahertz power when compared with parallel polarisation, as is consistent with the previously described plasmonic enhancement [82, 96]. The 15 µm period LT-GaAs array emitter produces 5.2 times as much output power as a single LT-GaAs edge, shown in figure 4.6, despite the presence of the silicon lens allowing a larger acceptance angle for the single emitter. Figure 4.7 shows the terahertz output plotted as a function of optical fluence for the 15 µm period multiple emitters with the inset showing the same for the 200 µm period emitters.

4.3 Multiple Metal LPD Emitters

As explained at the start of this section, and in the introduction, diffusion currents cannot be the sole mechanism for terahertz emission in the wedged emitters created by Klatt et al. We have refined the hypothesis of Klatt et al. [53] by attributing the mechanism of radiation of LPD emitters to diffusion currents and dipole quenching with a metal mask [2, 3]. The carriers that diffuse under the metal mask cannot radiate due to the proximity to the metallic surface. One lateral dipole exists within the sub-wavelength region under the semiconductor, and is fully quenched for a perfect metal. The rest of the carriers that diffuse away from the metal are free to radiate, unquenched by the semiconductor-air surface. In chapter 3 we have seen the influence of the lateral Schottky barrier on terahertz emission within LPD emitters. For this section we demonstrate

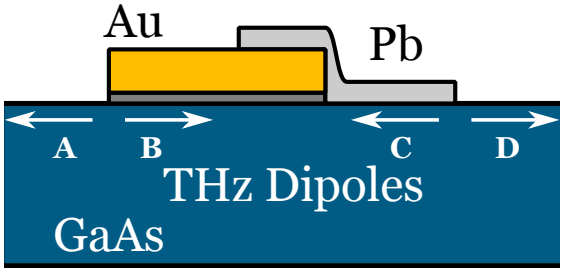

Figure 4.9: A diagram showing the emission mechanism of multiple-metal emitters due to the lateral photo-Dember effect. Carrier diffusion creates radiative dipoles near the metal boundaries, shown as arrows. Each set of dipoles created on the boundary are labelled A, B, C and D. The difference in the reflectivity between the two metals that quench dipoles B and C causes net terahertz emission to be observed.

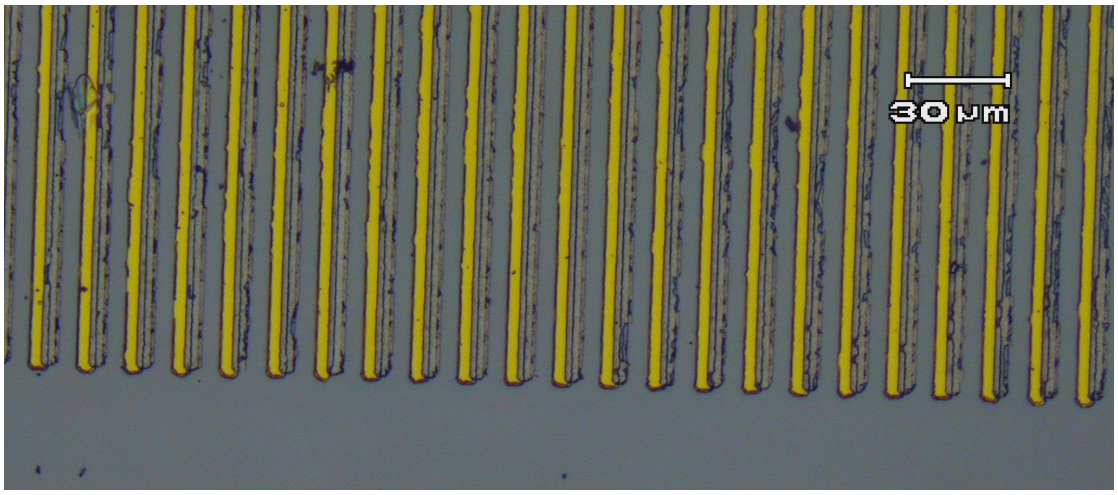

Figure 4.10: An optical microscope image of the multiple metal LPD emitters, fabricated with lead (Pb) and gold (Au).

repeatable photo-Dember emitters using two different metals, where both the difference in quenching strength and the lateral Schottky field are used to create observable terahertz emission.

We achieve the required asymmetry for a repeatable LPD emitter by applying a low skin depth second metal on one side of each repeat of the metal mask, as shown in figures 4.9 and 4.10. The lower skin depth metal reduces the quenching strength from one side of the metal mask by reducing the reflectivity of the metal surface [55]. Using multiple metals eliminates the requirement for a micro-lens array used previously [8], allowing for the emitters to operate under uniform illumination. The reduced quenching strength allows net terahertz emission to be formed in a dipole pattern under the low skin depth metal. In the ideal case the low skin depth metal is opaque to the optical pump beam and is transmissive to terahertz emission so quenching is reduced to a minimum. An opaque dielectric may be used in place of an additional metal at the expense of increased difficulty in emitter fabrication. This geometry is shown in figure 4.9 where gold completely quenches the dipole formed underneath whereas lead is deposited with a thickness below its skin depth (238 nm at 1 THz [97]) for terahertz frequencies and therefore not inhibiting the terahertz dipole to radiate. The dipoles are shown in figure 4.9 and are labelled A, B, C and D. Dipoles A and D oppose each other and only produce quadrupole emission. Dipole B is fully quenched by the gold mask. Dipole C is not fully quenched as the Pb layer has less reflectivity in the terahertz region. Under uniform illumination terahertz emission is observable co-linear with the surface normal due to the difference in quenching strength from the two metals.

We tested the transparency of Pb by evaporating Pb on microscope slides and testing the transmission in the THz-TDS. Pb layers with thickness below 24 nm are transparent at 1 THz [98]. We verified with THz-TDS that layers of Pb up to 80 nm were trasnparent

to the terahertz pulse across the spectral range of 2 THz while blocking light from the 800 nm optical pump beam.

Because we wanted Pb to be opaque to the 800 nm pump laser we chose for the fabrication to deposit a thickness of 100 nm. We designed a set of masks to deposit metal for standard photo-lithography and thermal evaporation. The Au layer deposition was performed first with a thickness of 170 nm and a 3 nm chrome (Cr) adhesion layer on both SI-GaAs and LT-GaAs. The mask for the Pb used the same strip pattern, and was optically aligned with the deposited Au pattern to ensure an overlap in the strip pattern. Figure 4.10 shows an optical microscope image of the multiple metal emitters. Each metal strip was 4 µm wide with a 15 µm period and a 2 µm overlap between the Au and Pb, as shown in figure 4.12. We also created emitters with an insulating SiO_2 layer to eliminate band bending from the metal [99] to characterize the relative strength of the LPD and Schottky effects. A Menlo Tera-8 photo-conductive antenna was used as a receiver with a focusing silicon lens. The double-metal emitters were mounted without any focusing silicon lenses. The emitters were illuminated with the pump laser with as beam diameter of 1 mm, illuminating 67 emitters. This spot size allows the emitter to act as a planar wave rather than a point source emitter for lens-free operation. An objective lens and a neutral density filter allowed the intensity and spot size to be adjusted, allowing the optical fluence on the multiple double-metal emitters to be varied. The multiple double-metal emitters were tested in a standard THz-TDS experiment using a Ti:Sapphire pump laser; centre wavelength 800 nm, 80 MHz repetition rate with a 70 fs pulse length.

From the observations shown on SI-GaAs in chapter 3, the lateral component of the Schottky barrier also plays a role in terahertz emission. Band bending near the surface of semiconductors can cause terahertz emission [49] and has been shown to influence LPD emitters [1] and to modify the polarity of terahertz pulses under intense optical fluence [1, 88]. Therefore in the repeatable structures the metal pairs also create terahertz emission due to different Schottky barrier potentials as a result of the different work functions of metals. By selecting metals with different skin depths and work functions both the LPD effect and Schottky barriers can contribute to terahertz emission. The concept is shown in figure 4.11 where by depositing metals with different work functions, ϕ_m, we create different barrier heights on each side of the double-metal emitters. The band bending causes a transient lateral current to form near the metal boundary emitting terahertz emission. If the barrier heights ϕ_b are different, net lateral current will occur proportional to the difference in barrier height under uniform illumination. If the barrier heights are equal, as the case would be for a single metal, no net current would be present under uniform illumination. Due to Bardeen surface states the barrier height is mostly independent of the work function of the metal but is dependant on surface quality due to oxidizing layers formed on the semiconductor surface [50]. The barrier height, ϕ_b of gold bonded with GaAs is approximately 0.9 eV [100, 101], and lead is 0.8 eV at 300 K

[102]. This potential difference can create a net lateral carrier current that contributes to the terahertz emission.

If the barrier heights are not equal the relative strength of dipoles A and D in figure 4.9 differ, producing net terahertz emission co-linear with the surface. In the multiple LPD emitters that we present the requirement for any focusing lens for the optical pump is removed, allowing the emitters to act as a drop-in replacement for photo-conductive emitters. These emitters are simple to fabricate, do not require an electrical bias or a silicon lens to out-couple the terahertz emission. We expect that these emitters are more durable than conventional photo-conductive emitters due to no risk of electrical breakdown from an applied bias.

Our initial results showed that multiple LPD emitters only functioned on SI-GaAs substrates; LT-GaAs substrates produced minimal terahertz emission. In comparison to our single edge LPD emitters the Schottky barrier plays a much greater role in generation of terahertz radiation. Figure 4.13 demonstrates the difference with and without an insulating SiO_2 layer for the SI-GaAs Au/Pb emitter which eliminates the Schottky barrier effect. The time domain scans and the corresponding power spectrum for the

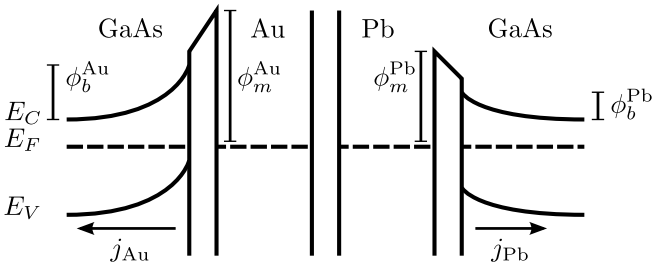

Figure 4.11: A band diagram of the repeatable terahertz emitters. Both gold and lead create a Schottky barrier near the interface. Two metals have different work functions, ϕ_m, creating different barrier heights ϕ_b. Band bending occurs near the metals creating currents j_{Au} and j_{Pb}. If $j_{Au} \neq j_{Pb}$ terahertz emission due to a net current is generated.

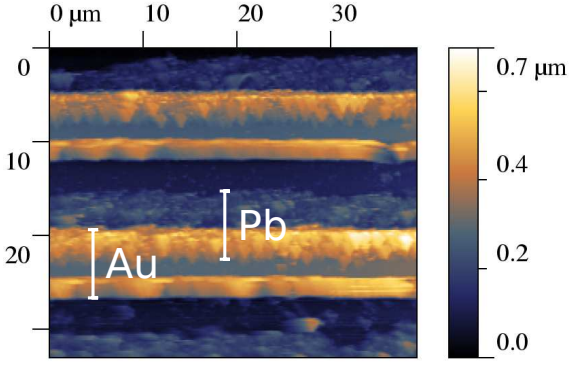

Figure 4.12: An atomic force microscope image of the repeatable emitters fabricated with gold and lead. The lead layer has oxidized with the air, forming a rough surface.

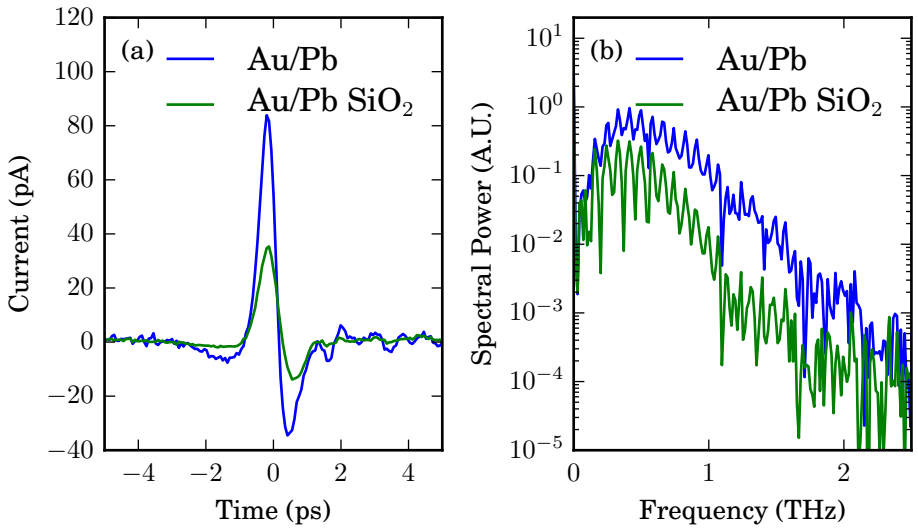

Figure 4.13: THz-TDS scans for Au/Pb emitters patterned on SI-GaAs in (a) the time domain and (b) the frequency domain. The emitters are patterned on bare SI-GaAs substrate and with an insulating SiO_2 layer to eliminate the Schottky effect. Adding the SiO_2 layer reduces the output power by more than half, showing the influence of the Schottky barrier to play a greater role than observed in the single edge LPD emitters.

Au/Pb insulated with SiO_2 and Au/Pb uninsulated are shown in figure 4.13 for optical pump power of 180 mW and spot diameter of 1 mm at room temperature. The addition of the SiO_2 layer more than halves the peak-to-peak detected terahertz current. The increased output amplitude resulting from eliminating the insulating layer is due to the different work functions of the two metals, leading to a difference in the barrier heights ϕ_b.

We characterized the Au/Pb emitters with fluence to test for saturation effects shown in figure 4.14. We used a saturation fit of the form

$$E(F) = A\frac{F}{F + F_{\text{sat}}} + c, \tag{4.2}$$

where F is the optical fluence, F_{sat} is the optical saturation fluence and A is a coefficient that describes efficiency. c is used as an offset for the fitting where the optical fluence is zero. When the optical fluence is zero, noise will still be recorded and be recorded as a peak-to-peak amplitude. F_{sat} was determined to be $0.82\,\mu\text{J}\,\text{cm}^{-2}$ for metal directly fabricated on SI-GaAs, whereas no saturation was observed for double-metal structures fabricated with an insulating layer. The cause of saturation within the directly bonded double-metal emitters is likely to be due to the charge accumulation within the depletion region as observed in the case of SI-GaAs single LPD emitters. The drift current of the electrons from the metal to the semiconductor is reduced for higher fluences, at high

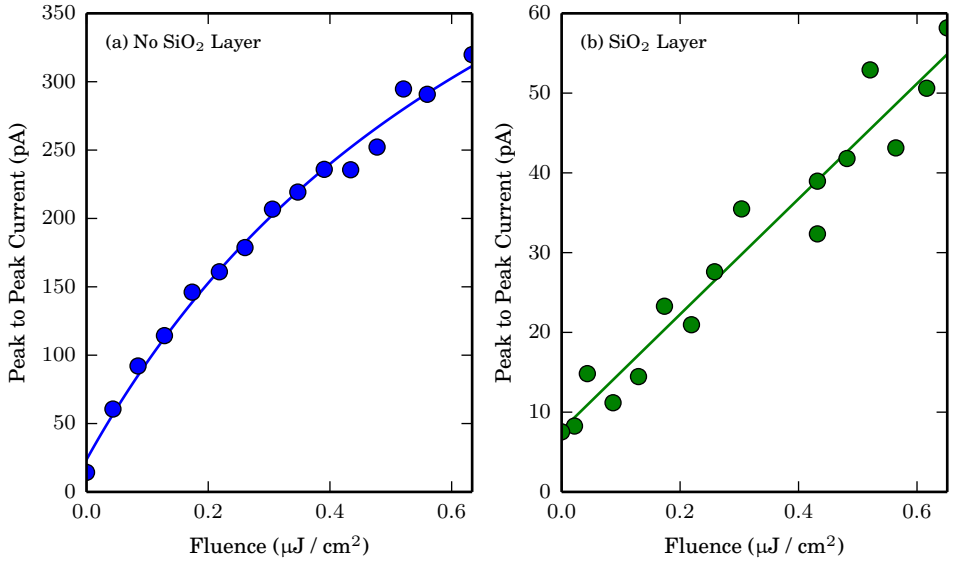

Figure 4.14: (a) shows the fluence dependence of Au/Pb without an SiO_2 layer and (b) with an insulating SiO_2 layer. The optical spot radius is held at 430 µm. The saturation fluence, F_{sat}, (a) is fitted from equation 4.2 and determined to be $0.82\,\mu J\,cm^{-2}$, (b) shows no saturation.

carrier concentrations the barrier height decreases due to the higher carrier density and higher Fermi energy in the semiconductor [1, 88]. The results show that the emitters with the highest peak to peak amplitude are Au/Pb fabricated directly of SI-GaAs. The Au/Pb insulated emitters produce less terahertz emission as they utilize only on the difference of quenching efficiency of Au and Pb strips.

Multiple double-metal emitters have similar signal to noise performance compared with large gap SI-GaAs photoconductive antennas measured in a terahertz time-domain spectroscopy (THz-TDS) experiment. The double-metal emitters produce emission of 2 THz bandwidth with 33 dB of dynamic range as shown in figure 4.13 similar to a SI-GaAs large gap photoconductive emitter biased at 20 V with a 140 µm electrode gap. Figure 4.15 shows the multiple metal emitters share same dependence with optical polarisation as the single edge LPD emitters in chapter 3, showing enhanced terahertz amplitude for "perpendicular" polarisation.

We measured terahertz emission power with temperature for both Au/Pb SiO_2 and non-SiO_2 fabricated emitters. Both emitters were mounted in a helium flow cryostat that allowed a temperature range of 4–300 K and illuminated with an optical power of 200 mW. Figure 4.16 (a) and (b) show the peak-to-peak terahertz signal with temperature for the non-SiO_2 and SiO_2 double-metal emitters respectively. The alignment of the emitters changed with the mounting in the cryostat, so the relative detected terahertz emission viewed in figure 4.16 (a) and (b) is not strictly comparable. The terahertz output power increases with decreasing temperature for the insulated SiO_2 emitter, with an optimum emission temperature at 50–75 K, shown in figure 4.16 (b). This increase in output power

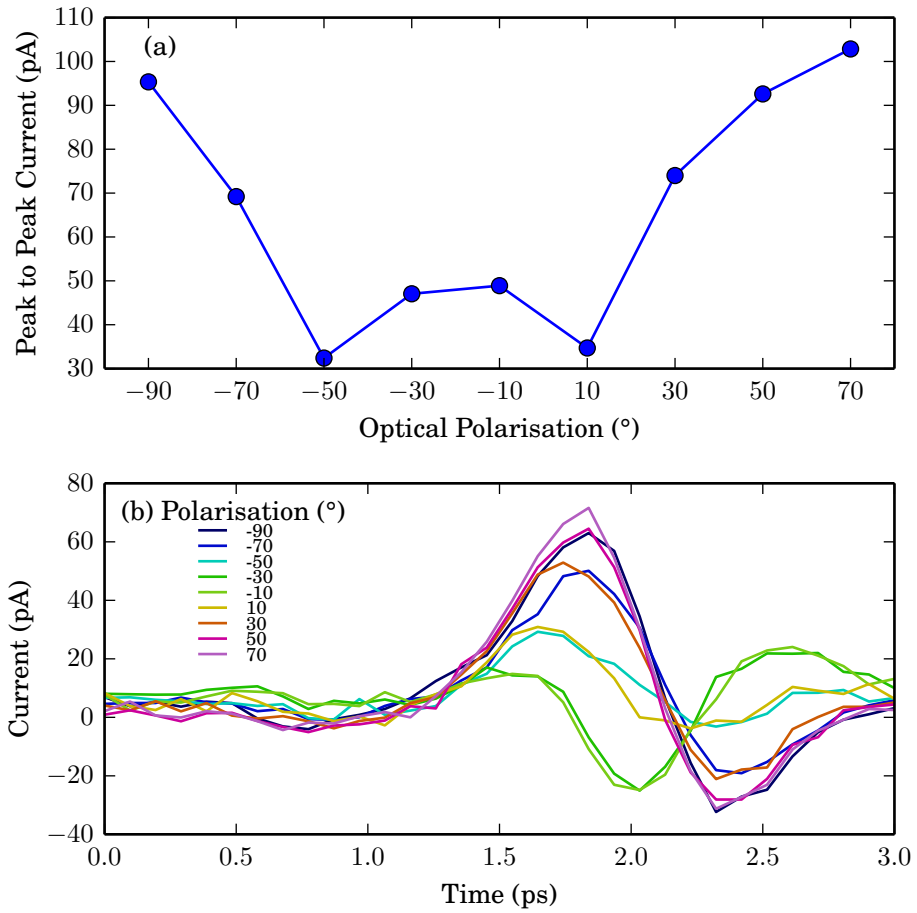

Figure 4.15: Optical polarisation dependence of the uninsulated Au/Pb multiple metal emitters. The angle of 0° corresponds to perpendicular polarisation and 90° to parallel polarisation as described in chapter 3. Figure (a) shown the peak-to peak amplitude with varying optical polarisation angle and figure (b) shows the time-domain scans used for each data point in figure (a). The increased terahertz output power at 0° arises from sub-wavelength diffraction causing carriers to form nearer the metal boundary.

is attributed to the increased electron mobility at low temperatures [103], as fewer free carriers are present the free electron path length is increased. This implies carrier mobility is the main source for terahertz emission when Schottky barrier emission is removed. Both emitters show a decrease in terahertz output below 50 K which is in accordance with the reduction in electron mobility in GaAs [103]. In the case of the uninsulated emitters there is a contribution from the Schottky barriers formed at the Au/GaAs and Pb/GaAs interfaces as well as emission due to diffusion. These emitters show reduced performance when the temperature is reduced below 200 K, shown in figure 4.16 (a). This follows the temperature relationship of the Au/GaAs Schottky barrier height [104]. Between 50 K and 100 K the terahertz emission levels out and experiences a small rise in power. This coincides with the temperature region in which carrier mobility reaches its peak values and Schottky barrier height approaches its minimum values [103, 104]. If we inspect the

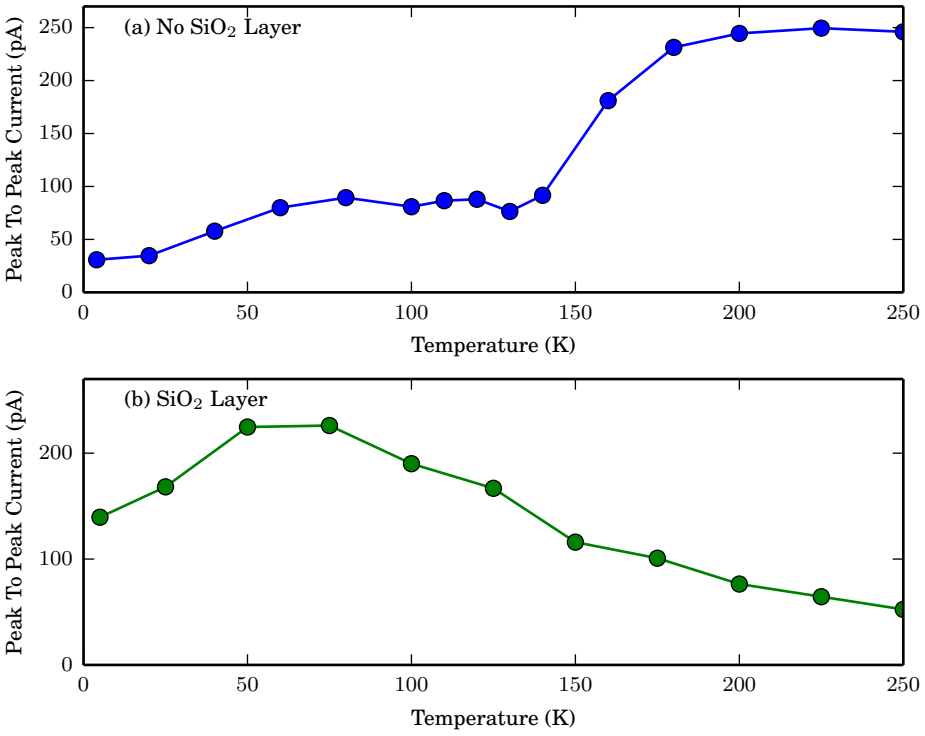

Figure 4.16: Temperature dependence of Au/Pb and Au/Pb insulated LPD emitters. Figure (a) shows the temperature dependence for the emitters without an SiO_2 layer and figure (b) with an insulating SiO_2 layer.

individual THz-TDS traces with temperature, shown in figures 4.17 and 4.18, we can see that there appears to be polarity dependence. Curiously both the un-insulated emitter and insulated emitter seem to show polarity dependence with temperature. The polarity dependence shown for uninsulated Si-GaAs, shown in figure 4.18 (b), shows a similar shift of the peak detected current in time with that observed for uninsulated SI-GaAs with fluence, with the main pule peak shifting by ∼500 fs between 200 K to 100 K. This shift does not occur in insulated GaAs, shown in figure 4.17 (b). Instead the initial peak becomes amplified at temperatures below 100 K without shifting, whereas the trough after the initial pulse shifts by 300 fs. If we compared figure 4.17 (b) and figure 4.18 (b) together, we can see that the increase in signal amplitude occurs within the same region of 50–100 K at 2 ps at the initial excitation of the pulse, without being shifted forwards in time. This rise in terahertz output is likely due to the increased efficiency in the photo-Dember effect as it is common to both insulated and un-insulated samples. The apparent reversal in signal polarity at 100 K between the emitters is due to the choice of phase selected by lock-in detection at the start of the experiments, causing an apparent change in signal polarity.

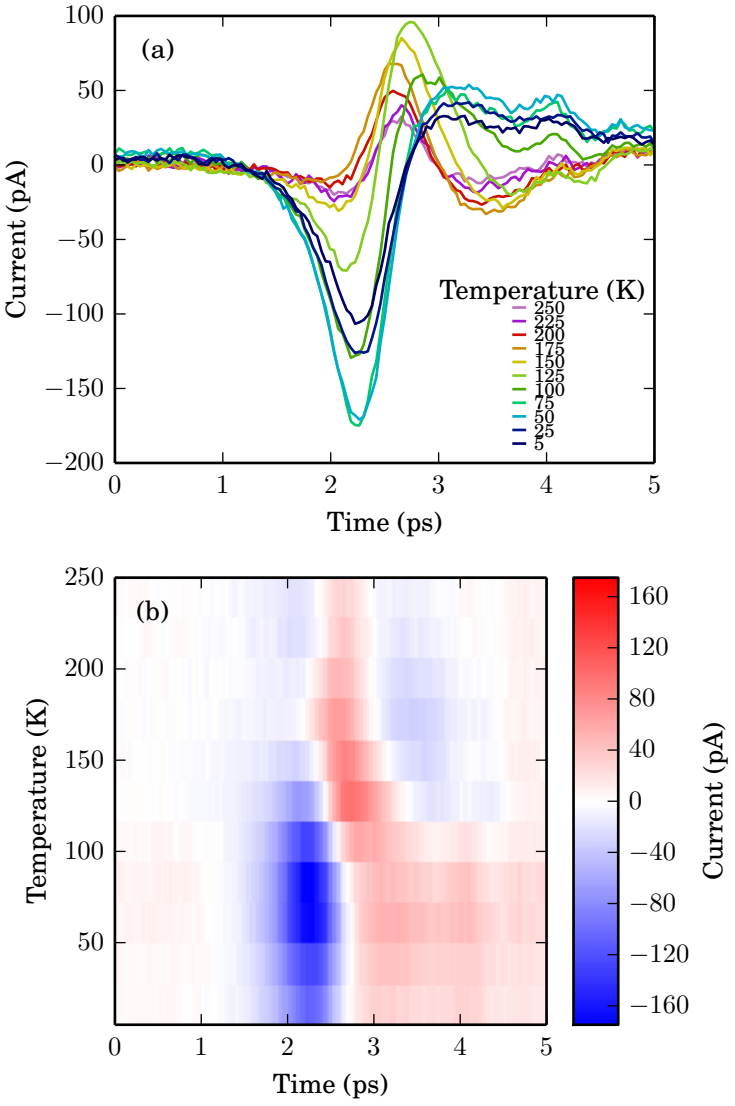

Figure 4.17: Temperature dependence THz-TDS scans of an Au/Pb multiple metal emitter fabricated with an insulating layer ranging from 5–250 K. Figure (a) shows the individual THz-TDS of detected current with time over the range of temperature. Figure (b) shows the same data as figure (a) as a two dimensional image of detected current against temperature and time.

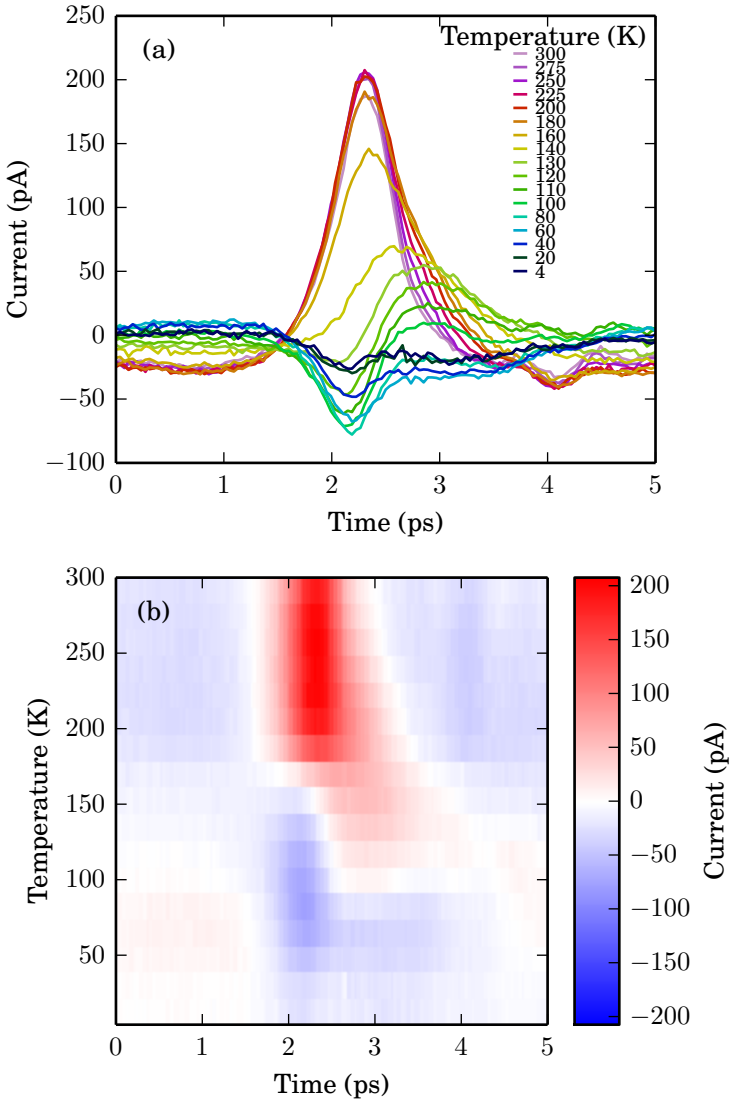

Figure 4.18: Temperature dependence THz-TDS scans of an Au/Pb multiple metal emitter fabricated with no insulating layer ranging from 5–250 K. Figure (a) shows the individual THz-TDS of detected current with time superimposed with each other over the range of temperature. Figure (b) shows the same data as figure (a) as a two dimensional image of detected current against temperature and time.

4.4 Conclusion

We have demonstrated robust, simple to fabricate terahertz emitters based on both the LPD effect and the Schottky barrier effect. These emitters should be substantially more robust compared to existing photoconductive antennas due to the lack of applied bias causing electro-migration, and the ability to scale for little cost over a large area reduces saturation The main source for emission at room temperature is due to band bending from the Schottky barrier. We also show that the LPD effect plays a role in the terahertz emission that becomes more apparent at low temperatures of 50–80 K in accordance with increased electron mobility.

We demonstrate effective terahertz emission but there is scope for improvement by choosing different metal pair to optimize the amount of Schottky currents. However, because the Schottky barrier heights are highly dependent on surface quality due to oxidation of the surface it is difficult to predict the strength of the emission without fabricating the emitters. The amount of LPD emission can also be optimized further by choosing different metals and thicknesses to enhance the quenching difference between the chosen metal pairs. Due to their lack of voltage bias requirements double-metal terahertz emitters allow for passive terahertz generation and increased robustness and may suit applications where wire-bonding would be difficult.

Degradation of the Pb surface quality of the metal strips may be an issue for long term performance. The rapid oxidation of Pb leads to the optical quality degrading with time, causing the metal to percolate and clump. While this is a consideration to bear in mind the Pb based emitters have continued to function over so far over a period of a year without incident.

Chapter 5

Plasmonic Lateral Photo-Dember Emitters

As demonstrated in chapter 3 we can create multiplexed LPD emitters by creating a net dipole per repeatable element, either by asymmetrical optical illumination [8] or reflectivity[6]. The drawback of using asymmetrical optical illumination is the careful alignment of the lens array required to match the pitch of the grating is the array of LPD emitters. Using multiple metals as repeatable emitters remedies this problem, but instead shifts the difficulty in alignment to the fabrication stage. Using two different metals requires a two-stage fabrication process, with surface quality of the semiconductor playing a major role in the Schottky field [89]. Ideally a multiple emitter would be constructed from a uniform material that could operate under uniform illumination using lithography for fabrication. Klatt et al. demonstrated this by using gold evaporated at an angle [53] where the decreased thickness of gold allowed for asymmetrical reflectivity across a repeatable emitter. However the method demonstrated still requires a two-stage fabrication. Initially "walls" of aluminium are constructed on a semiconductor with a high aspect ratio using thermal evaporation, and then gold is evaporated at an angle onto the surfaces to create wedges.

In this chapter we detail how a repeatable LPD emitter could be fabricated from one metal using extra-ordinary optical transmission to enhance the optical intensity under the surface of the semiconductor. This would have the advantage of reducing the complexity of fabrication demonstrated in Klatt et al's emitters [53] or the careful alignment of the double metal LPD emitter geometry presented in chapter 4 [6]. A plasmonic emitter fabricated from one material using lithography results in more scalable fabrication, opening up avenues to patterning LPD emitters over large areas.

Extra-ordinary transmission is a plasmonic effect that creates enhanced localised transmission compared with a bare substrate [105]. Extra-ordinary transmission is demonstrated by patterning sub-wavelength hole arrays on a metal sheet. At certain frequencies

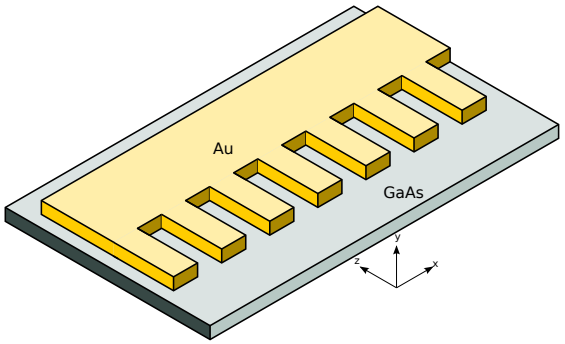

Figure 5.1: Diagram showing the geometry of the repeatable plasmonic LPD emitter. The comb structure on the yx plane acts as a plasmonic grating increasing the absorption of the optical beam into the substrate when light is polarised along the $\vec{x}$ axis. The relative increase in absorption creates an asymmetric carrier distribution, causing a net lateral dipole per emitter unit cell.

the sheet becomes highly transparent to the optical beam; the centre frequency of the transmission depends on the lattice constant, depth and frequency [106]. The optical transmission from this array of sub-wavelength holes is much higher than that predicted by standard aperture theory [107], where the transmission is limited by the aperture area. The increased transmission is due to surface plasmon polaritons (SPPs) that guide light across the surface of patterned metal into the hole array. The extra-ordinary transmission via SPPs allows enhanced coupling of the optical beam into specific regions of optical devices. If a plasmonic array is used to increase the transmission of optical light into the substrate, carrier generation increases. As a result we can use plasmonic gratings to tailor the initial carrier distribution on an LPD emitter. As explained in the introduction, a solid metal strip line will not create terahertz emission via the LPD effect due to the symmetric carrier distribution; the dipoles created on either side of the metal strip are equal and opposite. If a plasmonic grating is used on one side of the metal strip, as shown in figure 5.1, the optical intensity one side of the strip is increased. The increase in optical intensity results in the dipole formed by the plasmonic grating to be larger than the solid strip line. If this is the case then the difference in dipole strength causes a net lateral dipole, as is the case examined in chapter 4. Within the region of the plasmonic grating the optical transmission can be greatly enhanced near the centre wavelength of the optical pulse while also being highly reflective in the terahertz region due to the substantially smaller feature size. Such a “comb” geometry illustrated in figure 5.1 has been demonstrated recently using photo-conductive emitters for multiplexed operation [108]. The geometry is based around the same non-uniform illumination in the semiconductor surface to tailor the initial carrier density. Inter-digitated electrodes use the optical enhancement to selectively enhance electrode pairs, creating a net current when under optical illumination.

Plasmonic enhancement of photoconductive emitters has been demonstrated as a method

to improve the conversion efficiency of terahertz generation. Extra-ordinary transmission has been demonstrated with photo-conductive terahertz emitters to increase the optical coupling into the substrate. The use of sub-wavelength slits was investigated by Hsieh et al. by considering the guided modes along though a series of thin metallic slits [109]. In this analysis no explicit modelling of SPPs takes place; the modelled conditions are for a perfect metal waveguide. Using this analysis Hsieh et al. [109] found that a set of heights h that supported enhanced transmission into the substrate corresponding to the "open pipe" modes where enhancement occurs when $\lambda_{\text{Optical}} = \frac{2h}{i}n$, where λ_{Optical} is the optical wavelength, i is the set of positive integers and n is the refractive index of the material in the waveguide. Heshmat et al. demonstrated this experimentally using repeating slits in gold on SI-GaAs to make a plasmonic enhanced terahertz antenna acting as a receiver [110]. Heshmat et al. fabricated plasmonic structures were 300 nm deep 100 nm slits with a 700 nm period on a photoconductive reciever, with the design found by iterating through FDTD simulations to find the optimal transmission into the semiconductor substrate. The results for the plasmonic enhanced receiver showed competitive results in recorded amplitude with an LT-GaAs photoconductive receiver despite using a SI-GaAs which as a longer lifetime. Park et al. demonstrated the use of plasmonic gratings between the electrodes of a photoconductive antenna, shown in figure 5.2, to increase the absorbance of light within the electrode gap [111]. In Park et al.'s work, the plasmon enhancement is referred specifically as *local* surface plasmon resonances rather than surface plasmon resonances. Again, the optimal geometry was derived from a FDTD model. Park et al. show simulationed enhancement by the rotating the optical beam polarisation. The polarisation controls the sub-wavelength enhancement at the edge of the metal structure similar to the effect described in chapter 3.

Berry et al. developed this concept using the plasmonic grating to increase the conversion efficiency of the optical beam to terahertz emission by concentrating the optical pump beam at the antenna electrodes [112, 113]. The enhanced transmission was achieved using a 200 nm period grating patterned on the antenna electrodes, using light at normal incidence. The optimal geometry was also obtained by iterating through the grating geometry using COMSOL. This increased coupling of light allowed the terahertz emitter to function with a substantially higher efficiency by using SPPs to guide the pump beam to the antenna electrodes. Berry et al. also have demonstrated the possibility of using two sets of plasmonic gratings as a modulation method for controlling the amplitude of the terahertz emitter [114]. Changing the relative grating alignment the transmission of the system can be altered and the optical power into the emitter substrate can be changed rapidly. Improvements in performance have also been demonstrated using hexagonal nano-structures instead of a grating by Jooshesh et al [115]. The hexagonal grating was patterned between a photoconductive antenna's electrodes and demonstrated enhanced coupling of the optical beam with the substrate, leading to increased terahertz generation. It should be noted that the design strategy for observing the increase in terahertz generation stems from iterating through a set of constant frequency simulations

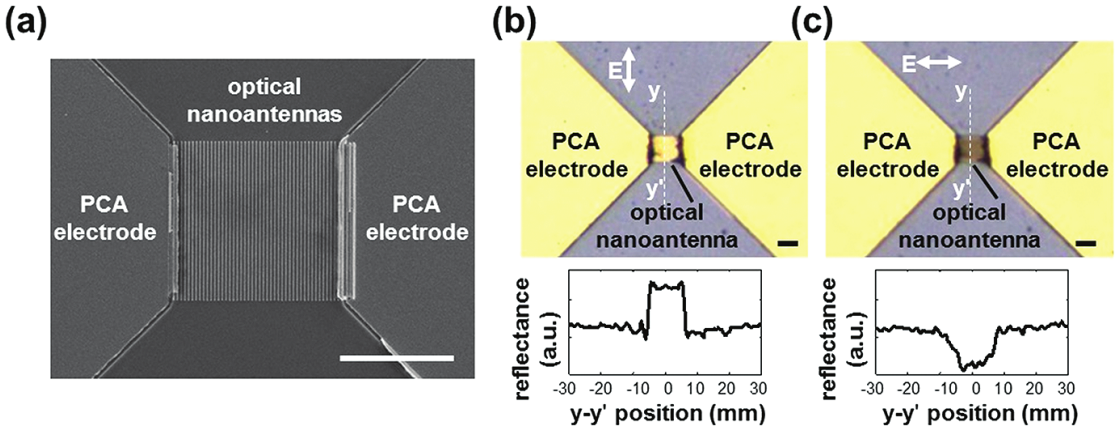

Figure 5.2: A terahertz photoconductive antenna with a plasmonic grating to enhance the optical absorption, reproduced from Park et al [111]. (a) Shows a SEM scan of the plasmonic grating on the photoconductive electrode, (b) and (c) show bright-field microscope images of the antenna with parallel (b) and perpendicular (c) optical polarisation. The optical absorption is shown by the dark region on the electrodes in figure (c) with a reflection profile.

either using finite difference time domain (FDTD) or finite element method (FEM). As well as structured geometries random surface roughness caused by percolation of the metal coating increases the optical absorption, enhancing terahertz performance. Park et al. demonstrated that a rough surface caused by percolated silver film enhanced the terahertz output power between photoconductive electrodes [116]. Ramakrishnan et al. demonstrated that a 8 nm layer of gold on a CuO_2 substrate caused enhanced terahertz emission due to the confinement of the optical beam to the depletion region [117]. Instead of using a photoconductive emitter, Ramakrishnan et al. used a Dember geometry emitter angled at 45° to the THz-TDS receiver, using intrinsic carrier drift. Trapping the optical beam close to the semiconductor depletion region causes more carriers to be generated within the region of the Schottky field, causing enhanced diffusion. From this literature it appears that plasmonic enhancement is a viable candidate for controlling the optical absorption into a terahertz emitter; the optical intensity can be chosen selectively by geometry to aid terahertz generation.

The exact mechanism for the plasmonic enhancement frequently left unspecified in the terahertz antenna design in scientific literature; i.e. the plasmon properties are not clearly attributed to local surface plasmon modes, or propagating surface plasmon modes. In the simulations presented here, we show similar results for in optical absorption for a single element compared to an array of elements, suggesting that the mechanism is a local effect.

An aperture causes diffraction of transmitted light. A Fraunhofer diffraction model of a sub-wavelength slit shows the transmission coefficient T tends to zero when the aperture size r is smaller than the wavelength λ_0. The transmission coefficient T is defined as the ratio of total transmitted intensity through the aperture over the incident intensity I_0.

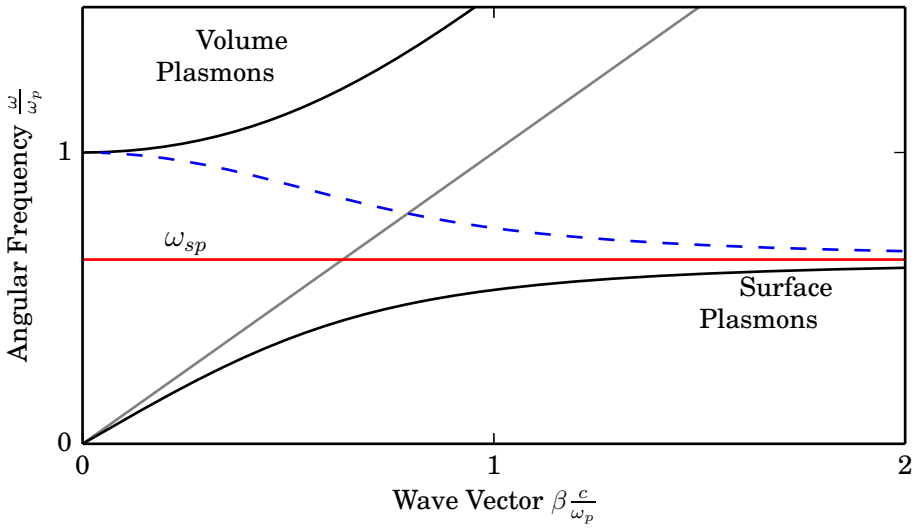

Figure 5.3: A plot of equation (5.2) with $\frac{\omega}{\omega_p}$ against $\beta\frac{c}{\omega_p}$ showing the dispersion curve of SPP modes of an ideal Drude metal with $\epsilon_2 = 1$. The black line shows the real part of β and the dashed blue line shows the imaginary component of β. The grey line shows the dispersion curve for light k_0. The red line shows the surface plasmon frequency ω_{sp}.

As a result the transmission coefficient $T \sim 1$ for $r > \lambda_0$, where almost all of the light is transmitted through the aperture without loss. For an aperture in a perfectly conductive thin metal sheet the transmission for a plane wave is [107]

$$T = \frac{4\pi^2}{27}\left(\frac{r}{\lambda_0}\right)^4 n. \tag{5.1}$$

This limit implies very weak transmission at low frequencies. The Bethe-Bouwkamp model only applies for decaying modes if the metal screen is thick compared to the wavelength [107]. If the aperture supports wave-guiding modes the Bethe limit does not apply, allowing T to be much higher. These wave-guiding modes allow for enhanced transmission with a perfect electrical conductor, however this does not apply for thin optical sheets with finite conductivity. The limit on T can either be bypassed using surface propagating plasmon (SPPs) that form on a periodic metal surface of apertures or localised plasmons for single sub-wavelength elements allowing $T > 1$. SPPs channel light over surface metal to the aperture allowing for light to be passed through the aperture. The increased effective light capture area allows for $T > 1$, and it is this effect that is called extra-ordinary transmission.

5.1 Plasmonic Grating Background

A plasmon is described as the collective oscillation of electrons within a metal structure that is formed as a reaction to the optical pulse. The electronic structure of an ideal

metal can be modelled as a free electron gas, known as the Drude model. We can model the displacement of charge, as shown in appendix A, to find the dispersion relationship β [118]. The displacement causes an oscillation in the electron density of the metal causing a propagating wave that is referred to as a plasmon. Plasmons that propagate as a wave of charge displacement through the bulk of the metal are referred to as "volume plasmons" and those that propagate along the surface are referred to as "surface plasmons". By deriving the dispersion curve β in appendix A bulk plasmons are shown to only occur above the plasma frequency in a metal. The dispersion relationship β is

$$\beta = \frac{\omega}{c}\sqrt{\frac{\epsilon_2(1-\frac{\omega_p^2}{\omega^2})}{\epsilon_2+1-\frac{\omega_p^2}{\omega^2}}}. \tag{5.2}$$

The dispersion relationship β is plotted in figure 5.3 showing the real (black) and imaginary (blue) components. For $\frac{\omega}{\omega_p} > 0$ real solutions exist corresponding to the volume plasmon modes described in equation (A.12). The other regime is the bound plasmon modes where the real part of β is greater than k_0, shown on the plot figure 5.3 as to the right of the light dispersion line, plotted in grey. In this mode the SPPs are bound to the dielectric interface, and approach the surface plasmon frequency ω_{sp}, where

$$\omega_{sp} = \frac{\omega_p}{\sqrt{1+\epsilon_2}}. \tag{5.3}$$

As $\omega \to \omega_{sp}$, $\beta \to \infty$. The SPP acts as a resonant mode near ω_{sp} allowing the energy to be propagated by the surface plasmon mode, and it is this that allows for enhanced energy flow into a substrate. However on a standard air interface surface polaritons do not couple with the optical beam due to phase matching; the only accessible SPP modes do not cross the grey light line. Prisms can be used to provide a crossing point between the light line and the SPP modes by creating a region of three dielectric interfaces. However this condition can also be satisfied by creating a grating on the surface of the metal to change the light momentum. By creating a periodic metal array we can use SPPs to provide the extra-ordinary enhanced transmission by using the surface plasmon to couple into the substrate. This grating can also be fabricated in a metal, such as silver, that already supports SPPs to create "spoof" surface plasmon polaritons [119], which otherwise would not be supported by a bare metal-dielectric interface. The grating can either be a raised array of metal or an array of holes into the substrate, or even a random surface roughness [118, p47]. If we create a 1D grating with periodicity a_0 the supported plasmon modes create a condition for momentum matching [120]. If we consider the grating momentum $G_x = \frac{2\pi}{a_0}$ then conservation of momentum leads to

$$\vec{k_{sp}} = \vec{k_x} \pm i\vec{G_x}, i = 0, 1, 2, 3 \ldots \tag{5.4}$$

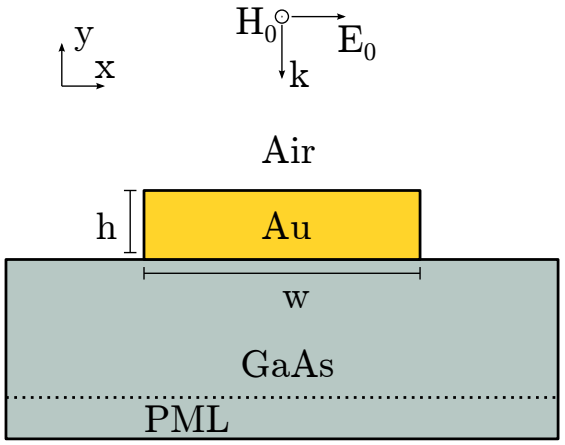

Figure 5.4: A diagram showing the model geometry used in the COMSOL model. Periodic conditions on the x axis are used to model a unit cell of a rectangular $w \times h$ gold grating element on a GaAs substrate.

where $\vec{k_{sp}}$ is the momentum of the SPP and $\vec{k_x}$ is the component of the incident wave vector on the same plane as the grating. If we use the plasma dispersion for a smooth film from equation (A.27) we can set the condition that the plasmon modes must correspond to the grating periodicity. If $k_x = 0$ for normal incidence then combining equation (5.4) and equation (A.27) leads to the condition

$$i\lambda_{\mathrm{SPP}} = a_0\sqrt{\frac{\epsilon_1\epsilon_2}{\epsilon_1+\epsilon_2}}, i = 0, 1, 2, 3\ldots \tag{5.5}$$

where λ_{SPP} is the wavelength of the optical beam. This condition should be satisfied either side of the interface, for $\epsilon_1 = \epsilon_{\mathrm{Air}}$ and $\epsilon_1 = \epsilon_{\mathrm{GaAs}}$. The effective refractive indices of each material propagating around the dielectric-metal boundary are given as the term in equation (A.27) as

$$n_{\mathrm{SPP}} = \sqrt{\frac{\epsilon_1\epsilon_2}{\epsilon_1+\epsilon_2}} \tag{5.6}$$

Allowing us to calculate the wavelength of the SPP as $\lambda_{\mathrm{SPP}} = n_{\mathrm{SPP}}\lambda_{\mathrm{optical}}$. Calculating the effective refractive indices for our system using equation (5.6) we find that $n_{\mathrm{SPP\ Air}} = 1.023 - 0.002i$ in air and $n_{\mathrm{SPP\ GaAs}} = 5.910 - 0.019i$ in GaAs at 800 nm optical wavelength. We expect the condition to be equal to roughly 6 modes within the GaAs substrate to 1 mode for the gold-air interface, which will constrain our geometry shown in figure 5.4

5.2 Simulation

We modelled a simple 1D grating of gold on a GaAs substrate with a 2D finite element COMSOL model to calculate the optical transmission into the semiconductor substrate

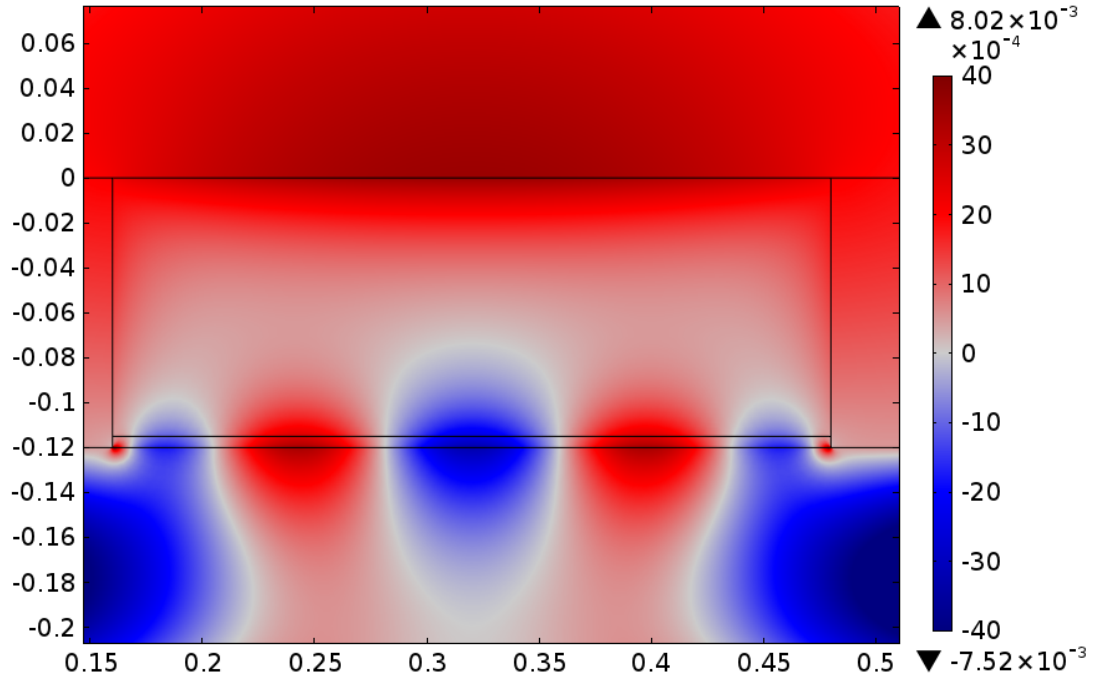

Figure 5.5: A COMSOL model of the z component of the magnetic field of the grating element for the dimensions of maximum transmission, $w = 320\,\text{nm}$, $h = 120\,\text{nm}$ for $n = 1$. The SPP modes on both the top and bottom of the element are clearly visible, with the fundamental mode on the top surface and the 4th harmonic on the bottom.

through a plasmonic grating. The COMSOL model was constructed with each material being based on the complex reflective index $\tilde{n} = n + i\kappa$ of gold [121] and GaAs [122] at 800 nm. Refractive indices interpolates data from the results given by Rakic et al. for gold [121] and Aspnes et al. for GaAs [122] allowing the optical frequency to be adjusted. For $\lambda_{\text{Optical}} = 800\,\text{nm}$ $n_{\text{Au}} = 0.188 + 4.71i$ and $n_{\text{GaAs}} = 3.68 + 0.085i$ The model geometry was defined as the unit cell of a gold grating element with width w and height h shown in figure 5.4. Periodic conditions on the x axis were matched so that the cell was repeated along the x axis to form a grating. The top y boundary was defined as the optical source with wave vector direction $\hat{k} = -y$ and $E_0 = x$. The bottom y boundary was defined as a perfectly matched layer to fully absorb the optical beam after it being transmitted A distance of 4 µm was used between the grating structure to the top and bottom boundaries to remove artefacts caused by reflection. Around the grating structure additional geometry was created to adjust the mesh size near the gold boundary so the region of interest could be studied in detail while maintaining reasonable time to complete the simulation. The model sets to optical wavelength to 800 nm while varying w and h, keeping the grating periodicity at $a_0 = 2w$. The refractive index on the surface of the grating, n, allows variation as well, and is set as purely real.

The COMSOL model shows the formation of the SPP modes in the grating element, as shown in figure 5.5. The electric field penetrates into the metal and with the SPP

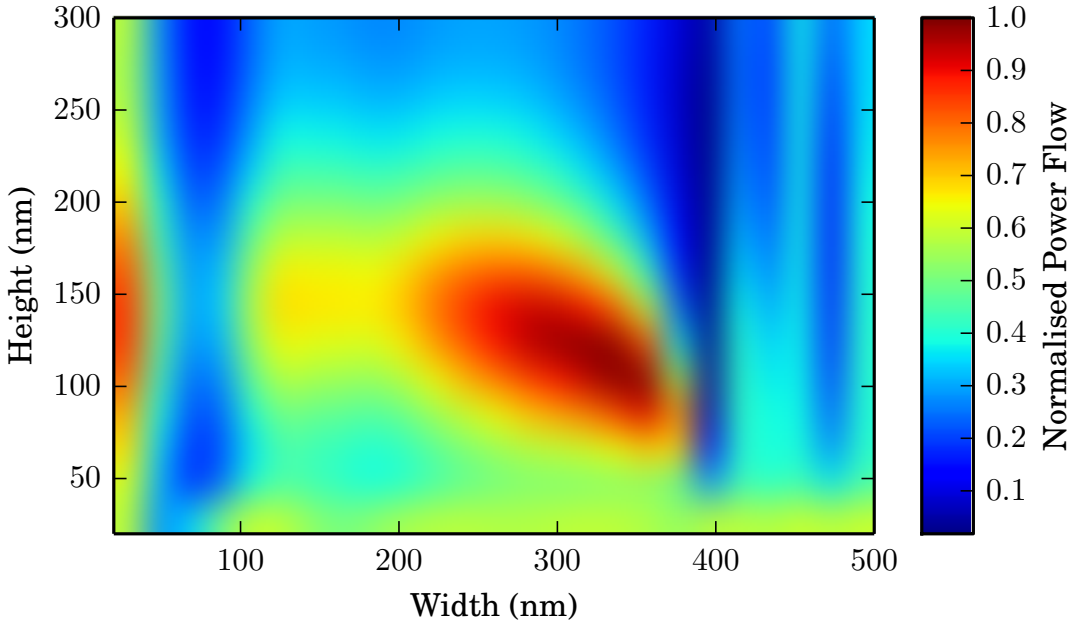

Figure 5.6: A plot showing the normalised power flow in colour of the described COMSOL model with varying width w and height h of the optical element with the surface refractive index, set at $n = 1$. There is an enhancement for $w = 320\,\text{nm}$ and $h = 120\,\text{nm}$.

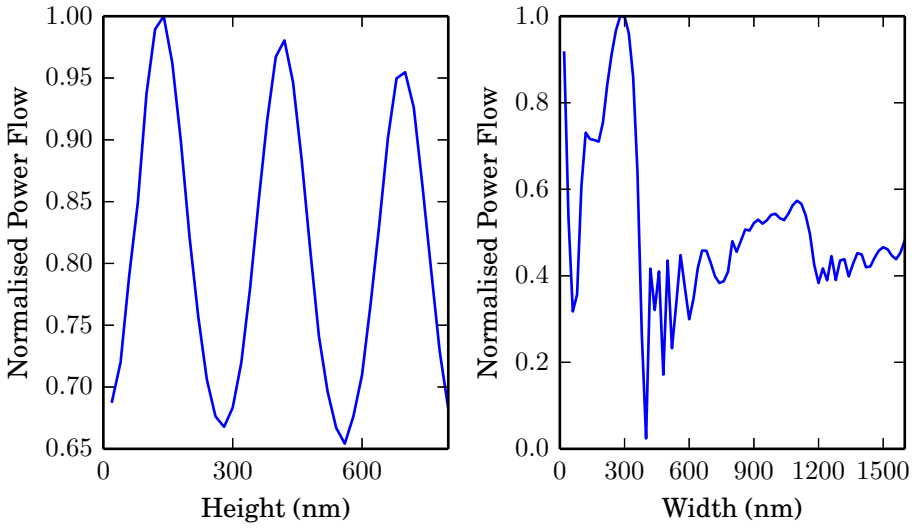

Figure 5.7: Extended 1D slices of figure 5.6 (a) A plot of the normalised power flow in the COMSOL model against h with fixed $w = 320\,\text{nm}$. (b) Power flow against w with fixed $h = 140\,\text{nm}$ showing maximum enhancement at $w = 320\,\text{nm}$.

modes guiding the optical power into the substrate. figure 5.5 shows the z component of the magnetic field H_z for the dimensions of maximum transmission, $w = 320\,\text{nm}$, $h = 120\,\text{nm}$ for $n = 1$. The SPP modes on both the top and bottom of the element are clearly visible, with the fundamental mode on the top surface and the 4th harmonic on the bottom. By sweeping element width w and height h we find the optimum transmission for the element geometry by calculating the $-y$ component of the electromagnetic power flow $\vec{S}$ on the exit port of the model before the PML region. The results are shown for a surface refractive index of $n = 1$ for $w = 20$–$500\,\text{nm}$ and $h = 20$–$300\,\text{nm}$, with step sizes in w and h of $20\,\text{nm}$. In figure 5.6 we can see for small widths of $w = 20\,\text{nm}$ there is a maximum transmission that occurs at $h = 150\,\text{nm}$. Figure 5.7 extends the range of figure 5.6, plotting the normalised power flow against h with fixed $w = 320\,\text{nm}$. At this width ($w = 320\,\text{nm}$) there are also maxima in the power transmission that occur at 42 nm and 70 nm, which we expect correspond to $h = \lambda_{\text{SPP}}/4$, $\lambda_{\text{SPP}}3/4$ and $\lambda_{\text{SPP}}5/4$ modes. However, these are not multiples of the expected wavelengths as calculated from the refractive index for $n_{\text{SPP Air}}$ for the gold-air interface, which is close to 1. If this is true we expect $\lambda_{\text{SPP}}/4 = 200\,\text{nm}$, which is not the case observed within the model. At these modes the magnetic field $\vec{H}_z$ is at zero on the substrate surface and a maximum on the top of the grating element. This height also corresponds to the local maximum observed for the grating element where $w = 320\,\text{nm}$ and $h = 120\,\text{nm}$. Figure 5.7(b) extends the range along w keeping h=140 nm showing no further distinguishable resonant modes except a slight enhancement at w=1.1 µm. If we plot the z component of the magnetic field H_z as in figure 5.5 for the resonant element dimensions we can clearly see the SPP modes forming around the metal structure. Plotting H_z does not show the large enhancement in the electric field near the corners, as is the case in chapter 3. In the resonant element the fundamental SPP mode covers the whole of the plasmon surface, and the 4th harmonic of the fundamental is present in the substrate.

I also attempted to simulate the effect of a single grating element, plotted in figures 5.8 and 5.9, to observe the influence of the repeating boundary condition, to see if the enhancement was purely due to local surface plasmon modes. In this case the height of the emitter does depend what appears to be the standing modes of the plasmon resonances, shown in figure 5.8, but the local enhancement occurs at much higher aspect ratios, were $w = 140\,\text{nm}$ and $h = 180\,\text{nm}$ for $n = 1$. The COMSOL model does not assume an ideal Drude model metal for the FEA calculations which may impact the comparison of the results. The height of the emitter is not affected by the scattering boundary, showing a $\lambda_{\text{SPP}}/4$ mode, but the modes underneath the metal mask are more heavily restricted to $w < 300\,\text{nm}$. While this high aspect ratio means that a single element plasmonic element would be very difficult to fabricate, it does indicate that the plasmonic enhancement can be argued not to be a “pure” propagating surface plasmon as described by grating phase matching.

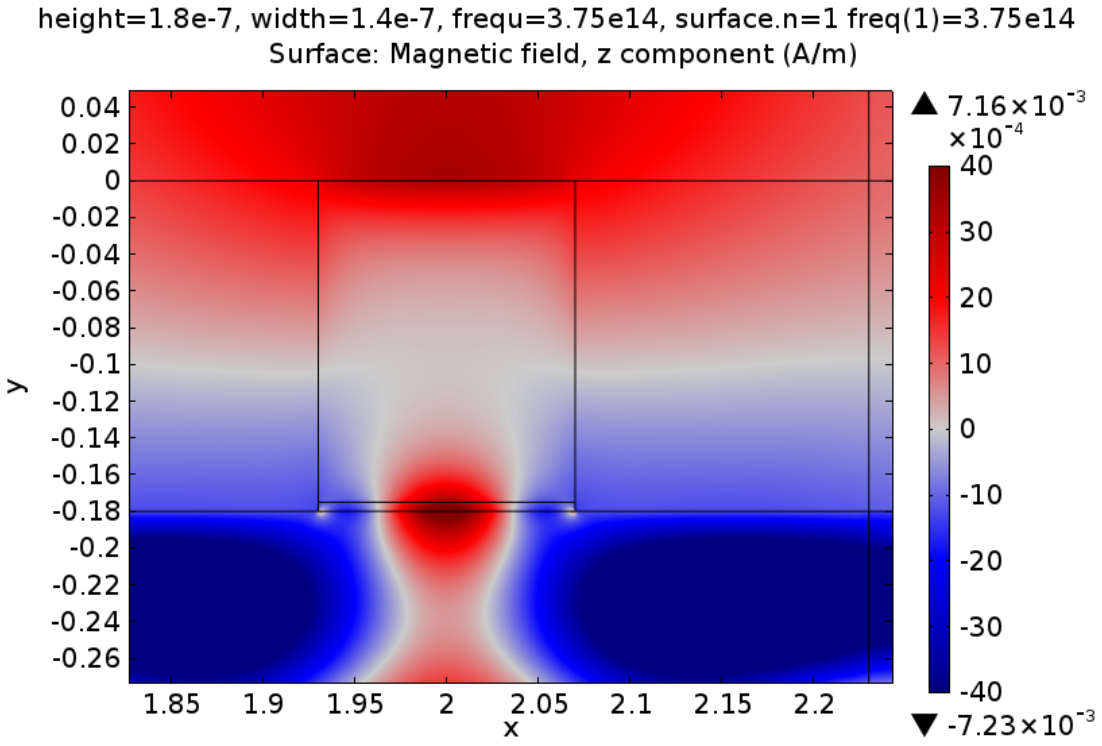

Figure 5.8: Scattering boundaries are used instead of repeating boundaries in a repeat of the simulation from figure 5.5. As in figure 5.5 the refractive index of the surface $n = 1$ showing the normalised power flow of the described COMSOL model with varying width w and height h of the optical element. The maximum local enhancement changes the optimal geometry to $w = 140\,\text{nm}$ and $h = 180\,\text{nm}$.

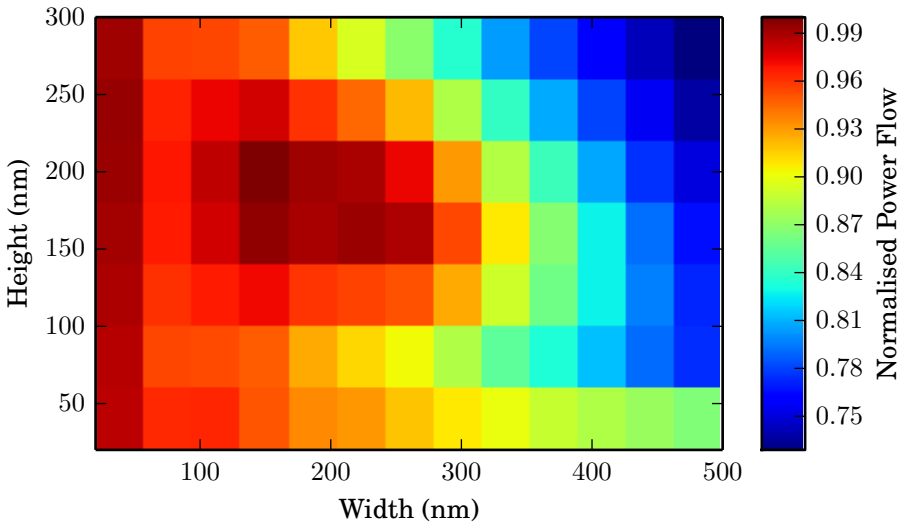

Figure 5.9: A plot showing the parameter sweep of the simulation plotted for figure 5.8. The maximum local enhancement changes the optimal geometry to $w = 140\,\text{nm}$ and $h = 180\,\text{nm}$.

5.3 Fabrication

The fabrication of the plasmonic grating for LPD emitters requires using a technique to cover a reasonably wide area(over 1 mm) for testing purposes. As a result using techniques such as focussed ion milling (FIB) I deemed impractical for a scalable technique, though available photo-lithography means that sum-1 µm structures are not realisable in small testing runs. Due to these constraints electron beam lithography was selected to fabricate the plasmonic gratings, being able to provide >100 nm resolution at metal thickness controlled by thermal evaporation. Since the grating geometry did not have strict requirements for continuity matching I planned to tile an array of grating designs over a large area. Tilling the array would involve optimising the lithography procedure to be reliable enough to expose accurately without over or under exposure to ensure the fine structure. To ensure this I created a test pattern with a range of grating periods to attempt to find an optimum procedure and exposure time. I attempted to fabricate a series of plasmonic gratings in the geometry shown in figure 5.1 using scanning electron beam lithography with MMA and PMMA. PMMA (poly methyl methacryllate) and MMA (methyl methacryllate) are positive electron-beam resists, left after the development process when exposed to the electron beam. MMA was spun onto a SI-GaAs wafer for 40 s at 4000 RPM, followed by a bake on a hot plate at 115 °C for 60 s. The process is repeated with PMMA, resulting in a harder surface layer to provide an undercut for the developer to achieve higher spatial resolution. The grating geometry of the "comb" structure was defined and exposed using the RAITH electron beam control software, with a dose rate experimentally found for each exposure. The resist was developed with MiBK, rinsed with isopropanol (IPA) and water leaving the resultant structures defined as gaps within the resist. 5 nm of chrome and 100 nm of gold were evaporated onto the sample using thermal evaporation, and then left in acetone for 24 hours to lift off the metal adhered to the resist. The main challenge faced initially was the extreme variation in dose rate from each run, resulting in either solid regions of metal where the grating was exposed, to no visible features present. Typically dose rates varied from 30% to 40% the calculated dose rate with exposure steps at 2% taken to find a suitable dose that allowed the gratings to form as shown in figure figure 5.11. Once this was achieved difficulties were encountered with the adhesion of the metal between the gaps forming the grating. The high aspect ratio of the structures due to the height of the metal made penetration of the acetone to the resist difficult, frequently leaving the exposed structure as a solid block as sown in regions of figure 5.11. The long lengths of grating made the fabricated structures very fragile, with the grating elements shearing during lift-off in acetone as can be shown in figures 5.10 and 5.12. These difficulties encountered were found to be due to the surface quality of the material. Use of plasma ashing in oxygen to remove organic compounds on the surface improved results with electron beam lithography, but lift-off problems in acetone persisted making fabrication unreliable.

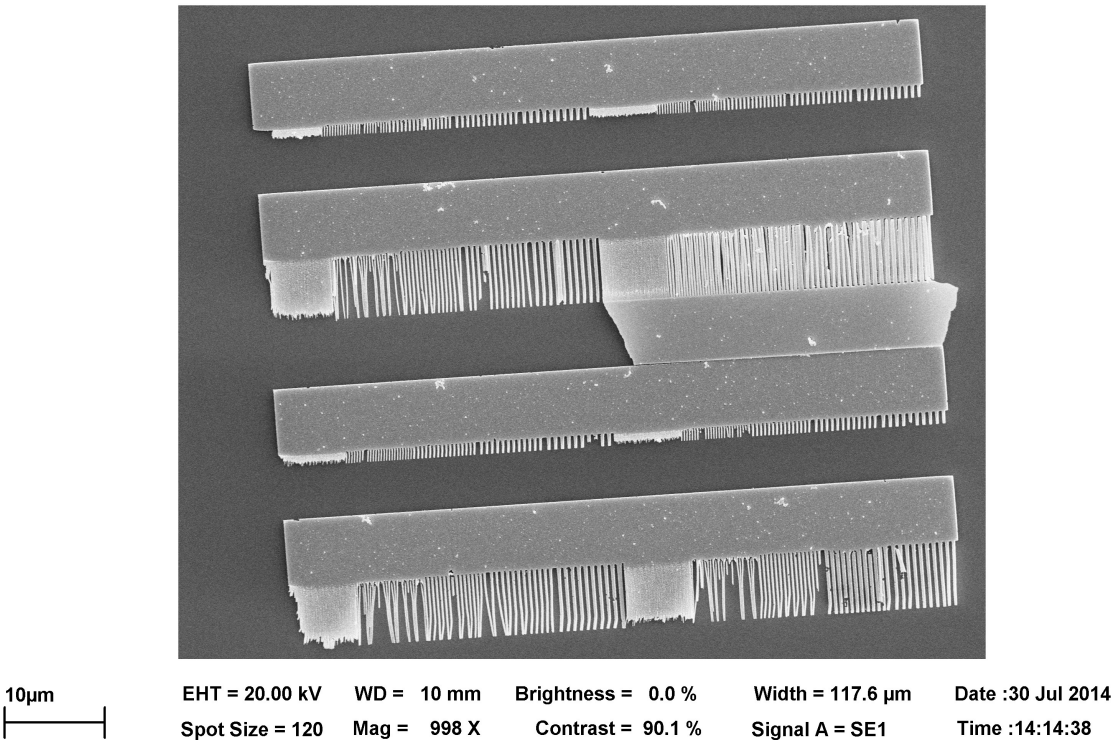

Figure 5.10: SEM image showing the attempted fabrication of a plasmonic single metal LPD emitter fabricated by electron beam lithography. The fabricated emitter consists of a 100 nm layer of gold on GaAs. One side of the metal strips is structured with periodic comb structures to create the plasmonic enhancement in the semiconductor underneath. Difficulties with the lift-off of exposed resist cause large sections of the metal to remain attached to the semiconductor.

None of these challenges are insurmountable, but they do provide difficulties for fabricating a region of plasmonic emitters with an area large enough to test in comparison to the multiple metal emitters. As a result if plasmonic emitters are demonstrable, the scaling of fine structure over a large area would continue to be a challenge for electron beam lithography. If the plasmonic emitters are fabricated, they should be easily testable using the same method as shown by Park et al. [111]. The optical absorption can be identified under a bright-field microscope and quantified with reflectivity measurements.

5.4 Conclusion

The groundwork for SPP enhanced terahertz emitters exists, with previous work showing that the enhancement in the optical pump beam leading to more efficient terahertz emitters [109–115]. If the enhancement described for photo-conductive emitters exists as described, it is a viable candidate for LPD emitters. However the modelling work done shows a poor correlation with the expected SPP modes, showing that the resonance condition occurs for unexpected fractions of the optical wavelengths when calculating the expected SPP refractive index. The fabrication should be possible to duplicate the

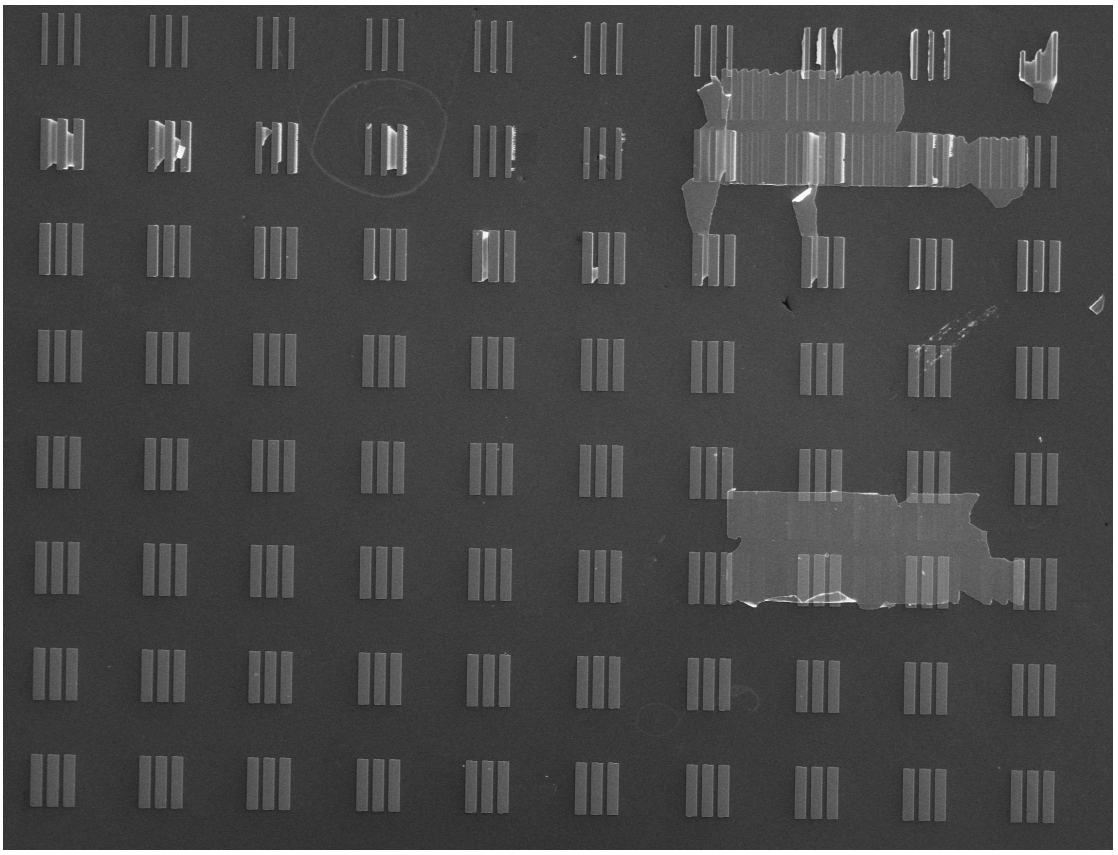

Figure 5.11: SEM image showing the effect of varying dose on the exposure of the plasmonic structure. The dose rate varies from 1% to 80% of the calculated dose, originating from the upper left corner.

geometry found in previous plasmonic terahertz emitters. In practice pattering plasmonic structures with SEM techniques is constrained by the deposition quality and scaling over large distances, which is impractical where a limited write area is available.

The efficiency of the plasmonic emitters is also likely to be less than that observed by the multiple metal emitters due to equal band-bending on both sides of the repeatable emitter. The results shown in chapter 4 demonstrate that the band bending is responsible for roughly 50% of the terahertz output power, so lacking this ability the plasmonic emitters would be less intense terahertz source in comparison, while being harder to fabricate. Given that fabrication using multiple metals on semiconductors is a well established process using photo-lithography techniques, there is limited scope in the further development of the plasmonic LPD emitters using top-down lithography techniques. A possible avenue for exploration may be to use self assembly techniques that do not require high levels of top-down precision. Examples include percolation structures that occur in thin gold, or using nano-particles to provide the plasmonic enhancement that can be selectively applied to one edge of the LPD emitter.

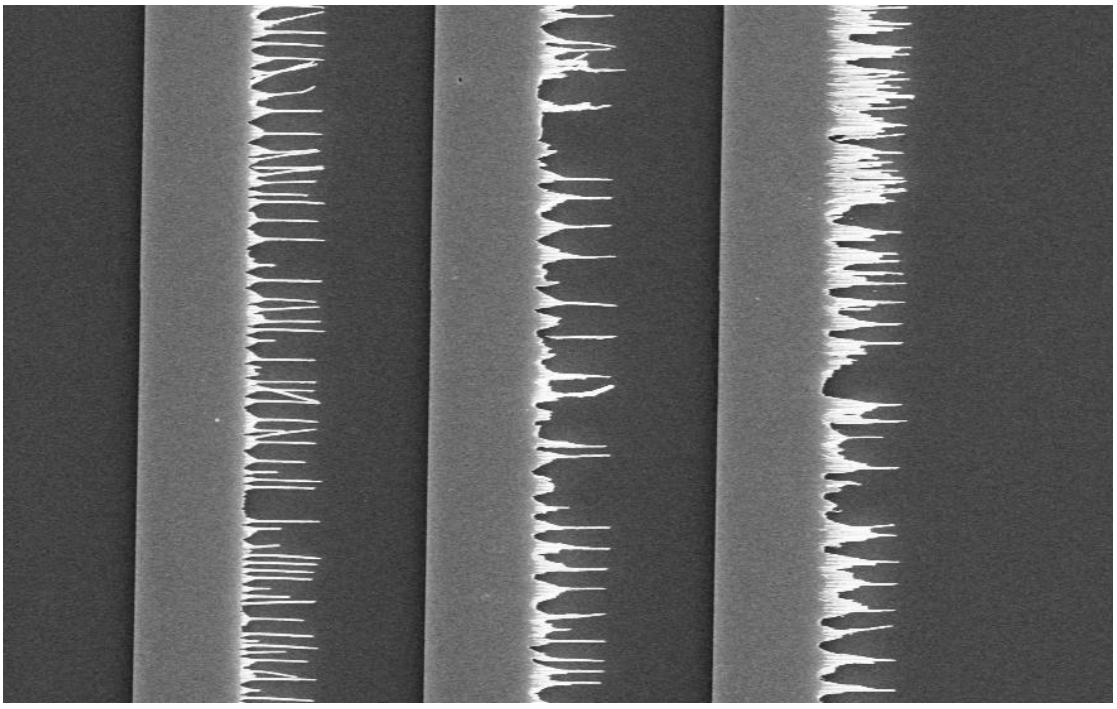

Figure 5.12: A closer inspection of the structure formed from figure 5.11 for a 42% dose. The strands from the plasmonic grating have detached from the lift-off process and tangles with each other, resulting in a non-uniform grating.

Chapter 6

Conclusion

6.1 Summary

The work of this thesis has presented the effect lateral photo-Dember (LPD) as terahertz generation mechanism, characterising the effects of optical saturation and creating a repeatable unbiased terahertz emitter. The repeatable emitter element can be scaled over a large area to overcome saturation effects and operates without an applied bias, overcoming the effects of electromigration. In the terahertz group we began by exploring the lateral photo-Dember (LPD) effect as presented by Klatt et al. I created a two dimensional model, as detailed in chapter 2, simulating the lateral diffusion. Using the model I created a triangular initial carrier distribution, and showed that a small net current was apparent. It was thought that this net current was responsible for the lateral photo-Dember effect [9]. Attempts to fabricate this triangular structure did not result in any net detectable terahertz emission, which resulted in Mark Barnes developing the dipole suppression model [3]. We demonstrated that the dipole suppression mechanism works with the current simulated with a one-dimensional drift-diffusion model to produce net terahertz emission with a THz-TDS.

In chapter 3 I tested the terahertz output semi-insulating GaAs, unannealed and annealed low temperature GaAs based LPD emitters. I found that the low-temperature annealed GaAs substrate used for photoconductive antennas required higher optical fluences to function compared with the annealed and semi-insulating GaAs substrate [1]. The annealing process required to boost the resistivity for the photoconductive antennas is not a requirement of the LPD emitters. Unannealed low temperature grown emitters demonstrate the highest terahertz output power with optical fluence and the highest saturation fluence. This output power is attributed to the excitation of carriers from trap states. Semi-insulating emitters demonstrate a flip in signal polarity, illustrating the influence of the Schottky contact with the metal. I also demonstrated the influence on optical polarisation on the LPD emitter performance. The variation in performance

was attributed to a change in carrier distribution near the metal mask. The increase in performance occurs when the optical beam is polarised perpendicular to the mask boundary. Optical diffraction from the thin metal mask creates a sharp, sub-wavelength enhancement region close to the metal boundary, which increases the performance of the LPD emitter.

I investigated the scaling of LPD emitters over a larger surface area in chapter 4. Initially this was demonstrated with a series of cylindrical lenses [8] which I improved upon by fabricating a repeatable LPD emitter [1]. The repeatable emitter consist of two metals which provide both different reflectivities in the terahertz region and different Schottky barrier heights. Both of these effects create a net terahertz pulse per repeatable emitter unit, and are simple to fabricate using photo-lithography over a wide area. I initially fabricated emitters using gold and lead on a SI-GaAs substrate, with Paul Gow investigating emitters fabricated using gold and aluminium. Of this set gold and lead emitters created the greatest amplitude pulses recorded with THz-TDS. Optical polarisation dependence was the same as the single edge LPD effect as observed in chapter 3, with the largest pulse amplitude corresponding with the optical beam perpendicular to the metal edge.

I proposed the concept of plasmonic emitters in chapter 5. Surface propagating plasmons enhance the optical intensity in a substrate with a sub-wavelength metal grating. I created a finite element model with COMSOL to demonstrate this effect for a one-dimensional grating and characterised the grating dimensions. Plasmonic enhancement with a grating would allow the fabrication of a continuous metal structure in stage without requiring a separate evaporation stage. The single fabrication stage would potentially allow simpler fabrication compared to the multiple metal LPD emitters. Using a SEM I attempted to fabricate the plasmonic LPD emitters using electron beam lithography. Due to the small structure size the grating was easily damaged, and with the limited writeable area of electron beam lithography the scaling potential of this emitter is limited compared with the multiple metal LPD emitters.

6.2 Outlook

The future of LPD terahertz emitters lies in applications where robust, bias free and scalable operation takes priority over terahertz output. As photoconductive antennas have the ability to generate with an applied voltage, a LPD emitter functioning with comparatively weaker diffusion currents will provide less terahertz output. The lack of bias restriction may aid integration with other terahertz technologies. Photoconductive terahertz emitters have been demonstrated as seeding quantum cascade lasers (QCLs) [123, 124]. The photoconductive antenna probe creates an initial terahertz pulse that is propagated into a broadband QCL structure. The QCL lases and acts as an amplifier to

the initial terahertz pulse. As a result of the coherent amplification the QCL device may be used within a THz-TDS of coherent spectroscopy at high output power. Repeatable terahertz emitters may by highly suitable for this application for integration into a single device. Whereas photoconductive antennas have to propagate either in free space into a QCL structure a series a series of LPD emitters could be patterned on the facet edge. The direct patterning would reduce the size and complexity of the seeded QCL structure.

LPD emitters are being considered for use as a CW terahertz source [125]. Photoconductive antennas can be used for generating terahertz emission at a constant frequency (CW) by photomixing [126]. The tunability of the CW terahertz emitters can also be used for spectroscopy of adsorption where the temporal use of a THz-TDS is not required. Large area LPD emitters are currently being sold commercially as alternative to photoconductive antennas, using a bi-metallic structure [127]. The devices currently available from Protemics GmbH are a repeatable terahertz emitter with integrated terahertz and optical focussing, marketed for situations where near-field excitation is of concern, such as waveguide coupling, and for robust saturation-free operation.

Appendix A

Drude Model Derivation

A plasmon is described as the bulk oscillation of electrons within a metal structure that is formed as a reaction to the optical pulse. The electronic structure of an ideal metal can modelled as a free electron gas, known as the Drude model we can model the displacement of charge [118]. The displacement of charge leads to bulk oscillations within the metal referred to as plasmons. By considering the plasmon frequency response we can derive the dispersion relation β. The equation of motion for a plasma of electrons is

$$m\ddot{\vec{x}} + m\gamma\dot{\vec{x}} = -e\vec{E} \tag{A.1}$$

where m is the electron mass, $\vec{x}$ is the position vector, γ is the damping term and $\vec{E}$ is the electric field. If the electric field has the form of $\vec{E}(t) = \vec{E_0}e^{-i\omega t}$ then the solution to the equation of motion of the plasma sea is of the form

$$\vec{x} = \vec{x_0}e^{-i\omega t}, \tag{A.2}$$

were x_0 is the complex amplitude that takes into account the phase shift. The complex amplitude used to satisfy equation (A.1) is

$$\vec{x}(t) = \frac{e}{m(\omega^2 + i\gamma\omega)}\vec{E}(t). \tag{A.3}$$

The electron sea displaced by the distance $\vec{x}$ create a polarization within the metal $\vec{P} = -nex$, where n is the electron density and e is the electric charge constant. In terms of dielectric displacement $\vec{D}$ where $\vec{D} = \epsilon_0\vec{E} + P$ equation (A.3) becomes

$$\vec{D} = \epsilon_0\left(1 - \frac{\frac{ne^2}{\epsilon_0 m}}{\omega^2 + i\gamma\omega}\right)\vec{E} = \epsilon_0\left(1 - \frac{\omega_p^2}{\omega^2 + i\gamma\omega}\right)\vec{E} \tag{A.4}$$

Where the ω_p is known as the plasma frequency, which is the natural frequency of displacement within the electron plasma.

$$\omega_p = \sqrt{\frac{ne^2}{\epsilon_0 m}}. \tag{A.5}$$

As a result we obtain from the dielectric response $\vec{D} = \epsilon_0 \epsilon \vec{E}$ the dielectric function of the free electron plasma:

$$\epsilon(\omega) = 1 - \frac{\omega_p^2}{\omega^2 + i\gamma\omega}. \tag{A.6}$$

If Maxwell's equations are used to construct a wave equation from electric field $\vec{E}$, dielectric displacement $\vec{D}$ and wave-vector $\vec{K}$ we can construct

$$\vec{\nabla} \times \vec{\nabla} \times \vec{E} = -\mu_0 \frac{\partial^2 \vec{D}}{\partial t^2} \tag{A.7}$$

and

$$\vec{K}(\vec{K} \cdot \vec{E}) - K^2 \vec{E} = -\epsilon(\vec{K}, \omega) \frac{\omega^2}{c^2} \vec{E}. \tag{A.8}$$

From these we can form the dispersion relationship for transverse and longitudinal waves. For transverse waves $\vec{K} \cdot \vec{E} = 0$ and so equation (A.8) becomes

$$K^2 = -\epsilon(\vec{K}, \omega) \frac{\omega^2}{c^2}. \tag{A.9}$$

For longitudinal waves, $\vec{K}(\vec{K} \cdot \vec{E}) = K^2 \vec{E}$ and so the dispersion relationship becomes

$$\epsilon(\vec{K}, \omega) = 0, \tag{A.10}$$

meaning longitudinal modes only occur when the complex dielectric constant is zero. If we consider the case where damping is negligible, which is valid for $\omega \sim \omega_p$ equation (A.6) becomes

$$\epsilon(\omega) = 1 - \frac{\omega_p^2}{\omega^2}, \tag{A.11}$$

which when used in equation (A.9) becomes

$$\omega^2 = \omega_p^2 + K^2 c^2. \tag{A.12}$$

From this dispersion relation we can see the only real solutions are $\omega > \omega_p$ and so transverse modes are only allowed to propagate above the plasma frequency. These modes are known as volume plasmon modes, as they occur in bulk and do not propagate on a boundary interface. From this understanding we can investigate the condition when $\omega < \omega_p$ on a metal-dielectric interface, known as surface propagating plasmons (SPPs). We can write equation (A.7), as

$$\vec{\nabla}(\vec{\nabla} \cdot \vec{E}) - \nabla^2 E = -\mu_0 \frac{\partial^2 \vec{D}}{\partial t^2} \tag{A.13}$$

by re-writing the curl product $\vec{\nabla} \times \vec{\nabla} \times \vec{E}$. The divergence $\vec{\nabla} \cdot \vec{E}$ can be written as

$$\vec{\nabla}(-\frac{1}{\epsilon}\vec{E} \cdot \vec{\nabla}\epsilon) - \nabla^2 E = -\mu_0 \epsilon_0 \epsilon \frac{\partial^2 \vec{E}}{\partial t^2} = -\frac{\epsilon}{c^2}\frac{\partial^2 \vec{E}}{\partial t^2}. \tag{A.14}$$

if the dielectric constant ϵ is the same within the region of one wavelength the divergent term can be discarded and simplifies to

$$\nabla^2 \vec{E} - \mu_0 \epsilon_0 \epsilon \frac{\partial^2 \vec{E}}{\partial t^2} = 0. \tag{A.15}$$

We obtain the Helmholtz wave equation by using the general solution $\vec{E}(x, y, z, t) = \vec{E}(x, y, z)e^{-i\omega t}$, giving

$$\nabla^2 \vec{E} + k_0^2 \epsilon \vec{E} = 0, \tag{A.16}$$

with the wave vector $k_0 = \epsilon\frac{\omega}{c}$. For an infinitely wide metal-dielectric interface we define ϵ as $\epsilon(z)$ so that the interface exists in the xy plane. This allows the incoming electric field $\vec{E}$ and magnetic field H to be split into z components with a propagation constant β in the non-z direction.

$$\vec{E}(x, y, z) = \vec{E}(z)e^{i\beta x}, \tag{A.17a}$$

$$\vec{H}(x, y, z) = \vec{H}(z)e^{i\beta x} \tag{A.17b}$$

The addition of the propagation constant changes the Helmholtz equation equation (A.18) to

$$\vec{E}(z) + (k_0^2 + \beta)\epsilon\vec{E}, = 0 \tag{A.18a}$$
$$\vec{H}(z) + (k_0^2 + \beta)\epsilon\vec{H}, = 0 \tag{A.18b}$$

From Maxwell's equations for a lack of external current source we can write

$$\vec{\nabla} \times \vec{E} = -\mu_0 \frac{\partial H}{\partial t} \tag{A.19a}$$
$$\vec{\nabla} \times \vec{H} = -\epsilon_0 \frac{\partial E}{\partial t}. \tag{A.19b}$$

We substitute in equation (A.17) into equation (A.19). If only considering propagation of β in the x direction and homogeneity in y in equation (A.17) leads to the curl components of equation (A.19) becoming

$$\frac{\partial E_y}{\partial z} = -i\omega\mu_0 H_x \tag{A.20a}$$
$$\frac{\partial E_x}{\partial z} - i\beta E_z = i\omega\mu_0 H_y \tag{A.20b}$$
$$i\beta E_y = i\omega\mu_0 H_z \tag{A.20c}$$
$$\frac{\partial H_x}{\partial z} - i\beta H_z = -i\omega\epsilon_0\epsilon E_y \tag{A.20d}$$
$$i\beta H_y = -i\omega\epsilon_0\epsilon E_z \tag{A.20e}$$

For the solutions of equation (A.21) we can consider the two orthogonal TM and TE modes. We define as TM modes $H_x = H_y = E_y = 0$ and for TE modes $E_x = E_z = H_y = 0$. For TM modes equation (A.21) becomes

$$E_x = -i\frac{1}{\omega\epsilon_0\epsilon}\frac{\partial H_y}{\partial z} \tag{A.21a}$$
$$E_x = -\frac{\beta}{\omega\epsilon_0\epsilon}H_y \tag{A.21b}$$

and the wave equation from equation (A.18) becomes

$$\frac{\partial H_y}{\partial z} + (k_0^2 + \beta)\epsilon E_y = 0. \tag{A.22}$$

Equation (A.21) and equation (A.22) are the equations that we can use to describe the propagation of TM modes at a metal boundary. A similar set of equations applies to TE modes, however it can be shown that TE modes do not support SPP modes in a metal interface. We define the metal interface $\epsilon(z)$ as a metal with ϵ_2 for $z < 0$ and a dielectric ϵ_1 for $z > 0$. By matching boundary conditions with equations equation (A.22) on either side of the boundary we can find the propagating wave solutions. Starting with a general solution in H_y for $z > 0$ and $z < 0$ leads to

$$H_y(z) = A_2 e^{i\beta x} e^{-k_2 z}, z > 0 \tag{A.23a}$$
$$H_y(z) = A_1 e^{i\beta x} e^{-k_1 z}, z < 0. \tag{A.23b}$$

Where A_1 and A_2 are the amplitudes to be matched and k_z are the components of the wave vector in the z direction. Using equation (A.23) in equation (A.21) leads to

$$E_x(z) = iA_2 \frac{k_2}{\omega\epsilon_0\epsilon_2} e^{i\beta x} e^{-k_2 z} \qquad z > 0 \tag{A.24a}$$
$$E_z(z) = -A_1 \frac{\beta}{\omega\epsilon_0\epsilon_2} e^{i\beta x} e^{-k_2 z} \qquad z > 0 \tag{A.24b}$$
$$E_x(z) = -iA_1 \frac{k_1}{\omega\epsilon_0\epsilon_1} e^{i\beta x} e^{-k_2 z} \qquad z < 0 \tag{A.24c}$$
$$E_z(z) = -A_1 \frac{\beta}{\omega\epsilon_0\epsilon_1} e^{i\beta x} e^{-k_2 z} \qquad z < 0 \tag{A.24d}$$

As a result of continuity $A_1 = A_2$ and

$$\frac{k_2}{k1} = -\frac{\epsilon_2}{\epsilon_1}. \tag{A.25}$$

From the wave equation in equation (A.22) the boundary condition on k becomes

$$k_1^2 = \beta^2 - k_0^2\epsilon_1 \tag{A.26a}$$
$$k_2^2 = \beta^2 - k_0^2\epsilon_2. \tag{A.26b}$$

Combining equations equation (A.25) and equation (A.26) gives the dispersion relation for surface plasmons propagating along the metal boundary,

$$\beta = k_0 \sqrt{\frac{\epsilon_1 \epsilon_2}{\epsilon_1 + \epsilon_2}}. \tag{A.27}$$

By replacing ϵ_1 with the ideal Drude dielectric function from equation (A.11) we can obtain the dispersion relationship with ω for an ideal metal

$$\beta = \frac{\omega}{c} \sqrt{\frac{\epsilon_2 (1 - \frac{\omega_p^2}{\omega^2})}{\epsilon_2 + 1 - \frac{\omega_p^2}{\omega^2}}}. \tag{A.28}$$

Appendix B

Source Code for 2D Diffusion Model

```
import numpy as np
import sys
import time
import scipy.io as sio

def Cyclic_ij(i,j,Nx,Ny):
    '''Gives the neighbouring points of i,j
        in a cyclic world of size Nx, Ny.
        Note: Can be replaced with np.roll'''
    jp1 = j + 1;     jm1 = j - 1
    ip1 = i + 1;     im1 = i - 1
    if j == Ny-1:    jp1 = 0;
    if j == 0:       jm1 = Ny-1;
    if i == Nx-1:    ip1 = 0;
    if i == 0:       im1 = Nx-1;
    return ip1, im1, jp1, jm1

def Psolve_fft(Ne, Nh, dx, L):
    '''Return electric field and potential
        from a cyclic charge distribution'''
    rho = Nh - Ne
    Mx = rho.shape[1]/2
    My = rho.shape[0]/2
    range_Mx = range(-Mx,Mx)
    range_My = range(-My,My)
    # Find Potential using FFTs
    RHO=np.fft.fft2(rho)
    for k1 in range_My:
        for k2 in range_Mx:
            if not (k1==0 and k2==0):
                RHO[k1,k2]= RHO[k1,k2]/(1.0*(k1*k1 + k2*k2))
    RHO[0,0]=0.0
    V= (1.0/(dx*4*np.pi**2)) * np.fft.ifft2(RHO).real

    # Find gradient of potential to get electric field,
    # Uses cyclic boundary conditions
    Ey = np.zeros(rho.shape)
    Ex = np.zeros(rho.shape)
```

```
    for (j,i) in np.ndindex(np.shape(rho)):
        ip1, im1, jp1, jm1 = Cyclic_ij(i, j, np.shape(rho)[1], np.shape(rho)[0])
        Ey[j,i] = L * ( V[jp1,i  ] - V[jm1  ,i  ]) / (2*dx)
        Ex[j,i] = L * ( V[j  ,ip1] - V[j    ,im1]) / (2*dx)
    return Ex, Ey, V

def diffuse_dNe_dNh(Ne, Nh, Ex, Ey, dx, Tr):
    '''Returns change in hole and electron densities'''
    range_Nx = np.arange(Ne.shape[1])
    range_Ny = np.arange(Ne.shape[0])
    Nx = Ne.shape[1]
    Ny = Ne.shape[0]
    dNe = np.zeros((Ny,Nx),float)
    dNh = np.zeros((Ny,Nx),float)
    for (j,i) in np.ndindex(np.shape(Ne)):
        ip1, im1, jp1, jm1 = Cyclic_ij(i, j, Nx, Ny)
        dNe[j,i] =(
                    ( Ne[jp1,i  ]*Ey[jp1, i   ]
                    - Ne[jm1,i  ]*Ey[jm1, i   ]
                    + Ne[j  ,ip1]*Ex[j,   ip1 ]
                    - Ne[j  ,im1]*Ex[j,   im1 ]) / (2*dx)

                    +(Ne[jp1,i  ]
                    + Ne[jm1,i  ]
                    + Ne[j  ,ip1]
                    + Ne[j  ,im1]
                    - 4*Ne[j,i]) / (dx*dx)

                    - (Ne[j,i]*Nh[j,i]) / Tr
                   )
        dNh[j,i] = - (Ne[j,i]*Nh[j,i]) / Tr
    return dNe, dNh

def gaussian(Ne, t, t_fwhm=1, t0=1):
    '''generate a 2D Gaussian function in time. Sums to one'''
    Nx = Ne.shape[1]
    Ny = Ne.shape[0]
    range_Nx = np.arange(Nx)
    range_Ny = np.arange(Ny)
    x0 = Nx / 2
    y0 = Ny / 2
    x, y = np.meshgrid(range_Nx, range_Ny)
    dNe = np.zeros((Ny,Nx),float)
    # get the variance  from the FWHM definition.
    wt = float(0.42466091*t_fwhm)
    # Make sure that the integral always sums to one
    a = (2.5066283 * wt)**(-1)
    dNe =  a * np.exp( -(((t-t0)**2)/(2*wt**2)))
    return dNe

def create_comb(resolution, width=1, depth=1, length=1):
    ''' Create initial triangular comb'''
    w = float(width*resolution)
    d = float(depth*resolution)
    x = float(length*resolution)
    Ny = int(w)
    Nx = int(2*d+x)
    Ne  = np.zeros((int(w),int(2*d+x)),float)
    for i in range(int(2*d+x)):
```

```
        for j in range(int(w)):
            if abs(j - w/2) < (x-i)*w/(2*x) or i > (d+x):
                Ne[j,i] = 1
    return Ne

def find_J(Ne, Nh, Ex, Ey, dx, Tr, n_0=1e20, mu=0.85, Temp=300):
    "Return current"
    k_b = 1.38e-23      # Boltzman Constant
    Nx = Ne.shape[1]
    Ny = Ne.shape[0]
    Jx = np.zeros((Ny,Nx),float)
    Jy = np.zeros((Ny,Nx),float)
    for (j,i) in np.ndindex(np.shape(Jx)):
        ip1, im1, jp1, jm1 = Cyclic_ij(i, j, Nx, Ny)
        Jy[j,i] = ( Ne[j  ,i  ] * Ey[j    ,i  ] +
                    (Ne[jp1,i  ] - Ne[jm1  ,i  ]) / (2*dx)
                  )
        Jx[j,i] = ( Ne[j  ,i  ] * Ex[j    ,i  ] +
                    (Ne[j  ,ip1] - Ne[j    ,im1]) / (2*dx)
                  )
    Jx = Jx * n_0 * mu * k_b * Temp
    Jy = Jy * n_0 * mu * k_b * Temp
    return Jx, Jy

def Main(size,X,resolution):
    start_Time = time.time()
    max_time = 1e-10    # Simulated time in s
    Temp= 300           # Temperature in K
    k_b = 1.38e-23      # Boltzman Constant
    e   = 1.60e-19      # electronic charge constant
    e_0 = 8.85e-12      # Free space permittivity
    n_0 = 1e20          # Initial carrier density
    t_r = 1e-12         # Recombination time in s
    mu  = 0.85          # Mobility in m^2 V^-1 s^-1
    pulse_fwhm = 1e-13  # Pulse FWHM in seconds

    # Debye Length L
    L   = np.sqrt((e_0 * k_b * Temp)/(e**2 * n_0))
    # Dimensionless time T_scale
    T_scale =  e_0 / (e * n_0 * mu)
    # Dimensionless recombination time Tr
    Tr = t_r / T_scale
    pulse_fwhm = pulse_fwhm/T_scale

     # Scale simulation
    size_L  = size / L
    dx      = size_L / resolution
    dt = 1e-2 * Tr
    max_i = max_time / (dt*T_scale)
    N = resolution
    print 'L    =', L, 'm'
    print 'T_scale  = ', T_scale
    print 'Dimensionless Recombination Time  = ', Tr
    print 'Dimensionless Time Step  = ', dt
    print 'time step    =', dt*T_scale, 's'

    comb = create_comb(resolution, width=1, depth=1, length=X)
    Nx = comb.shape[1]
    Ny = comb.shape[0]
```

```
J_sum_x = []
J_sum_y = []
timeList = np.arange(0, dt*max_i, dt, float)
# Initialise arrays
Ne  = np.zeros((Ny,Nx, max_i))
Nh  = np.zeros((Ny,Nx, max_i))
dNe = np.zeros((Ny,Nx, max_i))
dNh = np.zeros((Ny,Nx, max_i))
Ex  = np.zeros((Ny,Nx, max_i))
Ey  = np.zeros((Ny,Nx, max_i))
V   = np.zeros((Ny,Nx, max_i))
Jx  = np.zeros((Ny,Nx, max_i))
Jy  = np.zeros((Ny,Nx, max_i))
i = 0
while i < max_i -1:
    # Find electric field
   Ex[:,:,i+1], Ey[:,:,i+1], V[:,:,i+1] = Psolve_fft(
                                          Ne[:,:,i],
                                          Nh[:,:,i],
                                          dx, L)
    # Change in carrier density from diffusion
    dNe[:,:,i+1], dNh[:,:,i+1] = diffuse_dNe_dNh(
                                    Ne[:,:,i],
                                    Nh[:,:,i],
                                    Ex[:,:,i], Ey[:,:,i],
                                    dx,Tr)
    # Change from optical generation
    dNe[:,:,i+1] = (dNe[:,:,i+1]
                    + comb*gaussian( comb, timeList[i],
                                     t_fwhm=pulse_fwhm,
                                     t0=2*pulse_fwhm))
    dNh[:,:,i+1] = (dNe[:,:,i+1]
                    + comb*gaussian( comb, timeList[i],
                                     t_fwhm=pulse_fwhm,
                                     t0=2*pulse_fwhm))
    # Update carrier densities
    Ne[:,:,i+1] = Ne[:,:,i] + (dNe[:,:,i+1] *dt)
    Nh[:,:,i+1] = Nh[:,:,i] + (dNh[:,:,i+1] *dt)
    Jx[:,:,i+1], Jy[:,:,i+1] = find_J(
                                  Ne[:,:,i],
                                  Nh[:,:,i],
                                  Ex[:,:,i], Ey[:,:,i],
                                  dx, Tr, n_0, mu, Temp)
    i = i + 1
    # Monitor progress every 10 simulation steps
    if i % 10 == 0:
        sys.stdout.write("\r%d" % ((i/max_i)*100)+ "% Done")
        sys.stdout.flush()

end_Time = time.time()
print 'Time taken %.5g' % (end_Time - start_Time), 's'
sio.savemat('E.mat', {'Jx':Jx,
                      'Jy':Jy,
                      'Ex':Ex,
                      'Ey':Ey,
                      'V':V,
                      'Ne':Ne,
                      'Nh':Nh,
                      'dNe':dNe,
```

```
                              'dNh':dNh,
                              'time': timeList,
                              'dx': dx,
                              'dt': dt,
                              'J_sum_y': J_sum_y,
                              'J_sum_x': J_sum_x,
                              'T_scale': T_scale,
                              'L': L },
            do_compression=True)

resolution = 20
size  = 1e-6
x =1

Main(size,x,resolution)
```

Bibliography

[1] Duncan McBryde, Mark E. Barnes, Sam A. Berry, Paul C. Gow, Harvey E. Beere, David A. Ritchie, and Vasilis Apostolopoulos. "Fluence and polarisation dependence of GaAs based Lateral Photo-Dember terahertz emitters". In: 22.3 (2014), pp. 3234–3243 (cit. on pp. xix, 63, 70, 72, 75, 97, 98).

[2] Mark E. Barnes, Sam A. Berry, Paul C. Gow, Duncan McBryde, Geoff J. Daniell, Harvey E. Beere, David A. Ritchie, and Vasilis Apostolopoulos. "Investigation of the role of the lateral photo-Dember effect in the generation of terahertz radiation using a metallic mask on a semiconductor". In: *Optics Express* 21.14 (2013), pp. 16263–16272 (cit. on pp. xix, 12, 15, 20, 69, 70).

[3] Mark E. Barnes, Duncan McBryde, Geoff J. Daniell, G. Whitworth, Aaron L. Chung, Adrian H. Quarterman, Keith G. Wilcox, A. Brewer, Harvey E. Beere, David A. Ritchie, and Vasilis Apostolopoulos. "Terahertz emission by diffusion of carriers and metal-mask dipole inhibition of radiation." In: *Optics Express* 20.8 (2012), pp. 8898–8906 (cit. on pp. xix, 12, 15, 20, 35, 64, 70, 97).

[4] Mark E. Barnes, Duncan McBryde, Sam A. Berry, Paul C. Gow, Geoff J. Daniell, Harvey E. Beere, David A. Ritchie, and Vasilis Apostolopoulos. "Terahertz emission from lateral surge currents and suppression of dipoles under a metal mask". In: *2013 38th International Conference on Infrared, Millimeter, and Terahertz Waves (IRMMW-THz)*. IEEE, 2013, pp. 1–2 (cit. on p. xix).

[5] Mark E. Barnes, Duncan McBryde, Paul C. Gow, Sam A. Berry, Geoff J. Daniell, Harvey E. Beere, David A. Ritchie, and Vasilis Apostolopoulos. "Investigation into the role of the metal mask and pump laser illumination parameters for lateral photo-Dember emitters". In: *2013 38th International Conference on Infrared, Millimeter, and Terahertz Waves (IRMMW-THz)*. IEEE, 2013, pp. 1–2 (cit. on p. xix).

[6] Duncan McBryde, Paul C. Gow, Sam A. Berry, Mark E. Barnes, Armen Aghajani, and Vasilis Apostolopoulos. "Multiple double-metal bias-free terahertz emitters". In: *Applied Physics Letters* 104.20 (2014), p. 201108 (cit. on pp. xix, 81).

[7] Duncan McBryde, Mark E. Barnes, Paul C. Gow, Sam A. Berry, Geoff J. Daniell, Harvey E. Beere, David A. Ritchie, and Vasilis Apostolopoulos. "Characterisation of low temperature and semi-insulating GaAs lateral photo-dember THz emitters". In: *2013 38th International Conference on Infrared, Millimeter, and Terahertz Waves (IRMMW-THz)*. IEEE, 2013, pp. 1–2 (cit. on p. xix).

[8] Paul C. Gow, Sam A. Berry, Duncan McBryde, Mark E. Barnes, Harvey E. Beere, David A. Ritchie, and Vasilis Apostolopoulos. "Multiple lateral photo-Dember terahertz emitters illuminated by a cylindrical micro-lens array". In: *Applied Physics Letters* 103.25 (2013), p. 252101 (cit. on pp. xix, 71, 81, 98).

[9] Duncan McBryde, Mark E. Barnes, Aaron L. Chung, Zakaria Mihoubi, Geoff J. Daniell, Adrian H. Quarterman, Keith G. Wilcox, Harvey E. Beere, David A. Ritchie, Anne C. Tropper, and Vasilis Apostolopoulos. "Simulation of metallic nanostructures for emission of THz radiation using the lateral photo-Dember effect". In: *IRMMW-THz 2011*. Houston, Texas: IEEE, 2011, pp. 1–2 (cit. on pp. xix, 19, 97).

[10] Charles A. Schmuttenmaer. "Exploring dynamics in the far-infrared with terahertz spectroscopy". In: *Chemical Reviews* 104 (2004), pp. 1759–1779 (cit. on p. 1).

[11] Masayoshi Tonouchi. "Cutting-edge terahertz technology". In: *Nature Photonics* 1.2 (2007), pp. 97–105 (cit. on p. 1).

[12] Naoto Nagai, Ryoichi Kumazawa, and Ryoichi Fukasawa. "Direct evidence of inter-molecular vibrations by THz spectroscopy". In: *Chemical Physics Letters* 413.4-6 (2005), pp. 495–500 (cit. on p. 1).

[13] John F. Federici, Brian Schulkin, Feng Huang, Dale Gary, Robert Barat, Filipe Oliveira, and David Zimdars. "THz imaging and sensing for security application-sexplosives, weapons and drugs". In: *Semiconductor Science and Technology* 20.7 (2005), S266–S280 (cit. on pp. 1, 5).

[14] Peter U. Jepsen, D. G. Cooke, and M. Koch. "Terahertz spectroscopy and imaging - Modern techniques and applications". In: *Laser & Photon. Rev.* 5.1 (2011), pp. 124–166 (cit. on p. 1).

[15] Hai-Bo Liu, Yunqing Chen, Glenn J. Bastiaans, and X.-C. Zhang. "Detection and identification of explosive RDX by THz diffuse reflection spectroscopy". In: *Optics Express* 14.1 (2006), p. 415 (cit. on pp. 1, 5).

[16] T.G. G. Phillips and J. Keene. "Submillimeter astronomy [heterodyne spectroscopy]". In: *Proceedings of the IEEE* 80.11 (1992), pp. 1662–1678 (cit. on p. 1).

[17] A. G. Davies, Edmund H. Linfield, and Michael B. Johnston. "The development of terahertz sources and their applications." In: *Physics in Medicine and Biology* 47.47 (2002), pp. 3679–3689 (cit. on p. 1).

[18] Frank Schwierz. "The frequency limits of field-effect transistors: MOSFET vs. HEMT". In: *International Conference on Solid-State and Integrated Circuits Technology Proceedings, ICSICT* (2008), pp. 1433–1436 (cit. on p. 1).

[19] E Borie. *Review of gyrotron theory*. August. Insitut fur Technische Physik, 1991 (cit. on p. 2).

[20] David H Auston. "Picosecond optoelectronic switching and gating in silicon". In: *Applied Physics Letters* 26.3 (1975), pp. 101–103 (cit. on p. 2).

[21] Chi H Lee. "Picosecond optoelectronic switching in GaAs". In: *Applied Physics Letters* 30.2 (1977), p. 84 (cit. on p. 2).

[22] Gerard A. Mourou, C. V. Stancampiano, A. Antonetti, and A. Orszag. "Picosecond microwave pulses generated with a subpicosecond laser-driven semiconductor switch". In: *Applied Physics Letters* 39.4 (1981), pp. 295–296 (cit. on p. 2).

[23] Gerard Mourou, Charles V. Stancampiano, and Daniel Blumenthal. "Picosecond microwave pulse generation". In: *Applied Physics Letters* 38.6 (1981), pp. 470–472 (cit. on p. 2).

[24] David H. Auston, K. P. Cheung, and P. R. Smith. *Picosecond photoconducting Hertzian dipoles*. 1984 (cit. on p. 2).

[25] David H. Auston, K.P. Cheung, and D.A. Kleinman. "Cherenkov Radiation from Femtosecond Optical Pulses in Electro-Optic Meida". In: *Physical Review Letters* 53.16 (1984), pp. 1555–1558 (cit. on p. 2).

[26] David H. Auston and K.P. Cheung. "Coherent time-domain far-infrared spectroscopy". In: *Journal of the Optical Society of America B* 2.4 (1985), pp. 606–612 (cit. on p. 2).

[27] Alfred P. DeFonzo, Maduri Jarwala, and Charles Lutz. "Transient response of planar integrated optoelectronic antennas". In: *Applied Physics Letters* 50.17 (1987), p. 1155 (cit. on p. 2).

[28] Alfred P. DeFonzo and Charles Lutz. "Optoelectronic transmission and reception of ultrashort electrical pulses". In: *Applied Physics Letters* 51.4 (1987), p. 212 (cit. on p. 2).

[29] P. R. Smith, David H. Auston, and Martin C Nuss. "Subpicosecond photoconducting dipole antennas". In: *IEEE Journal of Quantum Electronics* 24.2 (1988), pp. 255–260 (cit. on p. 2).

[30] Ch. Fattinger and D. Grischkowsky. "Terahertz beams". In: *Applied Physics Letters* 54.6 (1989), pp. 490–492 (cit. on p. 2).

[31] Ch. Fattinger and D. Grischkowsky. "Point source terahertz optics". In: *Applied Physics Letters* 53.16 (1988), pp. 1480–1482 (cit. on p. 2).

[32] D. Grischkowsky, Søren Keiding, Martin van Exter, and Ch. Fattinger. "Far-infrared time-domain spectroscopy with terahertz beams of dielectrics and semiconductors". In: *Journal of the Optical Society of America B* 7.10 (1990), pp. 2006–2015 (cit. on p. 3).

[33] Peter U. Jepsen, R. H. Jacobsen, and Søren Keiding. "Generation and detection of terahertz pulses from biased semiconductor antennas". In: *Journal of the Optical Society of America B* 13.11 (1996), p. 2424 (cit. on p. 4).

[34] Daniel M. Mittleman, R. H. Jacobsen, and Martin C Nuss. "T-Ray Imagaing". In: *IEE Journal of Selected Topics In Quantum Electronics* 2 (1996), p. 3 (cit. on p. 4).

[35] P.F. Taday, I.V. Bradley, D.D. Arnone, and M. Pepper. "Using terahertz pulse spectroscopy to study the cryastalline structure of a drug: A case study of the polymorphs of ranitidine hydrochloride". In: *Journal of Pharmaceuticals Science* 92.4 (2003), pp. 831–838 (cit. on p. 5).

[36] Aaron L. Chung. "Material Parameter Extraction in Terahertz Time Domain Spectroscopy". PhD thesis. University of Southampton, 2012 (cit. on p. 5).

[37] Kaori Fukunaga, Iwao Hosako, Marcello Picollo, and Yohsei Kohdzuma. "Application of THz Sensing to Analysis of Works of Art for Conservation". In: *Microwave Photonics (MWP), 2010 IEEE Topical Meeting on*. 2010, pp. 147–150 (cit. on p. 5).

[38] D. Pinna, M. Galeotti, and R. Mazzeo. *Scientific Examination for the Investigation of Paintings: A Handbook for Conservator-Restorers*. Centro Di, Firenze, 2009 (cit. on p. 5).

[39] Callum J. Docherty, Patrick Parkinson, Hannah J. Joyce, Ming-Hui Chiu, Chang-Hsiao Chen, Ming-Yang Lee, Lain-Jong Li, Laura M. Herz, and Michael B. Johnston. "Ultrafast Transient Terahertz Conductivity of Monolayer MoS 2 and WSe 2 Grown by Chemical Vapor Deposition". In: *ACS Nano* 8.11 (2014), pp. 11147–11153 (cit. on p. 5).

[40] Hannah J. Joyce, Patrick Parkinson, Nian Jiang, Callum J. Docherty, Qiang Gao, H. H. Tan, Chennupati Jagadish, Laura M. Herz, and Michael B. Johnston. "Electron mobilities approaching bulk limits in "surface-free" GaAs nanowires." In: *Nano letters* 14.10 (2014), pp. 5989–94 (cit. on p. 5).

[41] Vasilis Apostolopoulos, Geoff J. Daniell, and Aaron L. Chung. "Complex Refractive Index Determination Using Planar and Converging Beam Transfer Functions". In: *Terahertz Spectroscopy and Imaging*. Springer, 2013, pp. 81–94 (cit. on p. 5).

[42] Timothy D. Dorney, Richard G. Baraniuk, and Daniel M. Mittleman. "Material Parameter Estimation and Imaging with Terahertz Time-Domain Spectroscopy". PhD thesis. 2001, p. 1562 (cit. on p. 5).

[43] H Dember. "Über eine photoelektronische Kraft in Kupferoxydul-Kristallen". In: *Physikalische Zeitschrift* 32 (1931), p. 554 (cit. on p. 5).

[44] Matthew C. Beard, Gordon M. Turner, and Charles A. Schmuttenmaer. "Subpicosecond carrier dynamics in low-temperature grown GaAs as measured by time-resolved terahertz spectroscopy". In: *Journal of Applied Physics* 90.12 (2001), p. 5915 (cit. on p. 6).

[45] T. Dekorsy, H. Auer, H. Bakker, H. G. Roskos, and H. Kurz. "THz electromagnetic emission by coherent infrared-active phonons." In: *Physical review. B, Condensed matter* 53.7 (1996), pp. 4005–4014 (cit. on p. 6).

[46] Nobuhiko Sarukura, Hideyuki Ohtake, Shinji Izumida, and Zhenlin Liu. "High average-power THz radiation from femtosecond laser-irradiated InAs in a magnetic field and its elliptical polarization characteristics". In: *Journal of Applied Physics* 84.1 (1998), p. 654 (cit. on p. 6).

[47] Michael B. Johnston, D. M. Whittaker, A. Corchia, A. G. Davies, and Edmund H Linfield. "Theory of magnetic-field enhancement of surface-field terahertz emission". In: *Journal of Applied Physics* 91.4 (2002), p. 2104 (cit. on p. 6).

[48] R. Kersting, Karl Unterrainer, G. Strasser, H.˜F. Kauffmann, and E. Gornik. "Few-Cycle THz Emission from Cold Plasma Oscillations". In: *Physical Review Letters* 79.16 (1997), pp. 3038–3041 (cit. on p. 6).

[49] X.-C. Zhang, Bin Bin Hu, J. T. Darrow, and David H. Auston. "Generation of femtosecond electromagnetic pulses from semiconductor surfaces". In: *Applied Physics Letters* 56.11 (1990), p. 1011 (cit. on pp. 7, 72).

[50] J Bardeen. "Surface States and Rectification at a Metal Semi-Conductor Contact". In: *Physical Review* 71.10 (1947), pp. 717–727 (cit. on pp. 7, 72).

[51] Peter Y. Yu and Manuel Cardona. *Fundamentals of Semiconductors Physics and Materials Properties*. 3rd ed. Springer, 2005 (cit. on p. 7).

[52] Michael B. Johnston, D. M. Whittaker, A. Corchia, A. G. Davies, and Edmund H. Linfield. "Simulation of terahertz generation at semiconductor surfaces". In: *Physical Review B* 65.16 (2002), pp. 165301–8 (cit. on p. 7).

[53] Gregor Klatt, F. Hilser, W. Qiao, Mattias Beck, R Gebs, A. Bartels, K. Huska, U. Lemmer, Georg Bastian, Michael B. Johnston, M. Fischer, Jérôme Faist, and T. Dekorsy. "Terahertz emission from lateral photo-Dember currents." In: *Optics Express* 18.5 (2010), pp. 4939–47 (cit. on pp. 8, 19, 63, 64, 70, 81).

[54] Gregor Klatt, B. Surrer, D. Stephan, O. Schubert, M. Fischer, Jérôme Faist, A. Leitenstorfer, R. Huber, and T. Dekorsy. "Photo-Dember terahertz emitter excited with an Er:fiber laser". In: *Applied Physics Letters* 98.2 (2011), p. 021114 (cit. on pp. 8, 13, 14, 64, 65).

[55] K.H Drexhage. "Influence of a dielectric interface on fluorescence decay time". In: *Journal of Luminescence* 1,2 (1970), pp. 693–701 (cit. on pp. 13, 71).

[56] M. Walther, D. G. Cooke, C. Sherstan, M. Hajar, M. R. Freeman, and F. a. Hegmann. "Terahertz conductivity of thin gold films at the metal-insulator percolation transition". In: *Physical Review B - Condensed Matter and Materials Physics* 76.12 (2007), pp. 1–9 (cit. on p. 15).

[57] Mark A. Ordal, Robert J. Bell, Ralph W. Alexander, Larry L. Long, and Marvin R. Querry. "Optical properties of fourteen metals in the infrared and far infrared: Al, Co, Cu, Au, Fe, Pb, Mo, Ni, Pd, Pt, Ag, Ti, V, and W." In: *Applied Optics* 24.24 (1985), p. 4493 (cit. on p. 15).

[58] Syed B. Qadri, Dong H. Wu, Benjamin D. Graber, Nadeemullah a. Mahadik, and Anthony Garzarella. "Failure mechanism of THz GaAs photoconductive antenna". In: *Applied Physics Letters* 101.1 (2012), p. 011910 (cit. on pp. 15, 16, 41).

[59] Stephan Winnerl. "Scalable Microstructured Photoconductive Terahertz Emitters". In: *Journal of Infrared, Millimeter, and Terahertz Waves* 33.4 (2011), pp. 431–454 (cit. on pp. 17, 63).

[60] Kanglin Wang and Daniel M. Mittleman. "Metal wires for terahertz wave guiding". In: *Nature* 432 (2004) (cit. on p. 17).

[61] Mark E. Barnes. "Terahertz emission from ultrafast lateral diffusion currents within semiconductor devices". PhD thesis. University of Southampton, 2014 (cit. on pp. 20, 37).

[62] Kai Liu, J.Z. Xu, Tao Yuan, and X.-C. Zhang. "Terahertz radiation from InAs induced by carrier diffusion and drift". In: *Physical Review B* 73.15 (2006), p. 155330 (cit. on p. 23).

[63] T. Dekorsy, T. Pfeifer, W. Kütt, H. Kurz, W. Kutt, and H. Kurz. "Subpicosecond carrier transport in GaAs surface-space-charge fields". In: *Physical Review B* 47.7 (1993), pp. 3842–3849 (cit. on pp. 23, 26).

[64] Martin Eden Glicksman. *Diffusion in solids*. 1st ed. New York, NY: Wiley, 2000, p. 472 (cit. on p. 23).

[65] Shantanu Gupta, John F. Whitaker, and Gerard A Mourou. "Ultrafast Carrier Dynamics in 111-V Semiconductors Grown by Molecular-Beam Epitaxy at Very Low Substrate Temperatures". In: 28.October (1992) (cit. on p. 39).

[66] Ian S. Gregory. "The development of a continuous-wave terahertz imaging system". PhD thesis. University of Cambridge, 2004 (cit. on pp. 39, 44, 66).

[67] J. S. Blakemore. "Semiconducting and other major properties of gallium arsenide". In: *Journal of Applied Physics* 53.10 (1982), R123 (cit. on p. 39).

[68] Shantanu Gupta, M. Y. Frankel, J. A. Valdmanis, John F. Whitaker, Gerard A. Mourou, F. W. Smith, and A. R. Calawa. "Subpicosecond carrier lifetime in GaAs grown by molecular beam epitaxy at low temperatures". In: *Applied Physics Letters* 59.25 (1991), p. 3276 (cit. on pp. 39, 40).

[69] F. W. Smith, A. R. Calawa, C.-L. Chen, M.J. Manfra, and L.J. Mahoney. "New MBE buffer used to eliminate backgating in GaAs MESFETs". In: *Electron Device Letters, IEEE* 9.2 (1988), p. 77 (cit. on p. 39).

[70] P. Grenier and John F. Whitaker. "Subband gap carrier dynamics in low-temperature-grown GaAs". In: *Applied Physics Letters* 70.15 (1997), p. 1998 (cit. on pp. 39, 40).

[71] Masahiko Tani, Kohji Yamamoto, Elmer S. Estacio, Christopher T. Que, Hidekazu Nakajima, Masakazu Hibi, Fumiaki Miyamaru, Seizi Nishizawa, and Masanori Hangyo. "Photoconductive Emission and Detection of Terahertz Pulsed Radiation Using Semiconductors and Semiconductor Devices". In: *Journal of Infrared, Millimeter, and Terahertz Waves* 33 (2012), pp. 393–404 (cit. on p. 39).

[72] Masahiko Tani, S. Matsuura, Kiyomi Sakai, and S. Nakashima. "Emission characteristics of photoconductive antennas based on low-temperature-grown GaAs and semi-insulating GaAs." In: *Applied Optics* 36.30 (1997), pp. 7853–7859 (cit. on pp. 40, 41).

[73] S.G. Park, M. R. Melloch, and A.M. Weiner. "Analysis of terahertz waveforms measured by photoconductive and electrooptic sampling". In: *IEEE Journal of Quantum Electronics* 35.5 (1999), pp. 810–819 (cit. on p. 40).

[74] A. Kurpiewski, K. Korona, and M. Kamiska. "Electrical and Optical Properties of Highly Non-stoichiometric GaAs". In: *Acta Physica Polonica A* 87.2 (1995), pp. 518–522 (cit. on p. 40).

[75] S. U. Dankowski, D. Streb, M. Ruff, Peter Kiesel, M. Kneissl, B. Knupfer, and G. H. Dohler. "Above band gap absorption spectra of the arsenic antisite defect in low temperature grown GaAs and AlGaAs". In: *American Institute of Physics* 68.January (1996), pp. 37–39 (cit. on p. 40).

[76] Andreas Othonos. "Probing ultrafast carrier and phonon dynamics in semiconductors". en. In: *Journal of Applied Physics* 83.4 (1998), p. 1789 (cit. on pp. 40, 41).

[77] J. K. Luo, H. Thomas, D. V. Morgan, and D. Westwood. "Transport properties of GaAs layers grown by molecular beam epitaxy at low temperature and the effects of annealing". In: *Journal of Applied Physics* 79.7 (1996), p. 3622 (cit. on p. 41).

[78] S. Fleischer, C. D. Beling, S. Fung, W. R. Nieveen, J. E. Squire, J. Q. Zheng, and Mohamed Missous. "Structural and defect characterization of GaAs and AlGaAs grown at low temperature by molecular beam epitaxy". In: *Journal of Applied Physics* 81.1 (1997), p. 190 (cit. on p. 41).

[79] Ian S. Gregory, Colin Baker, W. R. Tribe, M. J. Evans, Harvey E. Beere, Edmund H. Linfield, A. G. Davies, and Mohamed Missous. "High resistivity annealed low-temperature GaAs with 100 fs lifetimes". In: *Applied Physics Letters* 83.20 (2003), p. 4199 (cit. on p. 41).

[80] R. J. B. Dietz, R. Wilk, B. Globisch, H. G. Roskos, D. Stanze, S. Ullrich, S. Schumann, N. Born, M. Koch, B. Sartorius, and Michael Schall. "Low Temperature Grown Be-doped InGaAs/InAlAs Photoconductive Antennas Excited at 1030nm". In: *Journal of Infrared, Millimeter, and Terahertz Waves* 34.3-4 (2013), pp. 231–237 (cit. on p. 41).

[81] T. S. Sosnowski, T. B. Norris, H. H. Wang, P. Grenier, John F. Whitaker, and C. Y. Sung. "High-carrier-density electron dynamics in low-temperature-grown GaAs". In: *Applied Physics Letters* 70.24 (1997), p. 3245 (cit. on p. 46).

[82] P. G. Huggard, C. J. Shaw, J. A. Cluff, and S. R. Andrews. "Polarization-dependent efficiency of photoconducting THz transmitters and receivers". In: *Applied Physics Letters* 72.17 (1998), p. 2069 (cit. on pp. 55, 70).

[83] Wiebe G. Heitman and P. M. van den Berg. "Diffraction of Electromagnetic Waves by a Semi-Infinite Screen in a Layered Medium". In: *Canadian Journal of Physics* 53.14 (1975), pp. 1305–1317 (cit. on p. 55).

[84] Stephen E. Ralph and D. Grischkowsky. "Trap-enhanced electric fields in semi-insulators: The role of electrical and optical carrier injection". In: *Applied Physics Letters* 59.16 (1991), p. 1972 (cit. on p. 55).

[85] Dae Sin Kim and D. S. Citrin. "Efficient terahertz generation using trap-enhanced fields in semi-insulating photoconductors by spatially broadened excitation". In: *Journal of Applied Physics* 101.5 (2007), p. 053105 (cit. on p. 55).

[86] Y. Jin, X. F. Ma, G. A. Wagoner, M. Alexander, and X.-C. Zhang. "Anomalous optically generated THz beams from metal/GaAs interfaces". In: *Applied Physics Letters* 65.6 (1994), p. 682 (cit. on p. 56).

[87] M. Li, F. G. Sun, G. A. Wagoner, M. Alexander, and X.-C. Zhang. "Measurement and analysis of terahertz radiation from bulk semiconductors". In: *Applied Physics Letters* 67.1 (1995), p. 25 (cit. on pp. 56, 58).

[88] Yulei Shi, Yuping Yang, Xinlong Xu, Shihua Ma, Wei Yan, and Li Wang. "Ultrafast carrier dynamics in AuGaAs interfaces studied by terahertz emission spectroscopy". In: *Applied Physics Letters* 88.16 (2006), p. 161109 (cit. on pp. 56, 58, 72, 75).

[89] Emlyn Huw Rhoderick. *Metal-Semiconductor Contacts*. 1st ed. Oxford University Press, 1978 (cit. on pp. 58, 81).

[90] G. Matthäus, S. Nolte, R. Hohmuth, M. Voitsch, W. Richter, B. Pradarutti, S. Riehemann, G. Notni, and a. Tünnermann. "Large-area microlens emitters for powerful THz emission". In: *Applied Physics B* 96.2-3 (2009), pp. 233–235 (cit. on p. 63).

[91] Ranjan Singh, Eric Plum, Christoph Menzel, Carsten Rockstuhl, Nikolay I. Zheludev, and Weili Zhang. "Negative index in chiral metamaterials". In: *IEEE Photonic Society 24th Annual Meeting, PHO 2011* 9.7 (2011), pp. 240–241 (cit. on p. 63).

[92] Batop Electronics. *Instruction manual and data sheet iPCA-21-05-300-800-h* (cit. on p. 63).

[93] N. Laman and D. Grischkowsky. "Terahertz conductivity of thin metal films". In: *Applied Physics Letters* 93 (2008), pp. 1–3 (cit. on p. 64).

[94] Ian S. Gregory, W. R. Tribe, Colin Baker, B.E. Cole, M. J. Evans, L. Spencer, M. Pepper, and Mohamed Missous. "Continuous-wave terahertz system with a 60 dB dynamic range". In: *Applied Physics Letters* 86.20 (2005), p. 204104 (cit. on p. 66).

[95] Colin Baker. "Development of Semiconductor Materials for Terahertz Photoconductive Antennas". PhD thesis. University of Cambridge, 2004 (cit. on p. 66).

[96] Elmer S. Estacio, Masakazu Hibi, Katsuya Saito, Christopher T. Que, Takashi Furuya, Fumiaki Miyamaru, Seizi Nishizawa, Kohji Yamamoto, and Masahiko Tani. "Saturation and Polarization Characteristics of 1.56μm Optical Probe Pulses in a LTG-GaAs Photoconductive Antenna Terahertz Detector". In: *Journal of Infrared, Millimeter, and Terahertz Waves* (2013) (cit. on p. 70).

[97] Mark A. Ordal, Robert J. Bell, Ralph W. Alexander, Lawrence A. Newquist, and Marvin R. Querry. "Optical properties of Al, Fe, Ti, Ta, W, and Mo at submillimeter wavelengths". In: *Applied Optics* 27.6 (1988), pp. 1203–9 (cit. on p. 71).

[98] Ranjan Singh, Evgenya Smirnova, Antoinette J. Taylor, John F. O'Hara, and Weili Zhang. "Optically thin terahertz metamaterials." In: *Optics Express* 16.9 (2008), pp. 6537–43 (cit. on p. 71).

[99] Tomonori Nishimura, Koji Kita, and Akira Toriumi. "A Significant Shift of Schottky Barrier Heights at Strongly Pinned Metal/Germanium Interface by Inserting an Ultra-Thin Insulating Film". In: *Applied Physics Express* 1 (2008), p. 051406 (cit. on p. 72).

[100] C. A. Mead and W. G. Spitzer. "Fermi level position at metal-semiconductor interfaces". In: *Physical Review* 143 (1964), A713 (cit. on p. 72).

[101] W. G. Spitzer and C. A. Mead. "Barrier Height Studies on Metal-Semiconductor Systems". In: *Journal of Applied Physics* 34.10 (1963), p. 3061 (cit. on p. 72).

[102] J. R. Waldrop. "Schottky-barrier height of ideal metal contacts to GaAs". In: *Applied Physics Letters* 44.10 (1984), p. 1002 (cit. on p. 73).

[103] C. M. Wolfe. "Electron Mobility in High-Purity GaAs". In: *Journal of Applied Physics* 41.7 (1970), p. 3088 (cit. on p. 76).

[104] P. Hudait M.K.and Venkateswarlu and S.B Krupanidhi. "Electrical transport characteristics of Au/n-GaAs Schottky diodes on n-Ge at low temperatures". In: *Solid-State Electronics* 45.1 (2001), pp. 133–141 (cit. on p. 76).

[105] T. W. Ebbesen, H. J. Lezec, H. F. Ghaemi, Tineke Thio, and P. A. Wolff. "Extraordinary optical transmission through sub-wavelength hole arrays". In: *Nature* 391.February (1998), pp. 667–669. arXiv: `0008204 [cond-mat]` (cit. on p. 81).

[106] L. Martín-Moreno, F. J. García-Vidal, H. J. Lezec, K. M. Pellerin, Tineke Thio, J. B. Pendry, and T. W. Ebbesen. "Theory of extraordinary optical transmission through subwavelength hole arrays". In: *Physical Review Letters* 86 (2001), pp. 1114–1117. arXiv: `0008204 [cond-mat]` (cit. on p. 82).

[107] H. A. Bethe. "Theory of diffraction by small holes". In: *Physical Review* 66.7-8 (1944), pp. 163–182 (cit. on pp. 82, 85).

[108] Abhishek Singh and S. S. Prabhu. "Microlensless interdigitated photoconductive terahertz emitters". In: *Optics Express* 23.2 (2015), pp. 1972–1974 (cit. on p. 82).

[109] Bing-Yu Hsieh and Mona Jarrahi. "Analysis of periodic metallic nano-slits for efficient interaction of terahertz and optical waves at nano-scale dimensions". In: *Journal of Applied Physics* 109.8 (2011), p. 084326 (cit. on pp. 83, 93).

[110] Barmak Heshmat, Hamid Pahlevaninezhad, Yuanjie Pang, Mostafa Masnadi-Shirazi, Ryan Burton Lewis, Thomas Tiedje, Reuven Gordon, and Thomas Edward Darcie. "Nanoplasmonic terahertz photoconductive switch on GaAs". In: *Nano Letters* 12.12 (2012), pp. 6255–6259 (cit. on pp. 83, 93).

[111] Sang-Gil Park, Kyong Hwan Jin, Minwoo Yi, Jong Chul Ye, Jaewook Ahn, and Ki-Hun Jeong. "Enhancement of terahertz pulse emission by optical nanoantenna." In: *ACS nano* 6.3 (2012), pp. 2026–31 (cit. on pp. 83, 84, 93).

[112] Christopher W. Berry, N. Wang, Mohammad R. Hashemi, M Unlu, and Mona Jarrahi. "Significant performance enhancement in photoconductive terahertz optoelectronics by incorporating plasmonic contact electrodes." In: *Nature Communications* 4.1 (2013), p. 1622 (cit. on pp. 83, 93).

[113] Christopher W. Berry, Mohammad R. Hashemi, and Mona Jarrahi. "Generation of high power pulsed terahertz radiation using a plasmonic photoconductive emitter array with logarithmic spiral antennas". In: *Applied Physics Letters* 104.8 (2014) (cit. on pp. 83, 93).

[114] Christopher W. Berry, Jeremy Moore, and Mona Jarrahi. "Design of reconfigurable metallic slits for terahertz beam modulation." In: *Optics Express* 19 (2011), pp. 1236–1245 (cit. on pp. 83, 93).

[115] Afshin Jooshesh, Levi Smith, Mostafa Masnadi-Shirazi, Vahid Bahrami-Yekta, Thomas Tiedje, Thomas E. Darcie, and Reuven Gordon. "Nanoplasmonics enhanced terahertz sources". In: *Optics Express* 22.23 (2014), p. 27992 (cit. on pp. 83, 93).

[116] Sang-Gil Park, Yongje Choi, Young-Jae Oh, and Ki-Hun Jeong. "Terahertz photoconductive antenna with metal nanoislands." EN. In: *Optics express* 20.23 (2012), pp. 25530–5 (cit. on p. 84).

[117] Gopakumar Ramakrishnan, Nishant Kumar, Gopika K. P. Ramanandan, Aurèle J. L. Adam, Ruud W. A. Hendrikx, and Paul C. M. Planken. "Plasmon-enhanced terahertz emission from a semiconductor/metal interface". In: *Applied Physics Letters* 104.7 (2014), p. 071104 (cit. on p. 84).

[118] Stefan A. Maier. *Fundamentals and Applications Plasmonics : Fundamentals and Applications*. Vol. 677. 2004, p. 10 (cit. on pp. 86, 101).

[119] J.B. Pendry, L. Martín-Moreno, and F.J Garcia-Vidal. "Mimicking surface plasmons with structured surfaces." In: *Science (New York, N.Y.)* 305.5685 (2004), pp. 847–848 (cit. on p. 86).

[120] H. F. Ghaemi, Tineke Thio, D. Grupp, T. W. Ebbesen, and H. J. Lezec. "Surface plasmons enhance optical transmission through subwavelength holes". In: *Physical Review B* 58.11 (1998), pp. 6779–6782 (cit. on p. 86).

[121] A.D. Rakic, A.B. Djurisic, J.M. Elazar, and M.L Majewski. "Optical properties of metallic films for vertical-cavity optoelectronic devices." In: *Applied Optics* 37.22 (1998), pp. 5271–5283 (cit. on p. 88).

[122] D. E. Aspnes, S. M. Kelso, R. A. Logan, and R. Bhat. "Optical properties of AlxGa1-x As". In: *Journal of Applied Physics* 60.2 (1986), pp. 754–767 (cit. on p. 88).

[123] Jean Maysonnave, Nathan Jukam, M.Shahrizan M. Ibrahim, K. Maussang, Julien Madéo, P. Cavalié, Paul Dean, Suraj P. Khanna, D Paul Steenson, Edmund H. Linfield, A. G. Davies, J. Tignon, and S S Dhillon. "Integrated injection seeded terahertz source and amplifier for time-domain spectroscopy." In: *Optics Letters* 37.4 (2012), pp. 731–733 (cit. on p. 98).

[124] Dominic Bachmann, Norbert Leder, Markus Rösch, Giacomo Scalari, Mattias Beck, Holger Arthaber, Jérôme Faist, Karl Unterrainer, and Juraj Darmo. "Broadband terahertz amplification in a heterogeneous quantum cascade laser". In: *Optics Express* 23.3 (2015), p. 3117 (cit. on p. 98).

[125] M. J. Mohammad-Zamani, M. K. Moravvej-Farshi, and M. Neshat. "Modeling and Designing an Unbiased CW Terahertz Photomixer Emitters". In: *Millimeter-Wave and Terahertz Technologies (MMWATT), 2014 Third Conference on*. 2014, pp. 68–71 (cit. on p. 99).

[126] Daryoosh Saeedkia and Safieddin Safavi-Naeini. "A comprehensive model for photomixing in ultrafast photoconductors". In: *IEEE Photonics Technology Letters* 18.13 (2006), pp. 1457–1459 (cit. on p. 99).

[127] Michael Nagel. *Photoconductive structure e.g. radiation source, for optical generation of field signals in terahertz- frequency range in bio analysis, has metallic layers formed from locations and provided in direct contact with semiconductor material*. 2013 (cit. on p. 99).